Icy plumes on Enceladus

Relating the plume properties of Enceladus with channel shape, reservoir conditions and laboratory scale

Tomás Fontes

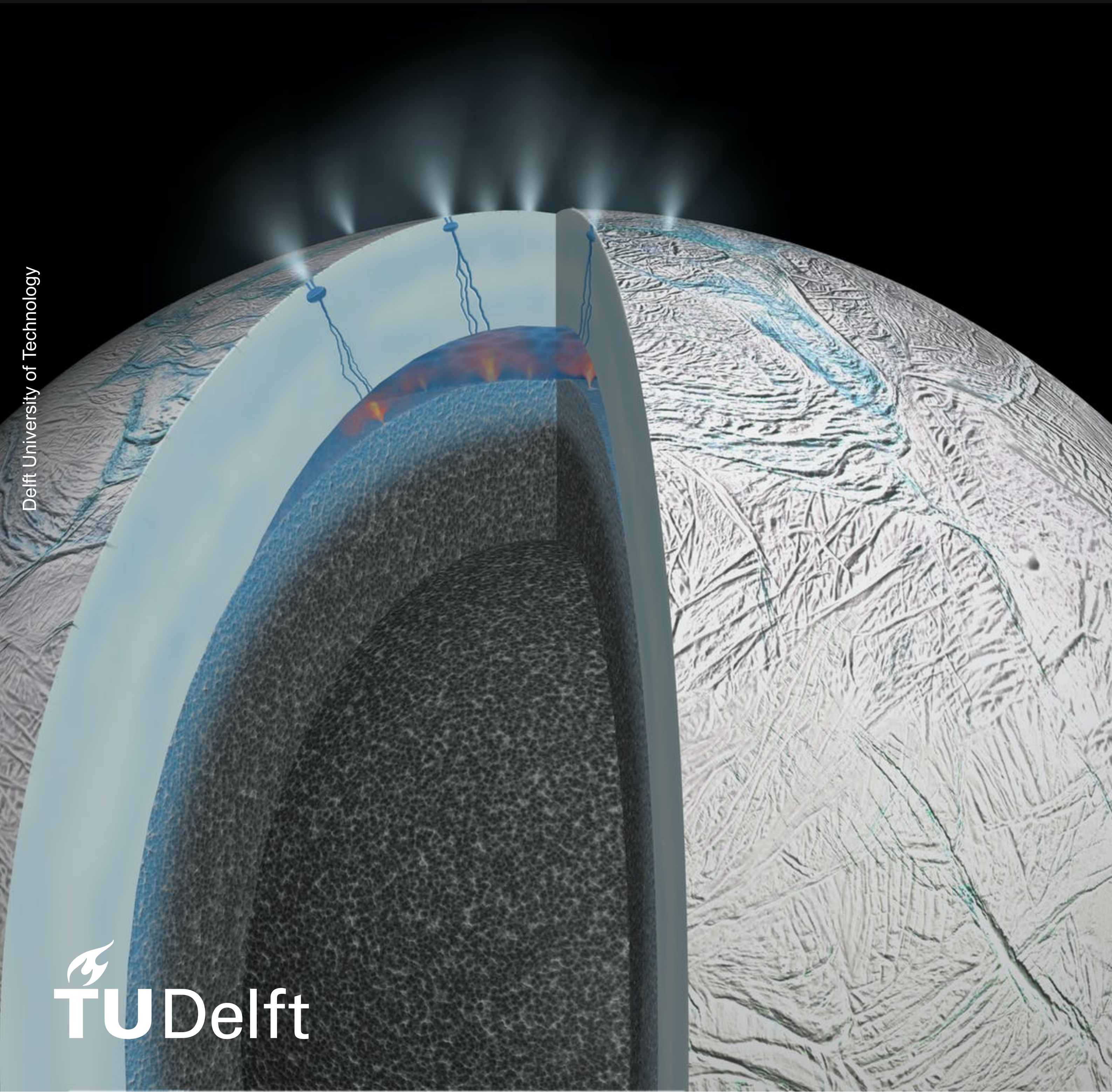

Delft University of Technology

Icy plumes on Enceladus

Relating the plume properties of Enceladus with channel shape, reservoir conditions and laboratory scale

by

Tomás Fontes

to obtain the degree of Master of Science
at the Delft University of Technology,
to be defended publicly on January 13th, 2023 at 15:00.

Student number:	5152895
Instructors:	F. F. J. Schrijer S. M. Cazaux
Assessment comittee:	B. W. van Oudheusden I. Langella A. Cervone
Project Duration:	March, 2022 - January, 2023
Faculty:	Faculty of Aerospace Engineering, Delft

Front cover image credits: NASA/JPL-Caltech.
About the object: Artist's rendering that depicts possible hydrothermal activity that may be taking place on and under the seafloor of the moon's subsurface ocean.

TUDelft

Abstract

This Master thesis consists in investigating the formation and behavior of vapor and ice plumes. These plumes can occur in icy moons of our solar system, such as Europa or Enceladus, which are widely believed to have a liquid water ocean beneath their crust. These plumes most likely consist of a subsurface reservoir of liquid water fed by the ocean, a crevasse, and a vent at the ice surface. Under certain conditions, the liquid water starts evaporating and, due to the high reservoir pressure, the resulting vapour starts flowing upwards through the crevasse. Due to the high pressure difference between the reservoir and the vent at near vacuum conditions, supersonic plumes are formed. This work studies the reservoir conditions and plume physics, gathering different models available in literature and comparing them to available data, such as that from observations from Cassini spacecraft. First, a model capable of describing the condensation phenomenon is sought. The effects of the consequent release of latent heat to be absorbed back by the vapour flow are also studied. Grains will then start to nucleate and grow. These particles can either collide and stick to the walls or keep flowing mixed with the vapour. Some of the above mentioned latent heat can be absorbed back by the icy walls of the crevasse and generate more vapour by sublimation. Further, this project also aims to extend the model mentioned above so that it considers the effects of a fully multi-phase, multidimensional flow, checking for the effects of rarefaction and hence the limits of the continuum assumption. Finally, a similarity analysis is performed so that the influence of working with scales as different as the channels used in the laboratory at TU Delft or the real dimensions of the crevasses found in Enceladus can be fully tackled. Any progress on the ongoing investigations about the physical characteristics of these plumes could be crucial to deepen our knowledge on geological mechanisms in icy moons of our solar system. This, in turn, could trigger research on organic compounds present in these moons, perhaps even allowing for the existence of life. Further, the model used throughout this work can be applied to study power production devices where condensation might play an important role, such as steam turbines for light-water-cooled nuclear reactors or turbines proposed to be used in innovative organic Rankine cycle (ORC) configurations, natural gas supersonic separators, supercritical CO_2 compressors for large-scale carbon capture and sequestration (CCS) and micro-nozzles.

Acknowledgements

This project marks the conclusion of my 3 years journey as a MSc student at TU Delft. 1 year and a half of intense course work plus six months of internship which culminated with one year of this project that allowed me to discover the wonders of Enceladus and its plumes while applying the knowledge of fluid dynamics and thermodynamics I acquired throughout my student life. This work would not have been possible without the insightful help of my thesis supervisors Ferry Schrijer and Stéphanie Cazaux, for whom I am thankful. This was specially true for those times when I felt my progress was slow and a suggestion made by one of them during our group or private meetings helped me through. I am also thankful to Nick van der Hijden, whose work I followed, as well as to Thom Verhoeff, whose laboratory experiments on recreating the plumes I was trying to simulate and ideas we shared also had an impact on my project.

Finally, on a more personal note, I would like to thank my family and friends. Special notes go to my mother and brothers, who always got my back, and friends Francisco Santos, Marco Sala, Conor Creagh, Vincent Versprille and Carlos de Inza, with whom I shared many moments on campus as well as outside, making all this journey a bit less heavy and more funny.

Tomás Fontes
Delft, January 2023

Contents

List of Figures

List of Tables

Nomenclature

Abbreviations

Abbreviation	Definition
CCS	Carbon capture and sequestration
CFD	Computational Fluid Dynamics
DSMC	Direct Simulation Monte Carlo
HST	Hubble Space Telescope
IAPWS	International Association for the Properties of Water and Steam
INMS	Ion and Neutral Mass Spectrometer
ISA	International Standard Atmosphere
MCM	Monte Carlo Method
ORC	Organic Rankine cycle
PDE	Partial Differential Equation
SPT	South Polar Terrain
SST	Shear Stress Transport
TU	Technical University
TVD	Total Variation Diminishing
UVIS	Ultraviolet Imaging Spectrograph
VIMS	Visual and Infrared Mapping Spectrometer

Symbols

Symbol	Definition	Unit
A	Area	[m^2]
a	Average	-
b	Standard deviation	-
	Coefficient from the equation of motion for a grain	[-]
C	Rayleigh function	[m^{-1}]
Cr	Cooling rate	[s^{-1}]
c_{ice}	Heat capacity of ice	[J/(kg K)]
c_p	Isobaric specific heat	[J/(kg K)]
c_s	acoustic speed	[m/s]
c_v	Isochoric specific heat	[J/(kg K)]
D	Diameter	[m]
E	Total internal energy	[J/kg]
e	Specific internal energy	[J/kg]
f	Solid fraction	[-]
H	Total enthalpy	[J/kg]
h	Specific enthalpy	[J/kg]
Kn	Knudsen number	[-]
k_B	Boltzmann constant	[J/K]
k_{eff}	Effective thermal conductivity	[W/(m K)]
k_v	Thermal conductivity of water vapour	[W/(m K)]
k_t	Turbulent thermal conductivity	[W/(m K)]
L	Channel length	[m]

Symbol	Definition	Unit
L_{div}	Length of the divergent portion of the channel	[m]
L_h	Latent heat	[J/kg]
$M/Mach$	Mach number	[-]
m	Water molecule mass	[kg]
$\dot{m}$	Mass flow	[kg/s]
N	Number of droplet particles	[m^{-3}]
Pr	Prandtl number	[-]
p	Pressure	[Pa]
Q	Total mass flow	[kg/s]
q	Specific heat	[J/kg]
q_c	Condensation coefficient	[-]
R	Maximum droplet radius	[m]
R_{gas}	Gas constant	[J/(kg K)]
r	Average droplet radius	[m]
r_c	Critical droplet radius	[m]
Re	Reynolds number	[-]
S	Supersaturation ratio	[-]
s	Specific entropy	[J/(kg K)]
T	Temperature	[K]
t	Time	[s]
t_{act}	Activation time	[s]
u	Velocity	[m/s]
V_{th}	Average molecular velocity	[m/s]
v_m	Molecular volume	[m^3]
Wi	Wilson number	[-]
x	Axial coordinate	[m]
y	Normal coordinate	[m]

Greek symbols

Symbol	Definition	Unit
α	Modelling parameter	[-]
	Weight factor	[-]
β	Condensation coefficient	[-]
Γ	Condensation mass rate	[kg/(m^3 s)]
γ	Specific heat ratio	[-]
γ_{nuc}	Specific heat ratio	[m^{-3} s^{-1}]
Δ	Difference in	-
δ_{ij}	Kronecker δ	-
ϵ	Expansion ratio parameter	[m^{-1}]
θ_H	Heaviside function	-
λ	Molecular mean free path	[m]
λ_g	Coefficient of convective heat transfer from the gas to the droplet	[W/(m^2 K)]
μ	Dynamic viscosity	[Pa s]
ν	Kinematic viscosity	[m^2/s]
	Modelling correction coefficient	[-]
π	Mathematical constant=3.14159265359...	[-]
ρ	Density	[kg/m^3]
σ	Water surface tension	[N/m]
τ	Shear stress tensor	[N/m^2]
	Average time between successive wall collisions	[s]
ϕ	Flux	[kg/s]

Symbol	Definition	Unit
Ψ	Generalized field variable	-
ψ	Volumetric flux	[m^3/s]

Subscripts

Symbol	Definition
0	Total/stagnation value
cr	Value at thermodynamic critical point
eq	Value at equilibrium
f	Face
	Relative to solid fraction
max	Maximum value
N	Sample
p	Particle
r	Reduced
res	Value at the reservoir
S	Surface
s	Sublimation
sat	Saturation
V	Volume
W	Wilson point
w	Value at the wall

Superscripts

Symbol	Definition
0	Determined from old time step values
∞	Value at the outlet
'	Derivative
(l.g.)	liquid-vapour
(s.g.)	solid-vapour

Special characters

Symbol	Definition
∇	Nabla operator
∂	Partial differential
$\sum$	Summation
$\int$	Integral

1

Introduction

Moons can be composed of several different components. Some, like Earth's Moon, are essentially rocky, while others, such as Jupiter's Europa or Saturn's Enceladus, have their crust consisting of an ice shell, with tidal heating provided by their parent gas giants allowing for the presence of liquid oceans below their ice shells (Kite et al. 2016, Nimmo et al. 2007). For this reason, these two moons started to arouse interest in the scientific community.

Images of Europa have been captured by the Hubble Space Telescope (HST), although without direct measurements from flyby's. On the other hand, in 2005 the Cassini spacecraft discovered geyser emissions at the southern polar region of Enceladus, with direct measurements from flyby's. The ice particles emitted by these geysers are known to be the main source of Saturn's E ring. These plumes originate on four linear structures, the so-called 'tiger stripes'.

Gas ejection velocities are estimated by fitting the Ultraviolet Imaging Spectrograph (UVIS) and Ion and Neutral Mass Spectrometer (INMS) data to be in the range of 300-500 m/s according to Schmidt et al. 2008 (or higher according to Dong et al. 2011). However, grain ejection velocities are found to be lower than Enceladus' escape velocity of 240 m/s. This difference cannot be justified on the gas and dust interaction in the plume, as it is too dilute, so it must originate below the surface (Schmidt et al. 2008). Another inference made is that the gas appears to form near the triple point of water (273.16 K, 611.2 Pa). This can be argued, because were it to happen due to sublimation of ice at a temperature lower than 260K, the resulting gas density would be too low to support the measured particle fluxes (Schmidt et al. 2008). This also led the scientific community to believe in the existence of a large body of liquid water below the ice shell, possibly an ocean.

Currently, there are ongoing laboratory experiments in TU Delft to investigate these plume phenomena. One of such projects is the one performed by Sklavenitis 2022 and continued by Verhoeff 2023, whose main goal is to investigate the effects that the measured plume parameters have on the physical and chemical characteristics of the subsurface ocean and the icy crust of Enceladus. Past projects done by fellow students on the numerical analysis of the plumes include the work performed by Hijden 2021, which performs numerical simulations of the plumes with variable crevasse shapes and reservoir conditions and validating them with available data from literature. This model accounts for particle production from homogeneous nucleation, particle growth, wall accretion, sublimation, wall friction, and heat convection.

This project proposes complementing the works described in the previous paragraph with a fully multi-phase, multidimensional model for condensation and grain dynamics phenomena behind the plumes of Enceladus. Different channel geometries and reservoir conditions are simulated and the respective effects on the plume properties investigated. Then, a similarity analysis is performed so that an appropriate comparison between length scales as different as the laboratory channels and Enceladus cracks can be elaborated. Finally, based on available plumes data from authors such as Schmidt et al. 2008, Hedman et al. 2009, Gao et al. 2016 and Kieffer et al. 2009, an appropriate range of channel geometric parameters and reservoir conditions are chosen. Also, a comparison is made between results predicted by simulations and experimental data obtained by Verhoeff 2023. The complex phenomena occurring in the plumes of Enceladus could then be better understood, which in turn could trigger further research on the possibility of Enceladus to have a global or, at least, regional subsurface body of water. This could be key to evaluate the plausibility of Enceladus to be able to host life.

1.1. Research questions

Before starting to elaborate this project, several questions arose from studying past works as well as throughout the process of elaborating this project. A list of such questions is hereby presented.

Q1: Which physical processes should be included to model the plumes of Enceladus? And what is the effect of each of these processes?

1. Condensation: nucleation and grain growth.
2. Wall friction and heat convection.
3. Quasi-1D (Hijden 2021) vs. 2D model.

Q2: How can observations from the plumes of Enceladus relate to characteristics of the crevasse and reservoir?

1. How do the geometric parameters of the channel (length, expansion ratio, smooth/sharp throat, throat location) influence the plume characteristics (velocity, number of particles, solid fraction, average droplet size)?
2. How do the reservoir conditions (temperature, pressure) affect the plume characteristics?
3. Which channel shape and reservoir conditions are the best fit for the plume characteristics observed by Cassini? Can the results be scaled up from the laboratory to Enceladus?

1.2. Report outline

This report starts by summarizing the work available in literature on the composition and mechanisms of the plumes in Enceladus, which will serve as base knowledge to perform the proposed thesis project. In chapter 2 the current knowledge about the geological behaviour of Enceladus is summarized. In chapter 3 a comprehensive theoretical background for the plume phenomena is set up, in terms of fundamental conservation equations and constitutive relations retrieved from available literature. This chapter finishes by applying the described model to a preliminary parametric study of the onset of condensation. Then, in chapter 4 a more complete model is proposed by the author, validated with a known case from literature. In chapter 5 an explanation is given about the geometric and numerical conditions for the different simulation setups. In chapter 6 an analysis on the results obtained by using the model proposed in chapter 4 is provided, giving it an outlook in light of the expected outcomes. Finally, chapter 7 gives a general conclusion to the project. The research questions self-proposed in chapter 1 are answered there, from which the main ideas to retain from the thesis project are drawn upon. Also, important remarks and suggestions for future works on this topic are proposed.

2

Enceladus and its plumes

In order to acquire a fundamental understanding on the physical phenomena behind the plumes of icy moons such as Enceladus, first it is useful to attain general knowledge about Enceladus and its geological characteristics. As such, this chapter, the main characteristics of Enceladus are mentioned and a geological background is given to describe possible mechanism behind the plume phenomena.

2.1. Enceladus: a moon of Saturn

Enceladus is a 504 km diameter moon, orbiting Saturn between Mimas and Tethys, with an orbital eccentricity of 0.0047, explained by a mean motion resonance with Dione (C. C. Porco et al. 2006). Its peculiar surface properties have long been known, such as its visual geometric albedo of 1.4, which makes Enceladus one of the brightest satellites in the solar system, with pure water ice dominating its reflectance spectrum. Analysis to the very narrow size distribution of particles constituting Saturn's E ring suggests possible present-day phenomena such as venting or geyser-like activity, responsible for supplying the E ring particles (C. C. Porco et al. 2006).

2.2. Plume mechanisms

The mechanisms behind the plumes discovered in Enceladus are still a mystery to these days. However, several investigative works have been performed based on observed evidence from measurements taken in the vicinity of the icy moon by spacecrafts such as Cassini (Matson, Spilker, et al. 2002). This was a pioneering mission which took almost 20 years to be completed (launched in October, 1997 and ended in September, 2017). It was a sophisticated robotic spacecraft sent to study Saturn and its complex system of rings and moons in unprecedented detail. Based on such measurements, Nimmo et al. 2007 argues that shear heating by tidally driven lateral (strike-slip) fault motion is the main mechanism to cause liquid water from the reservoirs to boil and thereafter create the vapour plumes. Kite et al. 2016 further adds that the model with tidally flexed slots along the ice shell explains the persistence of the eruptions throughout the tidal cycle, the phase lag (peak plume flux lags peak tidal extension by $\pm 1 rad$), the total power output of the south polar terrain (SPT), and that the eruptions can be maintained over geological timescales. According to Matson, Castillo-Rogez, et al. 2012, Matson, Castillo-Rogez, et al. 2018, plumes are maintained by a mechanism of water circulation that brings water from a subsurface ocean towards the surface through straight cracks (named conduits by the authors) opened by regular tidal forces. C. Porco et al. 2014 connects the phenomena of geysering, tidal stresses, and anomalous thermal emission across the south pole of Enceladus, conjecturing that normal (tensile) stresses open conduits in the ice shell through which water (containing vapour and icy grains) flows with convection of latent heat until it reaches the surface. Figure 2.1 and Figure 2.2 illustrate this. C. Porco et al. 2014 further argues that the plumes that this project intends to study consist of supersonic flows of water vapour and ice particles. Degrees of salinity around 0.5-2% and emitted particle size measured by the Cassini mission indicate the presence of a liquid ocean beneath the crust of ice. Postberg et al. 2011, Postberg et al. 2009 argue that salt-water reservoirs with a large evaporating surface provide nearly all of the matter in the plume. This comes in direct contradiction with Ingersoll and Nakajima 2016a, Ingersoll and Nakajima 2016b, which counter-argue that controlled boiling caused by the back pressure due to friction with the walls implies that water-vapour interfaces can be located within the narrow cracks, at the level of neutral buoyancy.

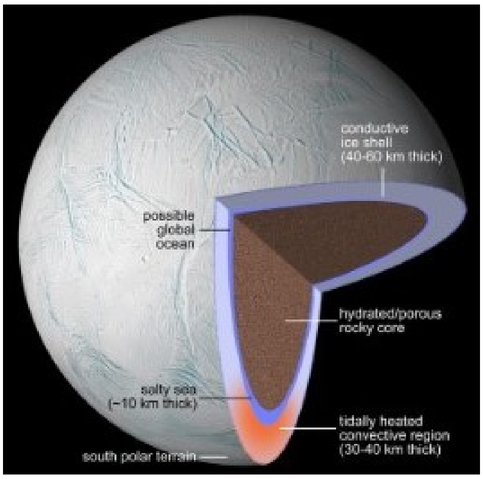

Figure 2.1: Possible geological structure of Enceladus (C. Porco et al. 2014).

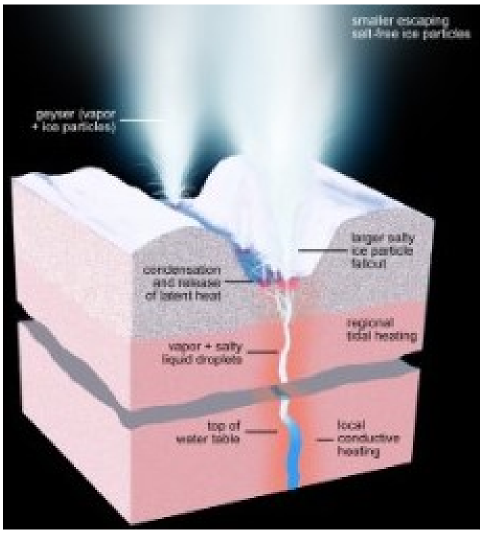

Figure 2.2: Schematic representation of a possible plume mechanism (C. Porco et al. 2014).

2.3. Plume physics

In this section, a detailed description of the theoretical foundations behind the processes of water vapour expansion, condensation, grain nucleation and growth and wall interactions (accretion, sublimation, friction and heat convection) is presented, mainly retrieved from literature and past projects. Water (H_2O) is the only known substance which can naturally be found in solid, liquid and vapour phases. Its occurrence, namely in liquid state, is essential to the very existence of life as we know it. Thus, the possibility of its presence in planets or moons is considered by the scientific community as a hope for life to exist or, at least, be possible in those places. The phase diagram of water is shown in Figure 2.3, where its different possible solid states are numbered from I to XI. Details on this nomenclature are out of scope of this project and is well described by works such as Atkins et al. 2006. Figure 2.3 shows an important point for this project: the triple point of water (273.16 K, 611.2 Pa), whose importance will become clear later on.

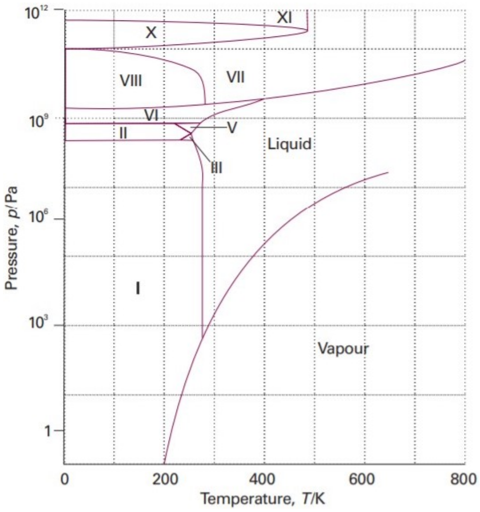

Figure 2.3: Experimental phase diagram of water (Atkins et al. 2006).

2.3.1. Structure

Enceladus, like any planet or moon, is comprised of different materials, disposed in layers according to their relative density. Becx 2019 summarizes the sizes of the structure of Enceladus as in Table 2.1.

Silicate core radius [km]	182.5 ± 2.5
Ocean thickness [km]	38 ± 4
Ice-shell thickness [km]	20 ± 2 x 5
Outer radius [km]	257 x 251 x 248

Table 2.1: Sizes of the structure of Enceladus

In turn, this enables the creation of a fully scaled model for the structure of Enceladus, which is shown in Figure 2.4.

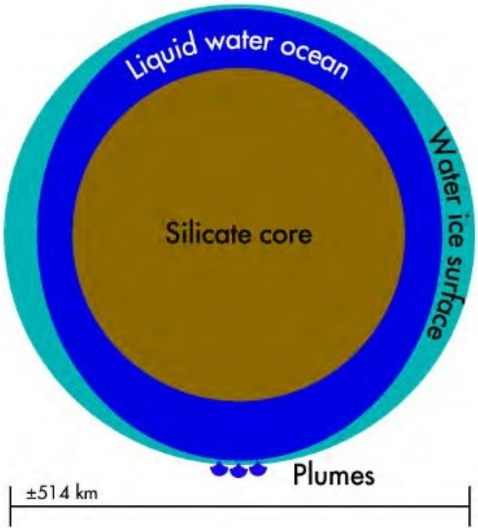

Figure 2.4: Scaled structure of Enceladus (except for the size of the plumes) (Becx 2019).

As the plumes extend through the ice shell of Enceladus, it is important to know, or at least have an idea, about the temperature gradient expected throughout this layer. Detailed information on this topic is rather cumbersome to obtain. However, a model is given by Roberts et al. 2008, shown in Figure 2.5. This figure shows that Enceladus has a relatively warm internal core below a cold crust. Particularly, there is a region where temperature is around 273 K where the existence of liquid water in equilibrium with ice is possible.

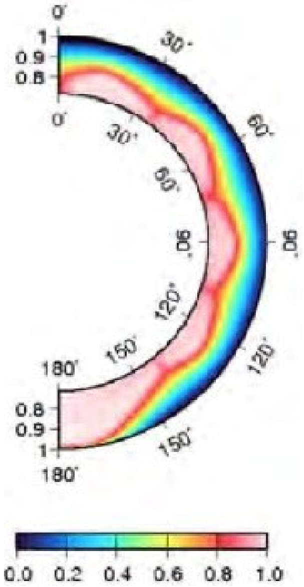

Figure 2.5: Internal temperature gradient for the ice shell of Enceladus including convection and shear heating. $T' = 0$ corresponds to $T = 75K$ and $T' = 1$ corresponds to $T = 273K$ (Roberts et al. 2008).

As for the plumes content, measurements taken by Cassini's INMS are available. These measurements played an important role in unveiling Enceladus' under-surface ocean composition. Table 2.1 provides a non-extensive list of molecular compounds present in Enceladus' plumes.

Molecule	Volume mixing ratio
H_2O	0.90 ± 0.01
CO_2	0.053 ± 0.001
H_2CO	$(3.1 \pm 1) \cdot 10^{-3}$
CH_3OH	$(1.5 \pm 0.6) \cdot 10^{-4}$
C_2H_4O	$< 7.0 \cdot 10^{-4}$
C_2H_6O	$< 3.0 \cdot 10^{-4}$
^{40}Ar	$(3.1 \pm 0.3) \cdot 10^{-4}$
NH_3	$(8.2 \pm 0.2) \cdot 10^{-3}$
N_2	< 0.011
HCN	$< 7.4 \cdot 10^{-3}$
CH_4	$(9.1 \pm 0.5) \cdot 10^{-3}$
C_2H_2	$(3.3 \pm 2) \cdot 10^{-3}$
C_2H_4	< 0.012
C_2H_6	$< 1.7 \cdot 10^{-3}$
C_3H_4	$< 1.1 \cdot 10^{-4}$
C_3H_6	$(1.4 \pm 0.3) \cdot 10^{-3}$
C_3H_8	$< 1.4 \cdot 10^{-3}$
C_4H_8	$(2.3 \pm 0.3) \cdot 10^{-4}$
C_4H_{10}	$< 7.2 \cdot 10^{-4}$

Table 2.2: INMS measurements of Enceladus plume content measured on 09-10-2008. Data obtained from Waite Jr et al. 2009.

2.3.2. Crack shape

Two basic shapes for the crevasses through which the plumes flow from the subsurface reservoirs up to the surface have been proposed: Figure 2.6 and Figure 2.7. The former is a crack in the ice of uniform width extending from the subsurface ocean up to the surface, which is several kilometers deep. Evaporation occurs inside the crack due to a back pressure much smaller than that of the reservoir. The later is a channel with a varying cross section. Water evaporates from the ocean to fill the reservoir at the triple point and the resulting vapour flows through the crack with a behaviour similar to that of a gas flow through a convergent-divergent nozzle.

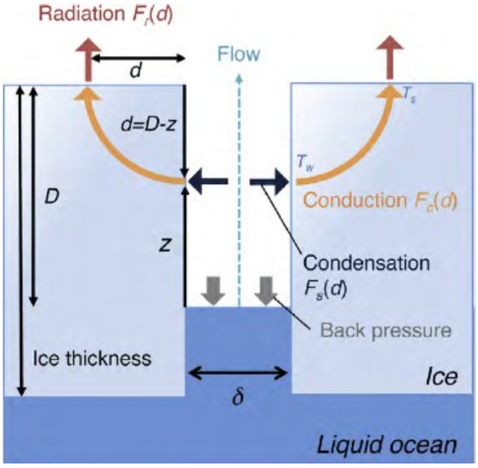

Figure 2.6: Plume scheme proposed by Ingersoll and Nakajima 2016a.

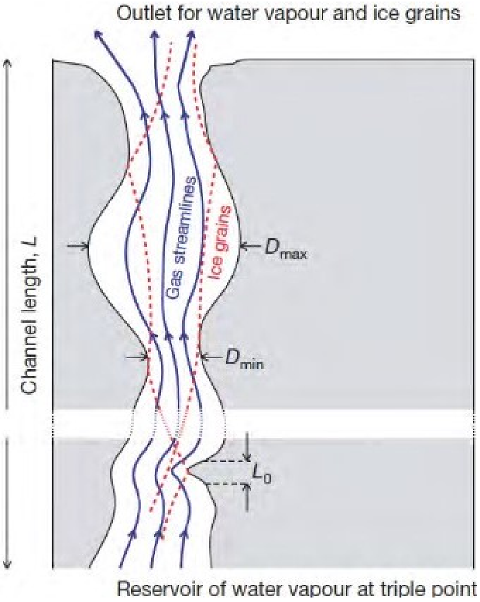

Figure 2.7: Plume scheme proposed by Schmidt et al. 2008.

2.3.3. Plume content

Based on observations from Cassini, values for plume properties such as ejection velocity, grain size and solid fraction have been proposed, summarized by Table 2.3. Ejection velocities have been measured in the range of 350-950 m/s by fitting the UVIS and INMS data (Dong et al. 2011, Schmidt et al. 2008). Measured droplet sizes are mostly in the range of 0.1-1 μm (Hedman et al. 2009, Schmidt et al. 2008). On the other hand, authors such as Kempf et al. 2010 refer the possibility for particles with significantly larger sizes to occur (up to 75 μm), which fall back on to the planet's surface near the vents and are therefore not captured by Cassini's Visual and Infrared Mapping Spectrometer (VIMS). Also, wall interactions such as accretion and sublimation or tidal phenomena like frictional cracking can change the channel shape over time and thus allow for a wide variety of particle sizes to occur. Another possible explanation for the larger than expected particle sizes is the occurrence of boiling in the reservoir (Ingersoll and Nakajima 2016b). The resulting bubbles burst to form a mix of vapour and tiny grains once they reach the reservoir surface. These droplets then have a much longer distance to travel until they reach the vent compared to particles formed in the main nucleation region close to the channel throat. As a result, the particles formed in the reservoir will grow significantly bigger. Regarding solid fraction, values in the range 0.07-0.2 have been measured for the plumes of Enceladus (Gao et al. 2016, Kieffer et al. 2009).

Property	Range of values
Ejection velocity	350-950 m/s
Temperature	210-240 K
Droplet size	0.1-75 μm
Solid fraction	0.07-0.2

Table 2.3: Measured values for some plume properties.

3

Preliminary analysis of the plumes

In order to model the physical processes behind Enceladus plumes, Yeoh, Chapman, et al. 2015 describes the subsurface flow as a simple isentropic quasi-1D flow expanding through a converging–diverging nozzle from stagnation conditions at the triple-point of water in the reservoir, as shown in Figure 3.1. This model provides an analytical solution for the flow, completely described by the channel geometry (Anderson Jr. 2017). Consequently, only the vent-to-throat area ratio needs to be known to obtain the vent properties:

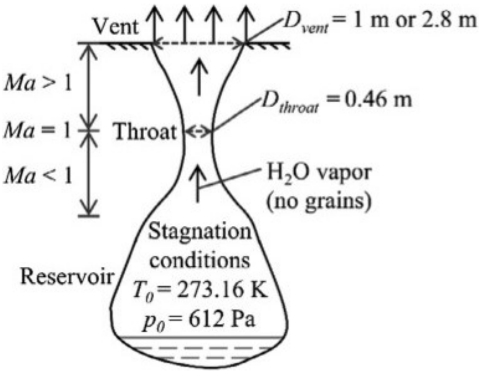

Figure 3.1: Isentropic quasi-1D flow plume model (Yeoh, Chapman, et al. 2015).

$$\frac{p}{p_0} = \left(\frac{\rho}{\rho_0}\right)^{\gamma} = \left(\frac{T}{T_0}\right)^{\frac{\gamma}{\gamma-1}} \tag{3.1}$$

$$\frac{A}{A_{throat}} = \left(\frac{2}{\gamma+1}\right)^{\frac{\gamma+1}{2(\gamma-1)}} \frac{\left(1+\frac{\gamma-1}{2}M^2\right)^{\frac{\gamma+1}{2(\gamma-1)}}}{M} \tag{3.2}$$

In the previous two equations, p is the gas pressure, $\gamma = 4/3$ is the specific heat ratio of water vapour, ρ is the gas density, T is the gas temperature, A is the channel cross-section area and M is the Mach number. The subscript 0 refers to stagnation quantities. Also, the ideal gas equation is used as equation of state for water vapour (where R_{gas} is the water vapour specific gas constant, 461.5 $J/(kgK)$):

$$p = \rho R_{gas} T \tag{3.3}$$

This model predicts vent velocities in the range of 700-900 m/s and vent temperatures of 110-53 K, considerably lower than what was measured by Cassini (Schmidt et al. 2008). As downsides, this model contains several limitations, such as not accounting for grain condensation, wall interactions or turbulence. An improvement to this model is suggested by Yeoh, Li, et al. 2016, which uses a Direct

Simulation Monte Carlo (DSMC) method, a numerical method for modeling rarefied gas flows, in which the mean free path of a molecule is of the same order (or greater) than a representative physical length scale (Bird 1994) and thus the Navier-Stokes equations can be inaccurate. This model accounts for the processes lacking in the isentropic quasi-1D model, namely condensation and wall interactions, which are found to be important (Ingersoll and Pankine 2010). The gas used in the simulation is pure H_2O vapor and spherical ice grains with a density of 920 kg/m^3 are assumed. A constant wall temperature of 230 K is assumed. The channel geometry under consideration is also more complicated and contains an additional throat, as shown in Figure 3.2. From this model, subsonic (Mach number around 0.8) plumes are obtained at the vent, corresponding to vent velocities of about 280 m/s and temperatures around 240 K, so not in good agreement with what was observed for the actual Enceladus plumes.

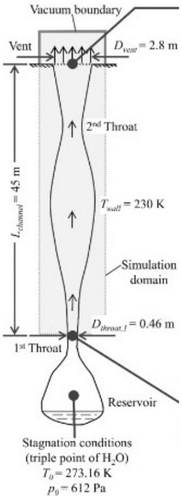

Figure 3.2: Schematic of computational subsurface model (Yeoh, Li, et al. 2016).

3.1. Quasi-1D plume model

The models mentioned above are either too simplistic (Yeoh, Chapman, et al. 2015) or involve considerably complex tools such as DSMC (Yeoh, Li, et al. 2016). Thus, neither of them will be used in this project, only serving for comparison. The role wall interactions play in the plume properties was studied by Hijden 2021. However, in this work such effects are left out, as the author's main goal is to perform a similarity analysis to study the influence of working with channel dimensions as discrepant as those found in Enceladus or in the Aerodynamics laboratory at TU Delft, where wall interactions are absent. A more practical model is the one by Schmidt et al. 2008, which splits the model of Enceladus' dust plumes into three conceptually different parts: (i) the gas outflow through the channels along with nucleation and growth of icy particles, (ii) grain collisions with channel walls and their interaction with the vapour stream and (iii) formation of the plume by the ballistic motion of the dust particles. Such model is described in the following paragraphs. In order to make a first centreline quasi-1D estimate, the vapour flow is modelled by the transient 1D Euler equations in their conservative form (Equation 3.4), with extra source terms accounting for condensation and wall interactions, namely grain accretion and sublimation. The flow variables are the following: u is the gas flow velocity, h is its specific enthalpy, t is time, x is the vertical distance from the reservoir and $\dot{m}_n$ is the nucleated mass flow. The remaining parameters are described in the following sections.

$$\begin{aligned}
&\frac{\partial(\rho A)}{\partial t} + \frac{\partial(\rho A u)}{\partial x} = -\frac{\dot{m}_n}{\Delta x} \\
&\frac{\partial(\rho A u)}{\partial t} + \frac{\partial(\rho A u^2)}{\partial x} = -A\frac{\partial p}{\partial x} - u\frac{\dot{m}_n}{\Delta x} \\
&\frac{\partial\left(\rho A\left(e+\frac{u^2}{2}\right)\right)}{\partial t} + \frac{\partial\left(\rho A\left(h+\frac{u^2}{2}\right)u\right)}{\partial x} = \frac{\partial(\rho A u f)}{\partial x}L_h
\end{aligned} \tag{3.4}$$

The set of equations above is a system of partial differential equations (PDEs), which alone do not form a closed system. Hence, additional (constitutive) relations are needed for closure. Water vapour is modelled as a thermally (Equation 3.3) and calorically (Equation 3.5, Equation 3.6) perfect gas. Here, e is the gas specific internal energy, c_v is the gas isochoric specific heat (1384.5 $J/(kgK)$) and c_p is the gas isobaric specific heat (1846 $J/(kgK)$). These equations are solved with the MacCormack method (Anderson Jr. 2017), which uses a predictor-corrector scheme based on forward and rearward differences.

$$e = c_v T \tag{3.5}$$

$$h \equiv e + \frac{p}{\rho} = (c_v + R_{gas})T = c_p T \tag{3.6}$$

3.2. Condensation

Condensation of water vapour into ice is enhanced by high temperature gradients, which can be found near the throat of the channel. This leads to an increase in the supersaturation of the vapour (Matsuo et al. 1986). This phenomenon is modelled by the term $\frac{\partial(\rho A u f)}{\partial x} L_h$ in the energy component of Equation 3.4, where f is the solid fraction of the mass flow and L_h is the latent heat released by condensation of the vapour (2.836 MJ/kg). When a particle is larger than a certain critical radius R_c, growth is enhanced, increasing the solid fraction, whose evolution is described by Equation 3.7 (Schmidt et al. 2008). Here, ρ_{grain} is the density of the icy grains (920 kg/m^3), Q is the total mass flow, γ_{nuc} is the nucleation rate, R is the maximal radius of the ice particles, R' is the growth rate of the particles and Θ_H represents the Heaviside function.

$$f'(x) \equiv \frac{df}{dx} = \frac{4\pi\rho_{grain}}{Q} \int_0^x \gamma_{nuc}(x_0)[R(x) - R(x_0)]^2 R'(x) A(x_0) \Theta_H(R(x) - R(x_0)) dx_0 \tag{3.7}$$

3.2.1. Nucleation

The ice particles form by condensation of water vapour, combining molecules in a process called nucleation. There is a high amount of literature available about this topic. However, it is often only applicable to certain specific conditions. Schmidt et al. 2008 used a regression from previous available data. However, it was mentioned that the calibration of the pressure had to be corrected for. This was done by Wölk et al. 2001, who came up with an empirical relation for H_2O valid for nucleation rates in the range $1 < \gamma_{nuc}/cm^{-3}s^{-1} < 10^{20}$, temperatures between $200K < T < 300K$ and supersaturation in the range $5 < S < 200$. Wölk et al. 2001 starts with classical nucleation theory - Becker-Döring nucleation rate:

$$\gamma_{BD} = \sqrt{\frac{2\sigma}{\pi m}} v_m \left(\frac{p_{gas}}{k_B T_{gas}}\right)^2 \exp\left(-\frac{16\pi v_m^2 \sigma^3}{3(k_B T_{gas})^3 (\ln S)^2}\right) \tag{3.8}$$

The theory behind this equation is extensive and an in-depth explanation is provided by Bakhtar et al. 2005. In Equation 3.8, σ, m and v_m are respectively the surface tension of the critical cluster (Equation 3.9, Wölk et al. 2001), the mass of the water molecule and the molecular volume. S is the supersaturation (Equation 3.10, Schmidt et al. 2008), where ρ_{gas} and $\rho_{eq}^{(l.g.)}(T_{gas})$ are the actual vapour and vapour-liquid equilibrium densities. p_{gas} and T_{gas} are respectively the vapour pressure and temperature. k_B is the Boltzmann constant. The nucleation rate for water is then obtained by multiplying Equation 3.8 by a correction factor, yielding Equation 3.11. Here, the empirical constants are $A = -27.56$ and $B = 6.5 \cdot 10^3 K$ (Wölk et al. 2001).

$$\sigma = 93.6635 \cdot 10^{-3} + 9.133 \cdot 10^{-6} T - 2.75 \cdot 10^{-7} T^2 \tag{3.9}$$

$$S \equiv \frac{\rho_{gas}}{\rho_{eq}^{(l.g.)}(T_{gas})} \tag{3.10}$$

$$\gamma_{H_2O} = \gamma_{BD} \exp\left(A + \frac{B}{T}\right) \tag{3.11}$$

It is worth noting that in Equation 3.10 the vapour-liquid equilibrium is used instead of the vapour-solid one. This is because the nuclei of the new phase at the channel conditions contain only 20-30 water molecules, which is too small to treat them as crystalline (Schmidt et al. 2008). $\rho_{eq}^{(l.g.)}$ is obtained with an empirical relation for the vapour-liquid equilibrium pressure $p_{eq}^{(l.g.)}$ (Equation 3.12, Peeters et al. 2002) and the ideal gas law (Equation 3.3).

$$p_{eq}^{(l.g.)}(T_{gas}) = 610.8\,\text{exp}\left[-5.1421\,\text{ln}\,(T_{gas}/273.15) - 6828.77(1/T_{gas} - 1/273.15)\right] \tag{3.12}$$

In order to check whether supersaturation is achieved, it is of interest to compare the slopes of the p vs T curves for the isentropic expansion described by Poisson's law (Equation 3.1) and the equilibrium condensation. For this, the equations of these slopes, Equation 3.13 and Equation 3.14 respectively, can be written.

$$\left(\frac{\partial p}{\partial T}\right)_{isentropic} = \frac{p}{T}\frac{\gamma}{\gamma - 1} \tag{3.13}$$

$$\left(\frac{\partial p}{\partial T}\right)_{condensation} = \left(\frac{6828.77}{T^2} - \frac{5.1421}{T}\right)p \tag{3.14}$$

The ratio between the slopes of these two curves can then be written as in Equation 3.15.

$$\frac{\left(\frac{\partial p}{\partial T}\right)_{condensation}}{\left(\frac{\partial p}{\partial T}\right)_{isentropic}} = \frac{6828.77 - 5.1421T}{T}\frac{\gamma - 1}{\gamma} \tag{3.15}$$

Equation 3.15 can be rewritten in terms of the enthalpy of vaporization (which is equal to the latent heat released by condensation of the vapour, L_h) and the gas isobaric specific heat c_p, assuming these properties remain constant in the temperature range of interest (reasonable for short ranges). This ratio then reads as in Equation 3.16 (Wegener 1964).

$$\frac{\left(\frac{\partial p}{\partial T}\right)_{condensation}}{\left(\frac{\partial p}{\partial T}\right)_{isentropic}} = \frac{L_h}{c_p T} \tag{3.16}$$

This ratio is found to be larger than 1 for water and other vapours for temperatures ranging from 0 ºC up to the critical point (Wegener 1964), i.e. the point at which liquid and vapour phases are indistinguishable. This means that the curve of saturated vapour pressure is steeper than the isentrope. Or, by other words, $p_{eq}^{(l.g.)}$ decreases faster than p_{gas}. Therefore, if the vapour keeps expanding isentropically for long enough, the two curves intersect and the vapour becomes saturated: $S = 1$. If the vapour expands any further, either condensation is enhanced or the vapor will enter a metastable state and become supersaturated ($S > 1$) without the formation of another phase. In the first case, the two phases are in equilibrium as the process follows a saturated isentrope ($S = 1$). In the second case, the vapor will follow a "dry" isentrope as if the boiling curve did not exist.

The first case can occur if the wall temperature is low enough and condensation nuclei (impurities such as dust or condensed particles of less volatile species) are already present: **heterogeneous nucleation**. By contrast, in the absence of foreign nuclei, supersaturation will be reached. Small clusters of vapor molecules are continuously formed by random fluctuations. However, they quickly disintegrate unless they attain a certain minimum critical size (Kikoin et al. 1978). If the vapor finally condenses on itself, the process is called **homogeneous nucleation**. However, as this corresponds to breaking a metastable state, the process is irreversible and entropy increases until equilibrium is again reached ($S = 1$). Figure 3.3 illustrates the different condensation processes that can take place depending on the physical and chemical conditions of the flow.

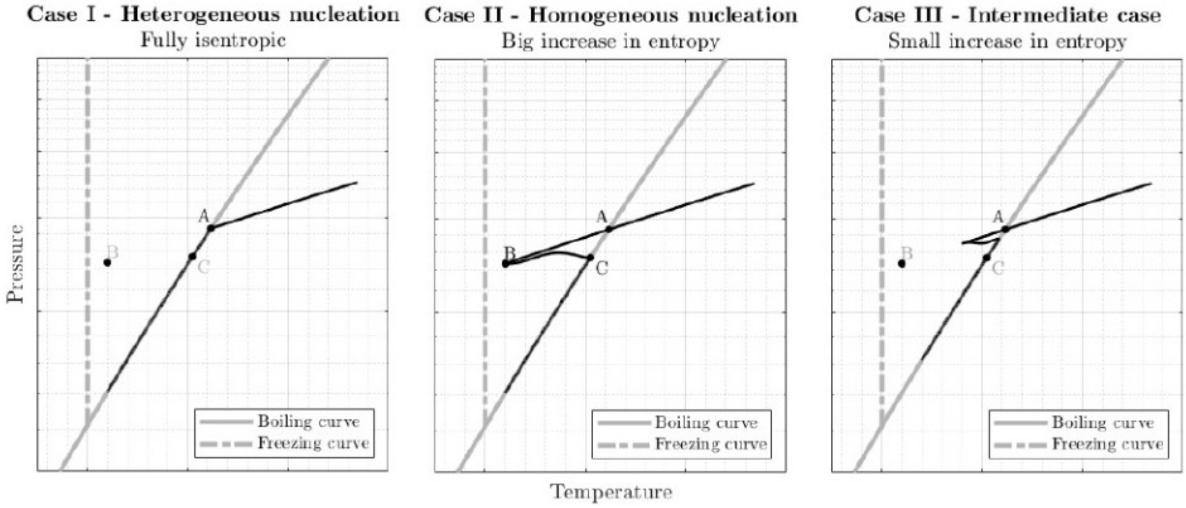

Figure 3.3: PT phase diagrams depicting three different condensation processes in a nozzle. Left: fully isentropic heterogeneous nucleation. Middle: homogeneous nucleation with big increase in entropy. Right: intermediate case with heterogeneous nucleation commencing after the vapor becomes supersaturated (Wegener 1964).

In particular, it is useful to consider point B of case II in Figure 3.3. This is the so-called Wilson point and the correspondent temperature is called Wilson temperature (T_W), which is defined by Equation 3.17 (Azzini 2019). In this equation, $T_{sat}(s_0)$ is the isentropic saturation temperature, T_{cr} is the critical temperature and Wi is the dimensionless Wilson number.

$$T_W \equiv T_{sat}(s_0) - T_{cr}Wi \tag{3.17}$$

Numerical determination of the Wilson point

In order to define the Wilson number in terms of physically meaningful variables, one first considers what happens between the saturation condition and the moment at which nucleation is enhanced. As the vapour is expanding, temperature is decreasing and therefore one can define a cooling rate Cr as (Azzini 2019):

$$Cr \equiv \frac{1}{T_{cr}}\frac{dT}{dt} \tag{3.18}$$

This is a local property, due to the fact that it is defined for any point along a streamline. The key-idea for the calculation of the Wilson temperature is the fact that there exists a correlation between an average cooling rate $\bar{Cr}$ to which the sub-cooled vapor is subjected and the time elapsing from the instant in which saturated conditions are achieved until the onset of stable condensation. This time interval, defined as activation time t_{act}, allows to cast the temperature difference $T_{sat}(s_0)$−T_W in dimensionless form as (Azzini 2019):

$$\frac{T_{sat}(s_0)\text{−}T_W}{T_{cr}} = \bar{Cr} \cdot t_{act} \tag{3.19}$$

Hence, combining Equation 3.17 and Equation 3.19 to define the Wilson number in terms of both the average cooling rate $\bar{Cr}$ and the activation time t_{act} (Azzini 2019):

$$Wi = \bar{Cr} \cdot t_{act} \tag{3.20}$$

Equation 3.20 is very useful in that it provides a relation between the Wilson number and physically meaningful properties of the flow. One downside of this equation is that it provides no closure to the model for the estimation of T_W, as it depends on two unknowns ($\bar{Cr}$, t_{act}). However, according to Azzini 2019, a functional dependence $t_{act} = f(\bar{Cr})$ exists. This is because of the very physical nature of the condensation mechanism: for time values $t > f(\bar{Cr})$ there are two phases present (vapour and condensate), whereas for $t < f(\bar{Cr})$ stable nucleation does not occur and only the vapour phase is present (Azzini 2019).

Therefore, using $t = 0s$ as a convention for the time instant at which the fluid is at saturation conditions, t_{act} can be interpreted as the time instant just before condensate droplets start forming. Physically, for each value $\bar{Cr}$, there is a finite time for which steam remains sub-cooled, after which stable nucleation is triggered (Azzini 2019).

As t_{act} and T_W both depend on the same set of physical parameters, due to both being characteristics of the condensation process, t_{act} can be calculated by integrating along a streamline. Using the quasi-1D approximation, this can be written as (where x is the coordinate along the nozzle axis and u is the velocity of the flow (Azzini 2019)):

$$t_{act} = \int_{x(T_{sat}(s_0))}^{x(T_w)} \frac{dx}{u} \tag{3.21}$$

The dependence of t_{act} on the geometry becomes apparent from Equation 3.21. For instance, by increasing the nozzle length by a factor 2, t_{act} also increases by about the same factor and, for a given Wi, $\bar{Cr}$ decreases by a factor of 2 (Azzini 2019). A more into-depth investigation of the influence that geometric parameters such as the channel length or its expansion ratio have on t_{act} and thus on T_W is developed below.

Once t_{act} has been determined from the flow properties calculated for a given set of geometric parameters, one can try to find $t_{act} = f(\bar{Cr})$. Azzini 2019 arrives at a power law dependence:

$$t_{act} = k_1 \bar{Cr}^{-k_2} \tag{3.22}$$

In the equation above, k_1 and k_2 are fitting constants. Then, by combining Equation 3.20 and Equation 3.22, an expression for $Wi = f(\bar{Cr})$ is readily given by:

$$Wi = k_1 \bar{Cr}^{1-k_2} \tag{3.23}$$

It is worth noting that for $\bar{Cr} \longrightarrow 0$, i.e., $t_{act} \longrightarrow \infty$, then $\lim_{\bar{Cr} \longrightarrow 0} T_W = T_{sat}(s_0)$, where s_0 is the stagnation entropy. This corresponds to the limit of equilibrium, fully isentropic nucleation, illustrated in case I of Figure 3.3. An example of fitting t_{act} vs. $\bar{Cr}$ and Wi vs. $\bar{Cr}$ into functional expressions is shown in Figure 3.4 and Figure 3.5, in the case for H_2O and CO_2 with $T_{sat,r}(s_0) \equiv T_{sat}(s_0)/T_{cr} = 0.86$.

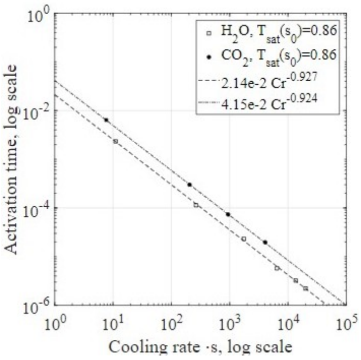

Figure 3.4: Activation time as a function of $\bar{Cr}$ for H_2O and CO_2 at $T_{sat,r}(s_0) = 0.86$ (Azzini 2019).

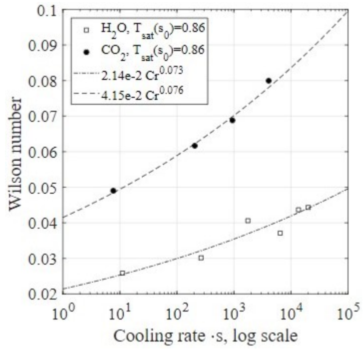

Figure 3.5: Wilson number as a function of $\bar{Cr}$ for H_2O and CO_2 at $T_{sat,r}(s_0) = 0.86$ (Azzini 2019).

In Figure 3.4 it can be seen that the slope of the lines is very similar for both fluids, so the same value of k_2 can be used for different substances. On the other hand, the coefficient k_1 has a clear dependence on $T_{sat,r}(s_0)$ and hence on both the fluid and reservoir conditions. This dependence can better be described by introducing the dimensionless temperature difference $\Delta\tilde{T}_{cr}$, defined by (Azzini 2019):

$$\Delta\tilde{T}_{cr} \equiv 1 - \frac{T_{sat}(s_0)}{T_{cr}} \tag{3.24}$$

By fitting the functional dependence $k_1(\Delta\tilde{T}_{cr})$ with an exponential function, one can write:

$$k_1(\Delta\tilde{T}_{cr}) = \hat{k}_1 \left[1 - \exp\left(-\Delta\tilde{T}_{cr}^{\,k_3}/\tau_T\right)\right] \tag{3.25}$$

There, $\hat{k}_1$, k_3 and τ_T are fitting coefficients. $\hat{k}_1$ is set to 0.0539 so that $k_1(\Delta\tilde{T}_{cr} \approx 1) \longrightarrow \hat{k}_1$. This further yields $k_3 = 1.359$ and $\tau_T = 0.0299$. Combining Equation 3.22 and Equation 3.23 and explicitly adding the dependence of k_1 on $\Delta\tilde{T}_{cr}$, Equation 3.26 is obtained (Azzini 2019):

$$Wi = k_1 \left(\Delta\tilde{T}_{cr}\right)^{\frac{1}{k_2}} t_{act}^{1-\frac{1}{k_2}} \tag{3.26}$$

For a given fluid and set of stagnation conditions, thus a set of $\Delta\tilde{T}_{cr}$ values, the previous equation can be used to write an explicit relation for $T_W(t)$, i.e. for the time variation of the Wilson temperature throughout an expansion process. In order to better understand the effect of varying $\bar{C}r$ on the characteristics of the flow, namely on the onset of condensation, Figure 3.6 is shown. There, it is clear that, the lower $\bar{C}r$, the longest time interval it takes for steam to achieve T_W, i.e., the intersection between the plots for T and T_W happens for a higher time instant t. This time instant is precisely the activation time t_{act}. In case b) of Figure 3.6, T_W coincides with T_{outlet} and hence the onset of condensation happens just at the end of the expansion, while for c) T_W is so much lower than T_{outlet} that it can be argued that condensation never occurs.

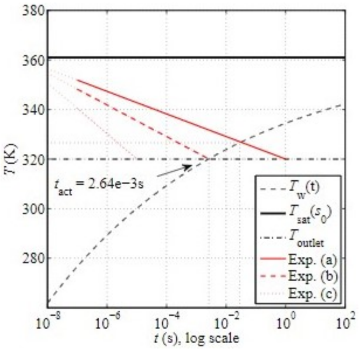

Figure 3.6: Plots of the flow temperature (T) and Wilson temperature (T_w) vs. time t for a)$\bar{C}r = 0.06s^{-1}$, b)$\bar{C}r = 24s^{-1}$, c)$\bar{C}r = 6000s^{-1}$ (Azzini 2019).

For cases II and III of Figure 3.3 condensation happens quickly and a considerable amount of heat is released in the gas surrounding the formed nuclei. Consequently, temperature increases, deviating from the original isentropic expansion, as shown in Figure 3.7. In this figure, the dashed line represents the local-to-total static pressure ratio according to the isentropic expansion without condensation, whereas the fully solid line represents the same ratio for the homogeneous nucleation case (II of Figure 3.3). The nozzle throat is denoted by the solid marked point. Non-equilibrium condensation takes place between the two white marked points (correspondent to points B and C in Figure 3.3). In this case, the flow is subsonic upstream of the throat, sonic at the throat and supersonic downstream (i.e. geometrically choked).

However, if enough heat is released due to condensation, the static pressure ratio will surpass the one at the throat of the nozzle. The flow is then said to be thermally choked, as it is equivalent to introducing a second throat to the channel. This is accompanied by shock waves, known as condensation shocks, downstream of which the flow becomes subsonic once again. It is then accelerated back into sonic speed at the equivalent ’thermal throat’, becoming supersonic further downstream. This is illustrated by Figure 3.8.

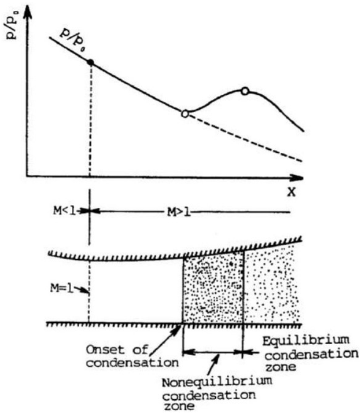

Figure 3.7: Homogeneous condensation without thermal choking (Matsuo et al. 1986).

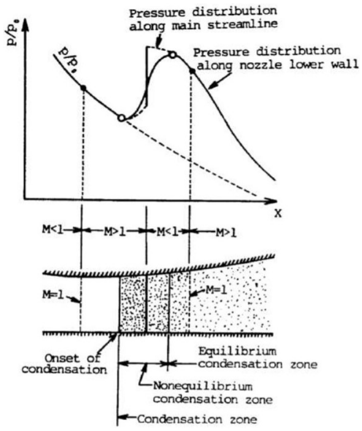

Figure 3.8: Homogeneous condensation with thermal choking (Matsuo et al. 1986).

At a particular position in the nozzle, there is a certain amount of added specific heat q_{max} for which thermal choking occurs, determined by Equation 3.27 (Pouring 1965). In this equation, c_p is the specific heat of the mixture, T_0 its total temperature and M is the local Mach number. As expected, for $M = 1$ we have $q_{max} = 0$.

$$q_{max} = c_p T_0 \frac{(M^2-1)^2}{2(\gamma+1)M^2\left[1+\frac{1}{2}(\gamma-1)M^2\right]} \tag{3.27}$$

q_{max} can be related to another quantity, the condensed mass fraction f_{max} that is needed for the flow to be thermally choked, defined by Equation 3.28. This equation is true within an uncertainty range of $\delta f_{max} = \pm\frac{1}{2}\left(\frac{q_{max}}{L_h}\right)^2$. A plot of this function is shown in Figure 3.9.

$$f_{max} = \frac{q_{max}}{L_h}\left(1 - \frac{q_{max}}{2L_h}\right) \tag{3.28}$$

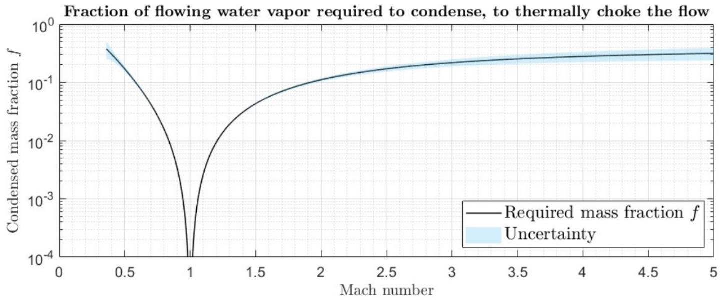

Figure 3.9: Mass fraction f_{max} and associated uncertainty of a flow of water vapor required to condense for thermal choking to occur (Sklavenitis 2022).

In order to have a more general understanding of the effects of condensation within a channel with a varying cross-sectional area, the concept of an inviscid compressible flow with heat addition (Rayleigh flow, Greitzer et al. 2004) is introduced:

$$\frac{dM^2}{M^2} = \frac{\left(1+\frac{\gamma-1}{2}M^2\right)}{1-M^2}\left[(1+\gamma M^2)\frac{dT_0}{T_0} - 2\frac{dA}{A}\right] \tag{3.29}$$

The previous equation states that change in the gas Mach number can be caused by either varying stagnation temperature or cross-sectional area. It can be rewritten as:

$$C(x) \equiv (1-M^2)\frac{dM^2}{dx} = M^2\left(1+\frac{\gamma-1}{2}M^2\right)\left[(1+\gamma M^2)\frac{d(\ln T_0)}{dx} - 2\frac{d(\ln A)}{dx}\right] \tag{3.30}$$

Analysing Equation 3.30 leads to the straight-forward conclusion that, in the absence of condensation (constant T_0), the flow Mach number is solely determined by the nozzle geometry. This corresponds to the isentropic quasi-1D nozzle flow model (Yeoh, Chapman, et al. 2015). Furthermore, $C > 0$ implies a tendency of the flow to become sonic, whereas $C < 0$ implies a divergence from that condition. $C = 0$ can be achieved by either reaching $M = 1$ or a maximum or minimum Mach number value. For the case of interest, let us consider a water vapour flow initially supersonic and accelerating in the divergent part of a nozzle. Condensation then starts, releasing latent heat to the still accelerating flow. For this to happen, $C(x)$ must be negative and thus the geometric term $2d(\ln A)/dx$ in Equation 3.30 must be dominant over the heat addition term $(1 + \gamma M^2)d(\ln T_0)/dx$. If, at a certain point, these two terms balance each other, then $C(x) = 0$ and a shock wave occurs, as in the case shown in Figure 3.8. The flow then becomes subsonic and $C > 0$, assuming condensation continues to be significant. This will cause the flow to accelerate back towards the sonic speed (thermal choking), at which point $C(x) = 0$ and $M = 1$ simultaneously. dM^2/dx is undetermined in this case. This condition enables continuous passage from subsonic to supersonic speeds (Pouring 1965). However, if $q < q_{max}$, then the sonic speed is not attained after the shock wave and once equilibrium ($S = 1$) is reached the subsonic flow will decelerate until the outlet due to the diverging cross-section.

3.2.2. Particle growth

After nucleation, grains continue to grow by absorbing water molecules that hit their surface. Thus, starting with the calculation of the collision rate of water molecules with the icy grains, the grains' growth rate equation (Equation 3.31) is immediately derived (Schmidt et al. 2008).

$$R'(x) \equiv \frac{dR}{dx} = \frac{\beta}{\sqrt{2\pi\gamma}\rho_{grain}} \left[\rho_{gas}(x) - \rho_{eq}^{(s.g.)}(T_{gas}(x))\right] \frac{c_s(x)}{u_{gas}(x)} \tag{3.31}$$

$$c_s \equiv \sqrt{\left(\frac{\partial p_{gas}}{\partial \rho_{gas}}\right)_{isentropic}} = \sqrt{\gamma R_{gas} T_{gas}} \tag{3.32}$$

In the previous equation, β is the condensation coefficient, defined as the fraction of absorbed molecules from those which hit the grain. This coefficient influences the overall brightness level of Cassini images for $\beta < 0.15$, with that influence weaker for $\beta > 0.2$. Other parameters such as the crack length and irregularity have only a mild influence on the plume brightness. As such, by comparison with the contours of plume brightness recorded by Cassini, β is set at 0.2 (Schmidt et al. 2008). $c_s(x)$ is the local speed of sound as defined by Equation 3.32 and $\rho_{eq}^{(s.g.)}$ is the saturated vapor density at the vapour-solid equilibrium and, analogously to $\rho_{eq}^{(l.g.)}$, it is calculated with an empirical relation for the vapour-solid equilibrium pressure $p_{eq}^{(s.g.)}$ (Equation 3.33, Schmidt et al. 2008) and the ideal gas law. As ρ_{gas} decreases slower than $\rho_{eq}^{(s.g.)}$, expansion rate and growth rate of grains are positively correlated (Schmidt et al. 2008).

$$p_{eq}^{(s.g.)}(T_{gas}) = \exp\left[(-2663.5/T_{gas} + 12.537)\ln(10)\right] \tag{3.33}$$

3.2.3. Particle size distribution

According to Schmidt et al. 2008, grain nucleation and growth happen mainly near the throat, where gradients of thermodynamic variables are higher. Hence, the grain size distribution is for all purposes set at this region. The size r of a grain at the outlet that nucleated at location x_0 in the channel can then be calculated with Equation 3.34, where the superscript "∞" denotes quantities at the outlet of the channel.

$$r(x_0) = R^{\infty} - R(x_0) \tag{3.34}$$

The distribution of the variable hereafter denoted as r can be found by starting with the conservation law for the grain particles (Equation 3.35, Schmidt et al. 2008), where n is the particle density.

$$\gamma_{nuc}(x_0)A(x_0)dx_0 = n(x_0)u_{gas}(x_0)A(x_0) = n(\infty, x_0)u^{\infty}A^{\infty} \tag{3.35}$$

The particle size distribution at the outlet of the channel is finally given by Equation 3.36 (Schmidt et al. 2008), where $x_0(r)$ is the inverse function of $r(x_0)$, or in other words, the location x_0 at which a particle with radius r at the outlet nucleated.

$$P(r)dr = \frac{\gamma_{nuc}(x_0(r))}{u^{\infty}} \left| \frac{dr}{dx_0} \right|^{-1} \frac{A(x_0)}{A^{\infty}} dr \tag{3.36}$$

Figure 3.10 shows thermodynamic profiles of gas density, solid fraction (condensed mass in the plot), temperature, sound speed and gas speed, as well as grain size distribution at the outlet for a randomly generated channel. There, it can clearly be seen that nucleation begins just downstream of the channel geometric throat, where solid fraction starts rising and the released heat is absorbed back by the vapour, increasing temperature and density and decreasing gas speed. The grain sizes at the vent are vastly in the range 0.1-10 μm.

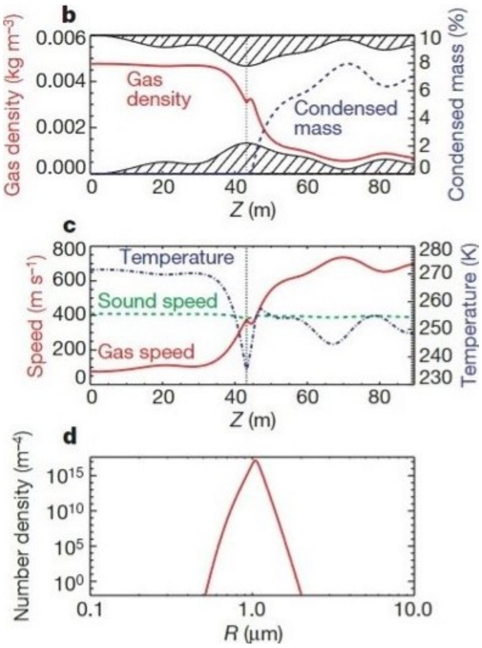

Figure 3.10: Example of a grain size distribution for a randomly generated channel (Schmidt et al. 2008).

3.2.4. Dynamics of the grains

Similarly as for the grain size growth, the interaction of the grains with the gas, is also described by gas-kinetic theory. This yields the equation of motion for a grain in the gas (Equation 3.37, Schmidt et al. 2008).

$$m_{grain} \frac{du_{grain}}{dt} = b\pi R^2 \rho_{gas} V_{th} (u_{gas} - u_{grain}) \tag{3.37}$$

In Equation 3.37, u_{grain}, R and $m_{grain} = (4/3)\pi R^3 \rho_{grain}$ are, respectively, the velocity, radius and mass of the grain. The remaining parameters are $b = 4/3 + (1-\beta)\pi/6$ and the average molecular speed $V_{th} = (8k_B T_{gas}/(\pi m))^{1/2}$, where m is the mass of a water molecule. Modelling collisions of the grains with channel walls as a random Poisson process, the probability to collide with a wall during an infinitesimal time interval dt is dt/τ, where τ is the average time between successive collisions with the walls. Now Equation 3.38 (Karagiannis 2020) is used to define the molecular mean free path λ. There, $\mu_{gas}[Pa \cdot s]$ is the dynamic viscosity of the gas. Noting that λ and τ are related by the relation $\lambda = u_{gas}\tau$, the probability that no collision has occurred during a time interval (0,t) is given by $exp[-t/(\lambda/u_{gas})]$. Assuming that the velocity of a grain is reduced to zero in a collision (completely dissipative collisions) and recalling that Equation 3.37 governs the particle dynamics between collisions, the time interval between its last wall collision and the instant when the particle leaves the channel determines the velocity of that grain. After some algebraic manipulation that can be found in Schmidt et al. 2008, the velocity distribution for grains of size R is given by Equation 3.39, where $R_c \equiv \rho_{gas}^{\infty}/\rho_{grain}V_{th}^{\infty}[1+\pi/8(1-\beta)]\lambda/u_{gas}^{\infty}$ is the critical radius of the grain.

$$\lambda = \frac{\mu_{gas}}{p_{gas}}\sqrt{\frac{\pi k_B T_{gas}}{2m}} \tag{3.38}$$

$$P(u_{grain}) = \frac{R}{R_c}\left[1+\frac{R}{R_c}\right]\frac{u_{grain}}{u_{gas}^{\infty}}\left[1-\frac{u_{grain}}{u_{gas}^{\infty}}\right]^{\frac{R}{R_c}-1} \tag{3.39}$$

It then follows that the average grain velocity is given by Equation 3.40.

$$< u_{grain}(R) >= \left(1+\frac{R}{2R_c}\right)^{-1} u_{gas} \tag{3.40}$$

3.3. Application of the quasi-1D condensation model: Wilson point estimation

In this section, a parametric study of the onset of condensation is performed. For that, a baseline channel geometry is generated with Equation 3.41, where $\bar{y}_{channel} = 0.06m$, $A = 0.01m$ and $L = 1.5m$. This geometry (Figure 3.11) is then modified such that the influence of different channel length, expansion ratio and throat location on the location of the onset of condensation are taken into account.

$$y = \bar{y}_{channel} + A\cos\left(\frac{2\pi}{L}x\right) \tag{3.41}$$

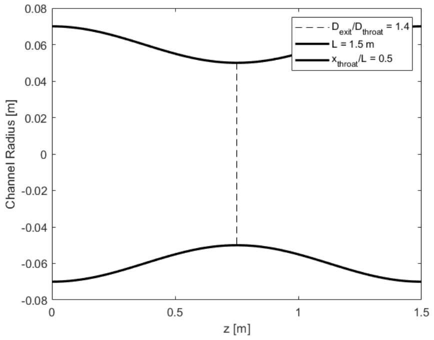

Figure 3.11: Baseline geometry generated with Equation 3.41.

The results of this parametric study are shown in Figure 3.12 and Figure 3.13. Particularly, it can be concluded that the larger the channel length or the closer to the vent the throat is located, the higher the activation time and hence the lower the average cooling rate. This in turn means that the Wilson point is smaller in such cases and thus the condensation process happens at a rather gradual rate, approaching case III of Figure 3.3. The opposite situation happens for the cases with higher geometric expansion ratio or throat location closer to the reservoir.

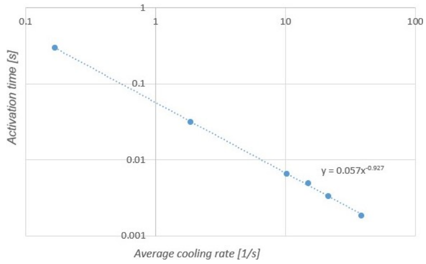

Figure 3.12: t_{act} vs. $\bar{Cr}$ for the simulation settings (left to right): $L = 150m$, $L = 15m$, $L = 3m$, $x_{throat}/L = 0.75$, baseline, $x_{throat}/L = 0.25$.

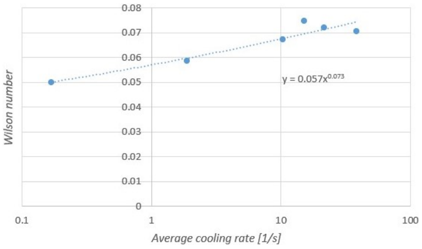

Figure 3.13: Wi vs. $\bar{Cr}$ for the simulation settings (left to right): $L = 150m$, $L = 15m$, $L = 3m$, $x_{throat}/L = 0.75$, baseline, $x_{throat}/L = 0.25$.

4

Multi-phase 2D model for condensation

In this chapter, a more complete condensation model which takes into consideration multi-phase, 2D effects is proposed. First, the model is presented in terms of its conservation and constitutive equations in section 4.1. Then, section 4.2 explains the numerical implementation of the equations presented previously. Finally, section 4.3 provides a validation of the model by applying the numerical solver to a known case from literature with available experimental data.

4.1. Wet steam model

A wet steam model based on Karagiannis 2020 and Wen et al. 2019 is described in this section. Wen et al. 2019 performed simulations of non-equilibrium homogeneous condensation of water vapour in supersonic flows with shock waves, to be taken advantage of to separate water vapour from saturated natural gas. This can be adapted to simulate the interactions between vapour and solid grains in the plumes of Enceladus. Equation 4.1 describes such model with the usual mass, momentum and energy conservation equations. There, τ_{ij} is the viscous stress tensor (Equation 4.2), $k_{eff} \equiv k_v + k_t$ is the effective thermal conductivity (with k_v and being respectively the molecular and turbulent thermal conductivity), E is the total specific internal energy of the vapour (Equation 4.3), H is the total specific enthalpy of the vapour (Equation 4.4) and H_p is the total specific enthalpy of the droplet (Equation 4.5). The remaining parameters are described in the following paragraphs.

$$
\begin{aligned}
&\frac{\partial \rho}{\partial t} + \frac{\partial(\rho u_i)}{\partial x_i} = -\Gamma \\
&\frac{\partial(\rho u_i)}{\partial t} + \frac{\partial(\rho u_i u_j)}{\partial x_j} = -\frac{\partial p}{\partial x_i} + \frac{\partial \tau_{ij}}{\partial x_j} - u_i \Gamma \\
&\frac{\partial(\rho E)}{\partial t} + \frac{\partial(\rho u_i H)}{\partial x_i} = \frac{\partial}{\partial x_i}\left(k_{eff}\frac{\partial T}{\partial x_i} + \tau_{ij} u_j\right) - H_{droplet}\Gamma
\end{aligned}
\tag{4.1}
$$

$$\tau_{ij} = \mu\left(\frac{\partial u_i}{\partial x_j} + \frac{\partial u_j}{\partial x_i} - \frac{2}{3}\frac{\partial u_k}{\partial x_k}\delta_{ij}\right) \tag{4.2}$$

$$E \equiv e + \frac{1}{2}u_i u_i \tag{4.3}$$

$$H \equiv h + \frac{1}{2}u_i u_i \tag{4.4}$$

$$H_p = H - L_h \tag{4.5}$$

To fully describe this multi-phase flow, two additional conservation equations must be added: one for the solid fraction f (Equation 4.6) and the other for the droplet number per volume (density) N (Equation 4.7). For the simulation case where wall friction and heat convection are considered, the $k - \omega$ shear stress transport (SST) turbulence model is used, as it is known to achieve good accuracy in predicting high Reynolds number Re (typically higher than 10^7) supersonic flows and non-equilibrium condensation phenomenon (Zhang et al. 2019).

$$\frac{\partial(\rho f)}{\partial t} + \frac{\partial(\rho u_i f)}{\partial x_i} = \Gamma \tag{4.6}$$

$$\frac{\partial(\rho N)}{\partial t} + \frac{\partial(\rho u_i N)}{\partial x_i} = \rho\gamma_{nuc} \tag{4.7}$$

Γ is the condensation mass rate per unit vapour volume per unit time, defined by Equation 4.8 (Zhang et al. 2019), where r is the mean droplet radius and r_c is the Kelvin-Helmholtz critical droplet radius, calculated with Equation 4.9 whose parameters have already been introduced in chapter 3.

$$\Gamma = \frac{4}{3}\pi r_c^3 \rho_{grain}\gamma_{nuc} + 4\pi r^2 \rho_{grain} N \frac{dr}{dt} \tag{4.8}$$

$$r_c = \frac{2 v_m \sigma}{k_B T_{gas} \ln S} \tag{4.9}$$

As for the growth rate of droplets due to evaporation and condensation, let us consider a grain which has just condensed and its surroundings, as in Figure 4.1. As temperature decreases slower for the grains than for the surrounding vapour, $T_f > T(r_1)$ (Lai et al. 1993). It also follows that $T(r_2) > T_g$. For particle growth to occur, it is required that an amount of heat $Q(r_2) > Q(r_1)$, so that the surrounding vapour releases a larger amount of heat to the outside than it absorbs from the nucleated grain (Lai et al. 1993). Equation 4.10 describes the energy balance of a droplet, where λ_g is the coefficient of convective heat transfer from the gas to the droplet, T_p is the droplet temperature and c_{ice} is the specific heat of ice.

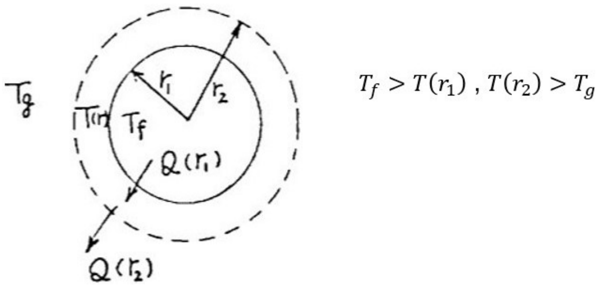

Figure 4.1: Sketch of a nucleated particle and its surroundings (Lai et al. 1993).

$$L_h \frac{dm_{grain}}{dt} = 4\pi r^2 \lambda_g (T_p - T) + m_p c_{ice} \frac{dT_p}{dt} \tag{4.10}$$

Due to the fact that the droplets are minuscule and hence their heat capacity is negligible and their thermal relaxation time is lower than that of the flow by orders of magnitude (Lamanna 2000), the last term on the right-hand side of Equation 4.10 can be omitted. That equation can then be rewritten and solved for dr/dt, yielding Equation 4.11.

$$4\rho_{grain}\pi r^2 L_h \frac{dr}{dt} = 4\pi r^2 \lambda_g (T_p - T) \Leftrightarrow \frac{dr}{dt} = \frac{\lambda_g (T_p - T)}{L_h \rho_{grain}} \tag{4.11}$$

In turn, λ_g can be estimated in several ways. However, the one which is most widely used and suitable for low pressures is the one proposed by Young 1980, Equation 4.12, where ν is a modelling correction coefficient (Equation 4.13, Wen et al. 2019), Kn is the local Knudsen number (Equation 4.14) and $Pr \equiv c_p\mu/k_v$ is the Prandtl number. In the definition of ν, q_c is the condensation coefficient and α is a modelling parameter ($q_c = 1.0$ and $\alpha = 1.0$ according to Wen et al. 2019).

$$\lambda_g = \frac{k_v}{r} \frac{1 - r_c/r}{1 + 3.78(1-\nu)\frac{Kn}{Pr}} \tag{4.12}$$

$$\nu = \frac{R_{gas}T_{eq}^{(s,g)}}{L_h}\left(\alpha - 0.5 - \frac{2-q_c}{2q_c}\frac{(\gamma+1)c_pT_{eq}^{(s,g)}}{2\gamma L_h}\right) \tag{4.13}$$

$$Kn \equiv \frac{\lambda}{2r} \tag{4.14}$$

Finally, an explicit expression for dr/dt can be written, yielding Equation 4.15. Once again, it is outlined that the droplet radius r used in this equation is an average value and hence it is just an attempt to accurately represent the actual size distribution that occurs throughout the flow.

$$\frac{dr}{dt} = \frac{k_v\left(T_p - T_{gas}\right)}{\rho_{grain}L_h r}\frac{1 - r_c/r}{1 + 3.78(1-\nu)\frac{Kn}{Pr}} \tag{4.15}$$

Although there is no settled theory on the exact moment of the onset of nucleation, throughout this work a minimal value of $2.75 \cdot 10^{-10}m$ for the droplet size is used, as it is the average distance between two oxygen atoms in the ice molecular bonds, according to Huang et al. 2013. The droplet size at the outlet $r(L, x_0)$ for a particle formed at a channel location x_0 is then possible to determine by Equation 4.16, where L is the channel length, r_0 is the droplet size at x_0 and u is the convective velocity (here assumed to be equal to that of the flow). A schematic explanation of Equation 4.16 is shown in Figure 4.2. The array of droplet sizes (one for each x_0) obtained with this equation can finally be used to retrieve the droplet size distribution at the channel outlet.

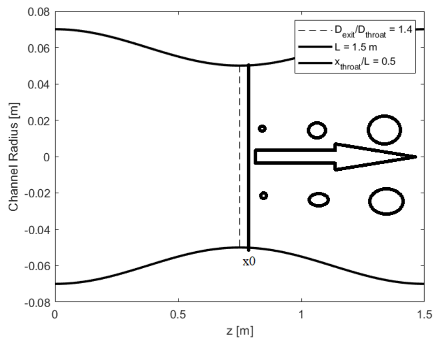

Figure 4.2: Scheme to determine the droplet size distribution at the channel outlet.

$$r(L, x_0) = r_0 + \int_{x_0}^{L} \frac{dr}{dt}\frac{1}{u}dx \tag{4.16}$$

It is particularly important to notice the dependence of the droplet growth rate on the Knudsen number. This dimensionless number is a measure of the degree of rarefaction of the flow. According to Tsien 1946, the following ranges of Knudsen number (based on the channel diameter) can be used:

- $Kn \leq 0.001$: continuum regime;
- $0.001 < Kn \leq 0.1$: slip-flow regime;
- $0.1 < Kn \leq 10$: transitional regime;
- $Kn \geq 10$: free molecular regime.

As pressures typically found in the plumes of Enceladus or those simulated in the laboratory are very low (a few hundreds of Pa), it becomes important to estimate the Knudsen number throughout the plume and interpret it in light of the applicability of the continuous flow regime, where standard fluid dynamics models can be applied. Typical Knudsen numbers to be found throughout this work lie within the range 0.0001-0.01.

4.2. Numerical implementation

The model described by Equation 4.1 is simulated in *OpenFOAM*, an open source CFD software written in C++ and relatively straightforward to use. *OpenFOAM* has several solvers which could potentially be used in the context of the problem in hands. These solvers mainly use one of two main approaches: density based (*rhoCentralFoam*) or pressure based (*sonicFoam*). In the former case, the continuity equation is used to determine the density and the pressure follows from the equation of state, whereas in the latter the pressure field is first determined by solving a pressure predictor-corrector equation. According to Marcantoni et al. 2012, *rhoCentralFoam* outperforms *sonicFoam* in terms of resolution accuracy and numerical performance. Therefore, it was chosen to perform the simulations needed in this project.

4.2.1. Numerical implementation of the governing equations

The conservation equations that are solved in the wet steam model are discretized by using the finite volume illustrated in Figure 4.3. There, P and N are points connected by the vector $\mathbf{d_{P,N}}$, central to computational cells bounded by face f with normal unitary vector $\mathbf{S_f}$.

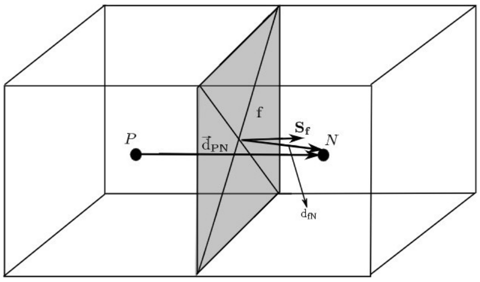

Figure 4.3: Schematic of the finite volume discretization of the *rhoCentralFoam* solver (Marcantoni et al. 2012).

Starting with a generalized field variable Ψ, the respective conservative equation can be written as Equation 4.17, where S_Ψ is the source term.

$$\frac{\partial(\rho\Psi)}{\partial t} + \nabla\cdot[\mathbf{u}(\rho\Psi)] = S_\Psi \tag{4.17}$$

The convective term of Equation 4.17 can be integrated over each control volume, converted into a surface integral by divergence's theorem and then linearised as Equation 4.18, where $\phi_f = \mathbf{S}_f \cdot \rho\mathbf{u}_f$.

$$\int_V \nabla\cdot[\mathbf{u}(\rho\Psi)] = \int_S d\mathbf{S}\cdot[\mathbf{u}(\rho\Psi)] \approx \sum_f \mathbf{S}_f \cdot \rho\mathbf{u}_f\Psi_f = \sum_f \phi_f\Psi_f \tag{4.18}$$

Compressible flows allow for information to be transported by both convection and wave propagation. Therefore, the right-hand side of Equation 4.18 can be rewritten as Equation 4.19, where the flux at any given face is split in an outward (+) and inward (-) direction, with a weight α being assigned to each component.

$$\sum_f \phi_f\Psi_f = \sum_f [\alpha\phi_{f+}\Psi_{f+} + (1-\alpha)\phi_{f-}\Psi_{f-}] \tag{4.19}$$

The local volumetric flux ψ_f at the local speed of propagation at each face, in turn associated to the local speed of sound c in each direction ($c_{f\pm} = \sqrt{\gamma RT_{f\pm}}$), is calculated with Equation 4.20.

$$\psi_{f\pm} = max(c_+|S_f| \pm \phi_+, c_{f-}|S_f| \pm \phi_-, 0) \tag{4.20}$$

The weight α is finally calculated based on the method of Kurganov and Petrova (Kurganov et al. 2007) as in Equation 4.21.

$$\alpha = \frac{\psi_{f+}}{\psi_{f+} + \psi_{f-}} \tag{4.21}$$

Due to the presence of steep gradients at the location of onset of nucleation, a second-order upwind scheme is used to reconstruct the variables f and N from the cells (Karagiannis 2020).

4.2.2. Linearisation of the source terms

For finite-volume methods, the convergence to the solution is faster when the matrix containing the coefficients of the linear set resulting from the discretization of the governing equations is diagonally dominant. That is, the entries along the diagonal are larger in magnitude than the rest of the entries along their respective rows combined. The source terms in the momentum component of Equation 4.1 and Equation 4.6 depend on the variable that is being solved for, U and f respectively. Due to the impulsivity of the metastable condensation phenomenon, in the condensation region the rate of change of these source terms dominates over that of the rest of the terms in their respective equations. If they are directly included in the solution matrix, they can negatively influence the solver's convergence behaviour. In order to amend this mathematically, each of those source terms can be expanded using the respective Taylor series and taking it up to the first order term. This yields a linearised version of those source terms, with an active (dependent on the correspondent variable) and passive components. The linearised version of the source term for f ($S_f = \Gamma$) is written as Equation 4.22, where the superscript 'o' denotes the old time-step and the prime denotes the active coefficient, i.e. the derivative of the source term with respect to the variable being conserved, f in this case. An example of the implementation of this algorithm is given in Appendix A.

$$S_f = S_f^0 + S_f'(f - f^0) \tag{4.22}$$

$$S_f^0 = \frac{4}{3}\pi r_c^3 \rho_{grain}\gamma_{nuc} + 4\pi r^2 N \rho_{grain}\frac{dr}{dt} \tag{4.23}$$

$$S_f' = \frac{3\rho}{r}\frac{dr}{dt} \tag{4.24}$$

4.3. Validation of the chosen model

In order to validate the above described model, a nozzle with two conical branches (convergent-divergent) was chosen. This is because reliable experimental data is available for this geometry. Another reason to choose this geometry lies in the possibility to test a rather extreme case of a sharp throat, which provides for huge property gradients in its neighbourhood. A sketch of this geometry is shown in Figure 4.4. The experimental conditions are specified in Table 4.1. According to the International Association for the Properties of Water and Steam (IAPWS), liquid water density was assumed constant at 997 kg/m^3 and the latent heat of evaporation at 2.260 MJ/kg. These assumptions are fine, as both quantities have a weak dependence on temperature for the range of values to be analysed.

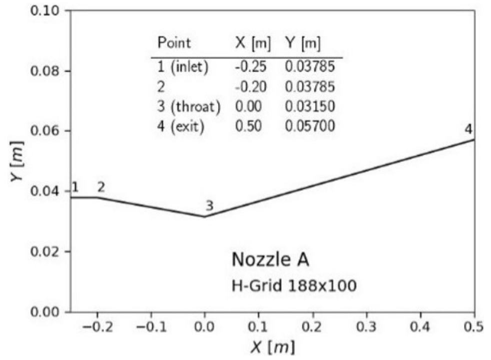

Point	X [m]	Y [m]
1 (inlet)	-0.25	0.03785
2	-0.20	0.03785
3 (throat)	0.00	0.03150
4 (exit)	0.50	0.05700

Figure 4.4: Sketch of the nozzle geometry to be used in the validation of the proposed model (Moore et al. 1973).

Boundary condition	Value
T_0	354.6 K
p_0	25 kPa

Table 4.1: Inlet stagnation conditions for the experiment by Moore et al. 1973.

A comparison between the results obtained with the proposed model and experimental data for the nozzle geometry by Moore et al. 1973 is shown in Figure 4.5.

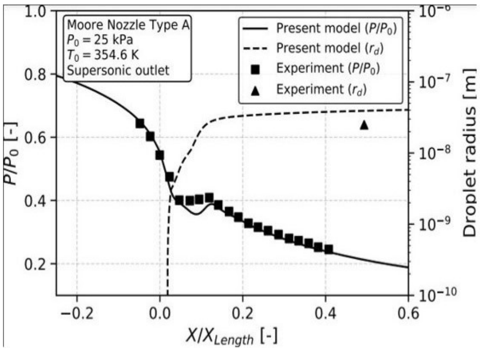

Figure 4.5: Validation of the proposed model by Moore et al. 1973

As suggested by the previous figure, there is only a small deviation between simulation and experimental pressure ratio results close to the channel throat, possibly because the actual channel geometry is not known there. Little information is known about the average droplet radius for the experiment. However, available data from a single experimental point suggests the same order of magnitude ($10^{-8}\ m$) for both simulation and experiment. The flow propagating through the nozzle described in Figure 4.4 and compared to experimental data in Figure 4.5 is now visualised along the channel. Figure 4.6 to Figure 4.15 show some vapour and solid properties representative of the flow through nozzle A.

Figure 4.6: Contour of the static pressure field (SI values) for nozzle A.

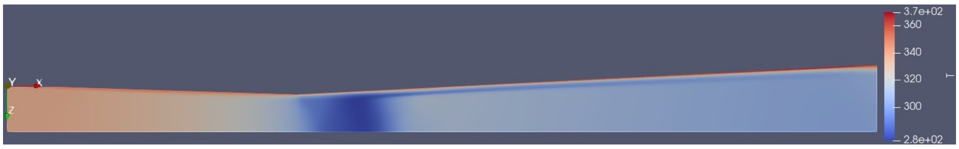

Figure 4.7: Contour of the static temperature field (SI values) for nozzle A.

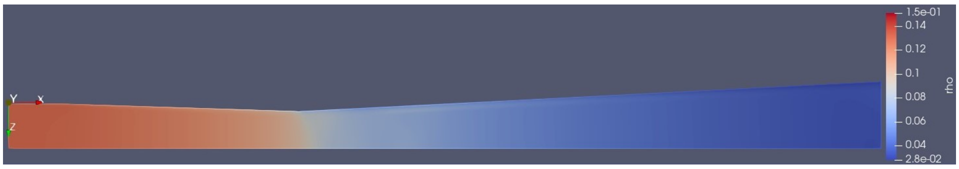

Figure 4.8: Contour of the density field (SI values) for nozzle A.

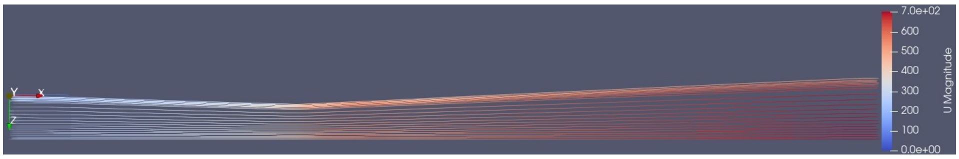

Figure 4.9: Shape of the velocity streamlines (SI values) for nozzle A.

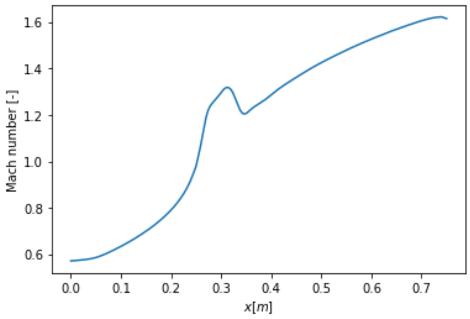

Figure 4.10: Mach number along the centerline of nozzle A.

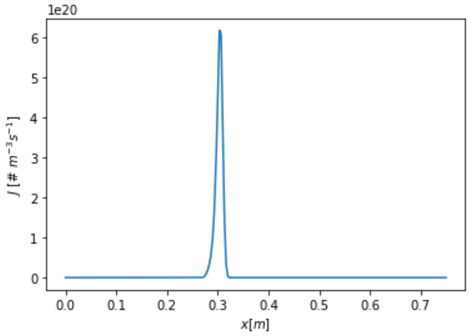

Figure 4.11: Nucleation rate along the centerline of nozzle A.

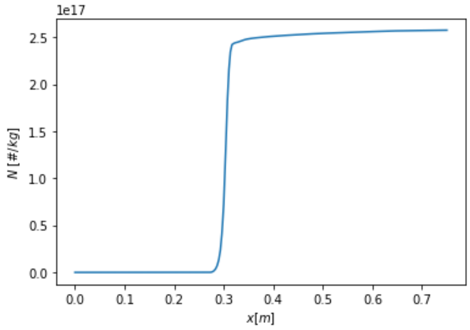

Figure 4.12: Droplet number along the centerline of nozzle A.

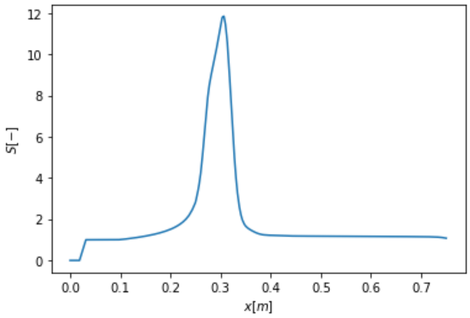

Figure 4.13: Supersaturation ratio along the centerline of nozzle A.

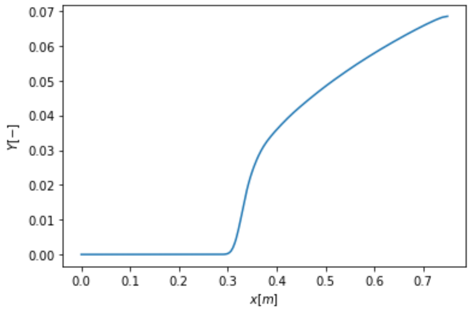

Figure 4.14: Solid fraction along the centerline of nozzle A.

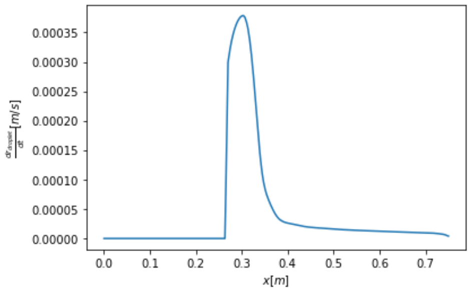

Figure 4.15: Droplet growth rate along the centerline of nozzle A.

From the figures above, it can be seen that, as steam expands through the nozzle, the saturation ratio (Figure 4.13) quickly rises above 1 and keeps steeply increasing until reaching a maximum just above 11. According to Equation 4.9, this leads to a decrease in the local value of the critical radius, making stable droplets easier to form. Liquid water clusters nucleate at rates in the order of $10^{20}/(m^3s)$ (Figure 4.14) and immediately start to grow (Figure 4.15). As this happens, latent heat is released and sub-cooling decreases. The resulting pressure rise yields a lower supersaturation ratio and the flow tends towards saturation equilibrium. Once supersaturation is low enough for nucleation to stop, no more droplets are generated and the number of droplets stays approximately constant (Figure 4.12). As pressure rises, the expansion slows, yielding a deceleration of the flow, which is apparent in Figure 4.9. The consequent temperature rise yields a higher sonic velocity, decreasing the Mach number (Figure 4.10).

5

Definition of the test-cases

In order to study the plumes of Enceladus, suitable geometries are built with *blockMesh*, the native meshing software of *OpenFOAM*. In section 5.1, the test cases used to investigate the influence that the channel geometry and the reservoir conditions have on the physical behaviour of the plumes are summarized. In section 5.2 the computational domain correspondent to the baseline physical geometry to be considered in this work is shown. In section 5.3 a description of the numerical implementation of the axisymmetric multi-phase solver is given. In section 5.4 an explanation of the methodology used to perform a similarity analysis between the laboratory and Enceladus scales is provided. Finally, in section 5.5 the basis to compare numerical simulation results with laboratory experiments performed by Verhoeff 2023 is set up.

5.1. Test cases

Table 5.1 summarizes the different simulation settings used throughout the first part of this work to study the dependence of the characteristics of the plumes on geometry and reservoir conditions.

n	Test case	Brief description
1	Isentropic model	-
2	Multi-phase model	includes condensation
3	Longer channel	channel length L doubled
4	Higher area ratio	A_{exit}/A_{throat} increased
5	Different throat location	x_{throat}/L varied
6	Viscous flow effects	includes friction and heat convection
7	Different reservoir temperature	T_{res} varied
8	Different reservoir pressure	p_{res} varied

Table 5.1: Cases to be studied in this work.

Cases 1 and 2 are used as a baseline comparison between an isentropic model and one including condensation. Cases 3, 4 and 5 are used to investigate the effects of changing the channel geometry on the flow properties. Case 6 adds viscous and heat convection effects to case 2. Finally, cases 7 and 8 study the effects of different stagnation conditions.

5.2. Geometry

In order to simulate cases 1, 2, 6, 7 and 8 of Table 5.1, the baseline geometry defined in section 3.3 is used. Figure 5.1 shows the computational domain (mesh) used to solve the flow through the baseline channel. The number of cells in each direction was chosen such that the nucleation and particle growth processes are accurately solved in all the domain. For a compromise between accuracy and solver speed, a mesh with 150 cells in the longitudinal direction and 60 in the radial one was chosen. It has a thickness of 1 cell, so that *OpenFOAM* interprets it as a 2D mesh. For the same reason, lateral faces are set to type *empty*. The expansion ratio between the inlet and the throat cells is 1/2 (cells at the throat are half the size of those at the inlet, so that this region is solved with enough accuracy to capture nucleation), 2 between the throat and the outlet and 1/50 between the axis of symmetry and the wall (1/100 for the test case with wall friction and heat convection so that the boundary layer is accurately solved). The boundaries of the computational domain are illustrated by Figure 5.2.

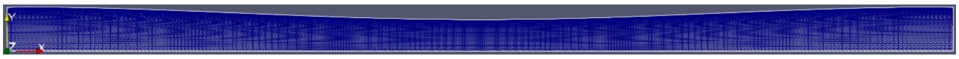

Figure 5.1: Overview of the computational domain.

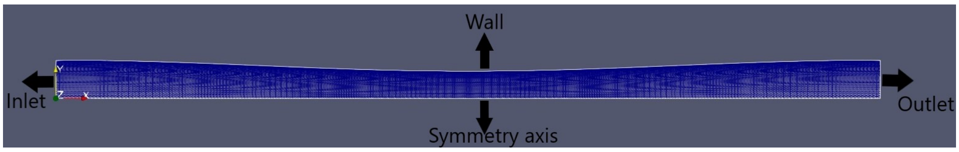

Figure 5.2: Overview of the computational domain boundaries.

5.3. Numerical setup

5.3.1. Boundary Conditions

The prescribed types for the boundary conditions are summarized and explained below.

Inlet

Stagnation conditions are specified for pressure and temperature, so that the inflow is subsonic compressible. For velocity, a zero gradient condition is prescribed, such that the flow is pressure-driven.

Outlet

As the outflow is supersonic and hence it cannot influence the flow upstream, no thermodynamic property can be prescribed. Instead, zero gradient conditions are prescribed to pressure and temperature. For velocity, an *inletOutlet* condition is specified. This is equivalent to a zero gradient if the velocity vector points outwards, switching to a fixed value condition in case there is reversing flow.

Wall

For the most part of this work, no friction nor heat convection with the walls are considered. Even though this can be considered questionable, according to authors such as Barschdorff et al. 1972, given smooth nozzle shapes, the boundary layer influence can be neglected. Hence, a slip condition is prescribed for the velocity. An exception is made for the simulation case that includes wall friction and heat convection, for which a no slip condition is instead used. For pressure and temperature, zero gradient conditions are prescribed, except for the case with wall friction and heat convection, for which the wall temperature T_w is set to 273.16 K.

Symmetry axis

As this is not a physical boundary, but instead a method to reduce the size of the computational domain by half, a symmetry condition is prescribed to all variables.

For the solid phase variables, droplet number N and solid fraction f, zero gradient conditions are prescribed at all the boundaries, such that they are only influenced by the behaviour of the flow itself.

5.3.2. Numerical solution methodology

Past works such as Blondel 2014 extensively explored different numerical schemes for the simulation of non-equilibrium condensation flows. A good summary of such schemes is also presented by Karagiannis 2020. Therefore, in order not to make this subsection too exhaustive, the numerical schemes used in the simulations required in this work are simply stated with a brief explanation attached.

For result reliability, the temporal terms are discretized with a second-order Crank-Nicholson scheme (Crank et al. 1996), with a weight factor of 0.9 following *OpenFOAM* guidelines. The divergence terms are dealt with by the algorithm of Kurganov and Petrova (Kurganov et al. 2007), already embedded in the solver and described in section 4.2. As for the Total Variation Diminishing (TVD) limiter implemented by the method of Kurganov and Petrova, Blondel 2014 concludes that the one sugested by Albada et al. 1997 gives the most convenient trade-off between precision and numerical performance. The solid phase variables N and f are not reconstructed from the cell faces using a TVD scheme, due to the highly steep gradients those variables attain in the flow region where nucleation first starts.

Instead, they are treated with a second order unbounded linear-upwind scheme (Warming et al. 1976). The Laplacian term in the energy equation is treated with a simple Gauss linear discretization. The surface-normal gradient of velocity in the energy equation is assigned a standard central-difference, corrected surface-normal gradient scheme. The remaining gradient terms in the conservation laws are discretized with a least-squares scheme, whose extrapolated values are bounded by the maxima and minima of the neighbouring cells.

5.3.3. Numerical initialisation

Due to the fact that for compressible flows the propagation of the solution is bounded by a time step determined at the local sonic velocity, convergence can be slow in regions where the flow is subsonic (Marcantoni et al. 2012). For this reason, in order to speed convergence, Riemann initial conditions are used to initialize the pressure, temperature and velocity variables. For the baseline channel case, in the convergent region of the channel the solution is initialized with 600 Pa and 270 K (close to the triple point values), whereas for the divergent region it is initialized with 300 Pa and 270 K. This is such that convergence is optimized with respect to the flow characteristics of the region, e.g., for the divergent, supersonic flow region, pressure is initialized in such a way that indicates the flow will be supersonic and therefore the propagation of the solution is made faster. As for the solid phase variables N and Y, they are initialized with the value 0 everywhere in the computational domain, so that condensation comes naturally from flow physics.

5.4. Length scale analysis: Enceladus vs. laboratory

In order to perform a scale comparison, it is useful to focus on the length of the divergent portion of the channel L_{div}, as illustrated in Figure 5.3. From that, a more useful parameter is defined as in Equation 5.1, which measures the effective geometric expansion ratio of the channel, in expansion per unit length of the divergent portion of the channel. This parameter is used to directly compare the results obtained at the laboratory with Enceladus scales.

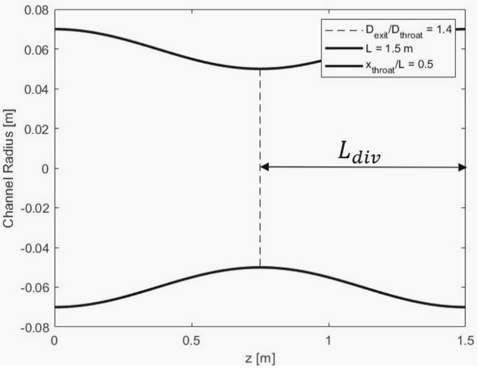

Figure 5.3: Geometric definition of the channel divergent length.

$$\epsilon \equiv \frac{A_{exit}/A_{throat}}{L_{div}} \tag{5.1}$$

5.5. Comparison with laboratory experimental data

Figure 5.4 shows the channel geometry used to compare the simulation results according to the model proposed in chapter 4 with laboratory experimental data, based on a 3D-printed model made of polylactic acid (PLA) designed by Verhoeff 2023. The main geometric parameters of this channel are outlined in Table 5.2. Relevant boundary conditions used in the numerical simulation of this channel are presented in Table 5.3. Laboratory experiments performed by Verhoeff 2023 show that the wall temperature is close to uniform for much of the channel length. In order to verify this numerically, two different boundary conditions are tried for the energy equation at the wall: adiabatic (thermally insulated wall) and isothermal (constant wall temperature).

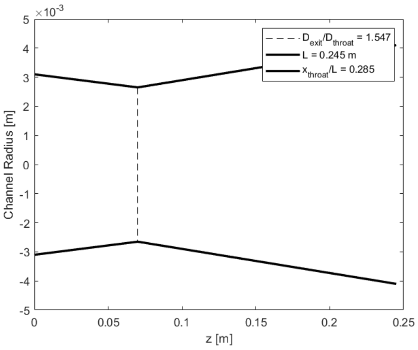

Figure 5.4: Channel model 1 geometry by Verhoeff 2023.

Parameter	Value
Inlet diameter	6.2 mm
Throat diameter	5.3 mm
Vent diameter	8.2 mm
Throat fillet radius	50 mm
Vent-to-throat area ratio	2.394
Converging angle	0.737
Expansion angle	0.949

Table 5.2: Geometric parameters of channel model 1 (Verhoeff 2023).

Boundary condition	Value
T_{res}	290.4 K
p_{res}	1968.2 Pa
T_w (isothermal wall)	295 K

Table 5.3: Boundary conditions used to simulate channel model 1.

6

Results and discussion

In this chapter, the results for the simulation settings described in chapter 5 are presented and discussed. In section 6.1, the results obtained from the simulations done to investigate the influence of the channel geometry are shown and analysed. Similar simulations are performed in section 6.2 but this time considering viscous effects (wall friction and heat convection) and different reservoir conditions (temperature and pressure). A similarity analysis between the laboratory and Enceladus scales is then drawn upon in section 6.3. section 6.4 compares the 2D flow model described in chapter 4 and used in this work to the quasi-1D model described by Hijden 2021. In section 6.5 a comparison between numerical simulation and laboratory experimental data retrieved by Verhoeff 2023 is laid out. Finally, in section 6.6, the different parameters influencing the plumes characteristics are discussed.

6.1. Effects of the channel geometry

6.1.1. Baseline case

The results for the simulations with the baseline geometry are presented in Figure 6.2 to Figure 6.9.

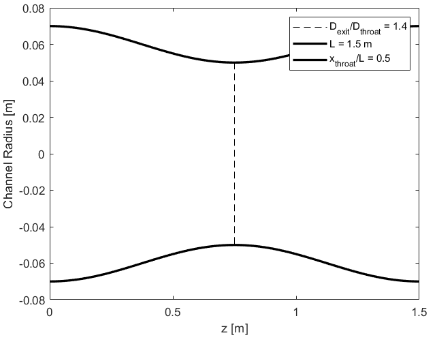

Figure 6.1: Baseline channel geometry.

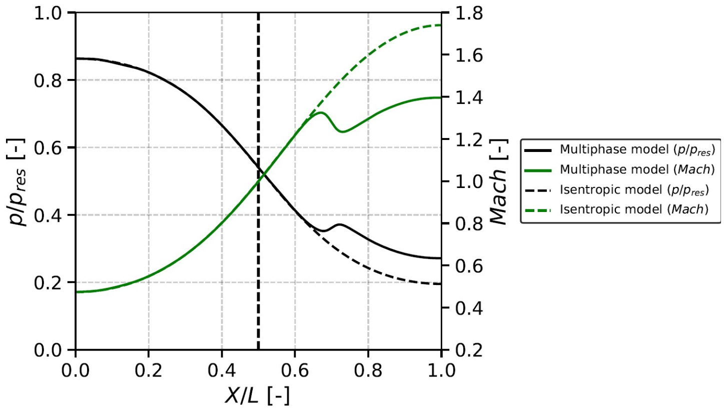

Figure 6.2: Pressure and Mach number plots for the baseline case.

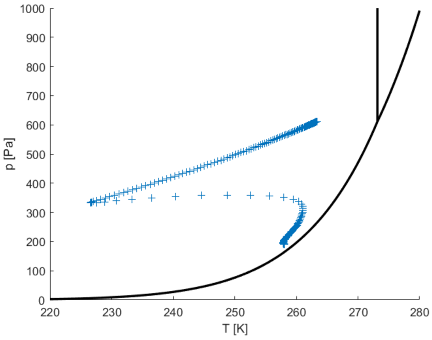

Figure 6.3: p-T diagram for uniformly distributed centreline points for the baseline simulation case.

Figure 6.2 compares pressure and Mach number for the baseline channel case illustrated in Figure 6.1, with and without (isentropic) condensation. Until the effects of nucleation are set on, the flow behaves very similarly for both situations. At about $x/L = 0.6$, as the first droplets start to form, latent heat is added to the flow and hence both pressure and temperature increase (Rayleigh flow, Greitzer et al. 2004). This in turn causes the Mach number to become less supersonic. This trends can be better understood by looking at the p-T diagram in Figure 6.3. There, the clear rupture of the metastable condition and the sudden onset of the nucleation phenomenon is visible as a vertex (Wilson point). Once equilibrium is again approached, no more solid particles are created and hence no more heat is added, with the effects of the geometric expansion now dominant (p-T curve approaches the saturation line).

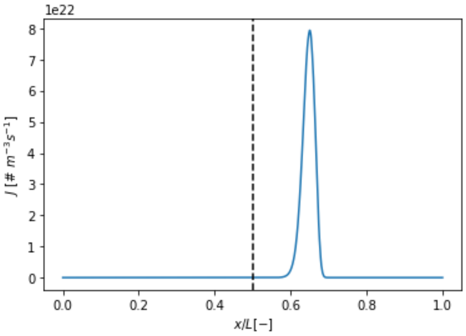

Figure 6.4: Nucleation rate along the centerline (x_c) for the baseline channel.

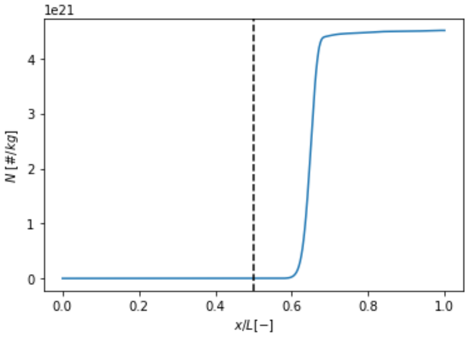

Figure 6.5: Droplet density vs. x_c for the baseline channel.

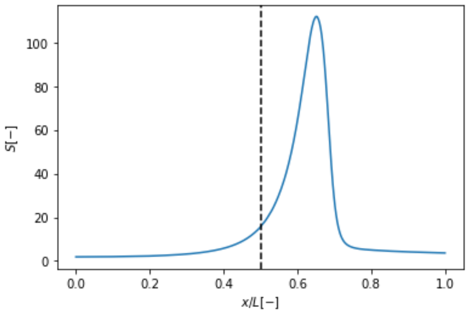

Figure 6.6: Supersaturation ratio vs. x_c for the baseline channel.

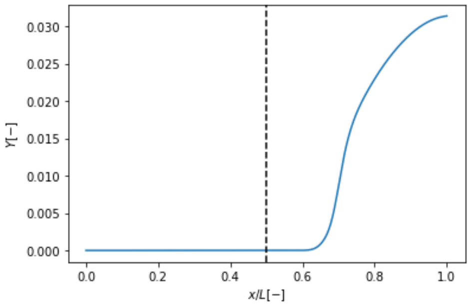

Figure 6.7: Solid fraction vs. x_c for the baseline channel.

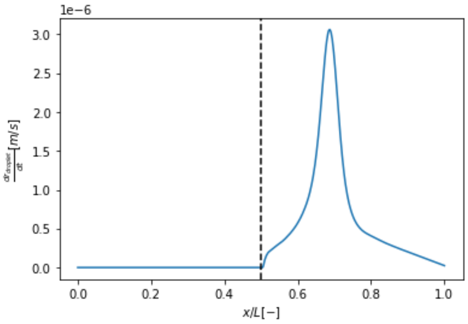

Figure 6.8: Droplet growth rate vs. x_c for the baseline channel.

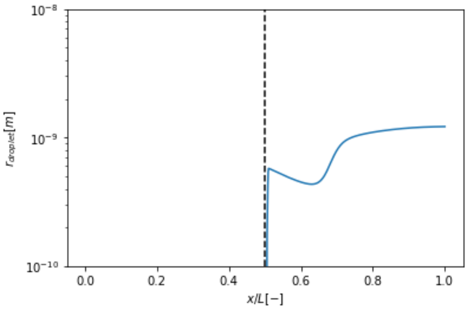

Figure 6.9: Average droplet radius vs. x_c for the baseline channel.

Figure 6.4 to Figure 6.9 show the evolution of the solid phase properties, where the vertical dashed lines represent the throat location. The effects of the onset of nucleation can be clearly noticed (i.e. it rises above around 10% of its maximum value) in Figure 6.4 at about $x/L = 0.6$, where the nucleation rate quickly rises, then to quickly drop back to 0 asymptotically. This thus makes the droplet number (Figure 6.5) quickly rise from $x/L = 0.6$ and then slowly after $x/L = 0.7$, approaching a constant value as no more particles nucleate. The supersaturation ratio (Figure 6.6) quickly rises above 1 as the flow expands from the reservoir up until the onset of nucleation, after which it drops due to the increase in pressure. This causes the solid fraction to quickly increase (Figure 6.7). As no more droplets nucleate but the supersaturation ratio is still slightly above 1, the solid fraction continues to grow, albeit at a significantly lower rate. The average particle radius (Figure 6.8, Figure 6.9) abruptly starts rising as supersaturation reaches very high values. Then, as a large number of very small particles nucleate, their average size decreases. The trend is inverted just after the supersaturation ratio peaks, as the nucleation rate abruptly drops and the droplet growth rate becomes dominant. Finally, as supersaturation drops and approaches 1 and the droplet growth rate slows down, the average droplet size stabilizes.

6.1.2. Longer channel case

In this subsection, the effects of increasing the channel length on the flow properties are investigated. The geometry of such channel is shown in Figure 6.10.

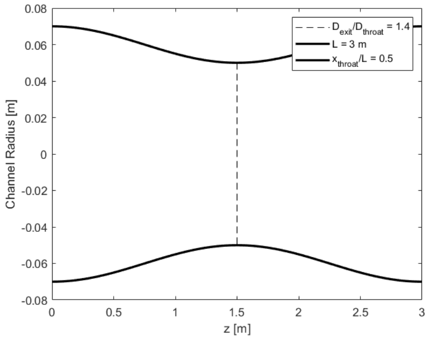

Figure 6.10: Longer channel geometry.

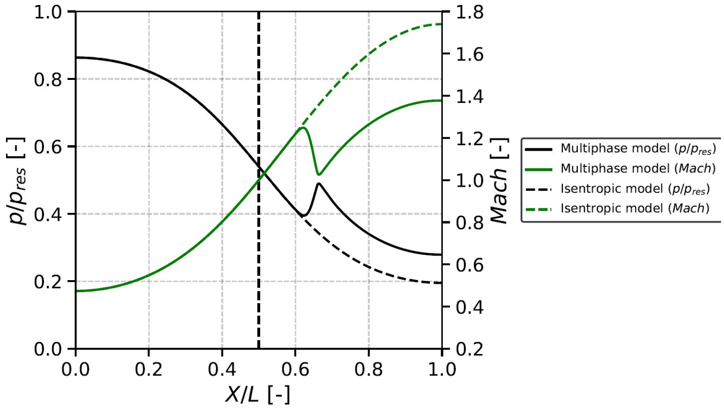

Figure 6.11: Pressure and Mach number plots for the longer channel case.

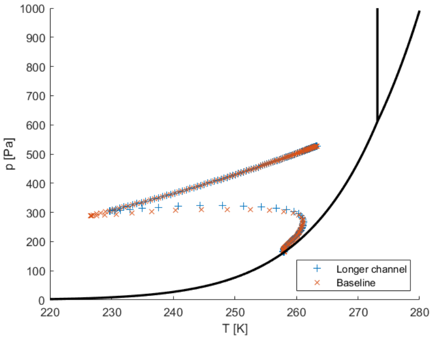

Figure 6.12: PT diagram: longer channel vs. baseline.

Figure 6.11 shows the evolution of pressure and Mach number along x_c for the extended channel (Figure 6.10) with and without (isentropic) considering the condensation phenomena. Until the effects of nucleation are set on, the flow behaves very similarly for both situations. At about $x/L = 0.6$, as the first droplets start to form, latent heat is added to the flow and hence both pressure and temperature increase. This in turn causes the Mach number to become less supersonic. Figure 6.12 shows the p-T diagram for the longer channel and the baseline one. For the longer channel, pressure and temperature go a bit less deep into the supersaturated region than for the baseline one.

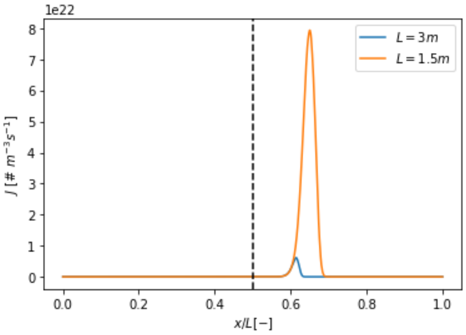

Figure 6.13: Nucleation rate vs. x_c: longer channel vs. baseline.

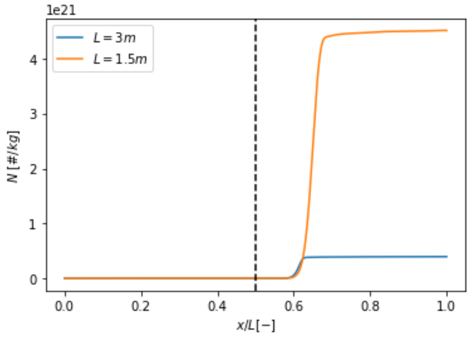

Figure 6.14: Droplet density vs. x_c: longer channel vs. baseline.

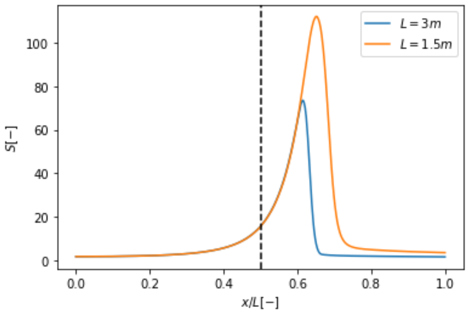

Figure 6.15: Supersaturation ratio vs. x_c: longer channel vs. baseline.

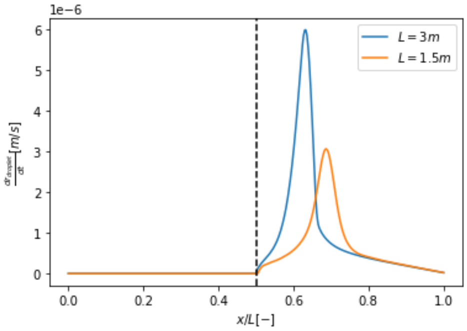

Figure 6.16: Droplet growth rate vs. x_c: longer channel vs. baseline.

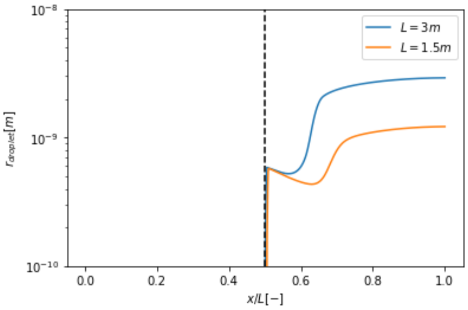

Figure 6.17: Average droplet radius vs. x_c: longer channel vs. baseline.

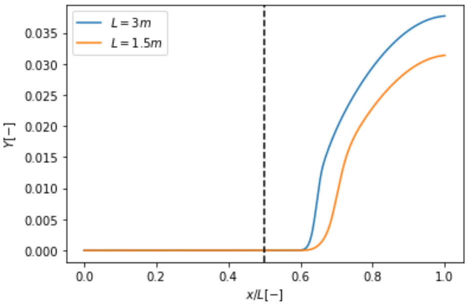

Figure 6.18: Solid fraction vs. x_c: longer channel vs. baseline.

Figure 6.13 to Figure 6.17 show the evolution of the solid phase properties for the longer channel and the baseline one. Figure 6.13 and Figure 6.14 show that nucleation starts at around $x/L = 0.6$ for both channels, but the nucleation rate and the number of particles formed are significantly higher for the baseline case. An explanation for this is that, for the same area ratio, the longer channel has a higher expansion length, i.e., the expansion is spread throughout a larger longitudinal distance and hence the core vapour will not achieve supersaturation values as high as for the baseline case (Figure 6.15). In Figure 6.16 and Figure 6.17 it can be seen that the droplet growth rate and the droplet size is higher for the longer channel. This is because the flow has a higher residence time inside the expanding region for the longer channel and hence droplets get to grow bigger. Finally, Figure 6.18 shows that the longer channel achieves a higher solid fraction value than the baseline case. Taking into consideration the competing influences of the droplet growth rate on one hand and the nucleation rate on another, this can be interpreted as the former dominating over the later.

6.1.3. Higher area ratio case

The effects of increasing the channel area ratio on the flow properties are now studied. The geometry of such channel is shown in Figure 6.19.

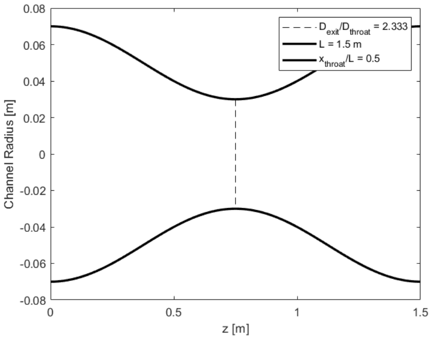

Figure 6.19: Channel geometry with a higher area ratio.

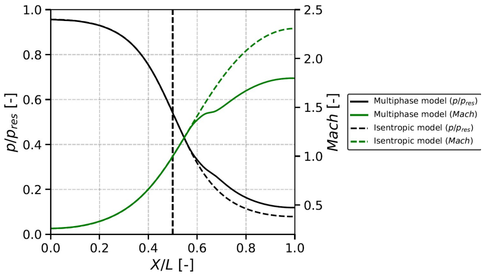

Figure 6.20: Pressure and Mach number plots: channel with a higher area ratio vs. baseline.

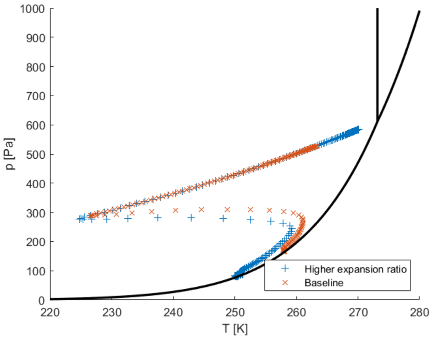

Figure 6.21: PT diagram: channel with a higher area ratio vs. baseline.

Figure 6.20 shows the evolution of pressure and Mach number along x_c for the channel with a higher area ratio (Figure 6.19) with and without (isentropic) considering the condensation phenomena. Until the effects of nucleation are set on, the flow behaves very similarly for both situations. At about $x/L = 0.55$, as the first droplets start to form, latent heat is added to the flow and hence both pressure and temperature increase. This in turn causes the Mach number to become less supersonic. Figure 6.21 shows the p-T diagram for the channel with a higher area ratio and the baseline one. For the channel with a higher area ratio, pressure and temperature go a bit deeper into the supersaturated region than for the baseline one, as expected due to the fact that the expansion is simply quicker for the former case.

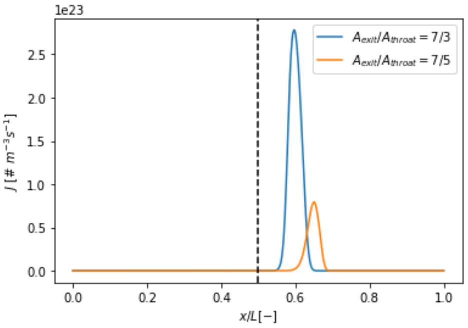

Figure 6.22: Nucleation rate vs. x_c: channel with a higher area ratio vs. baseline.

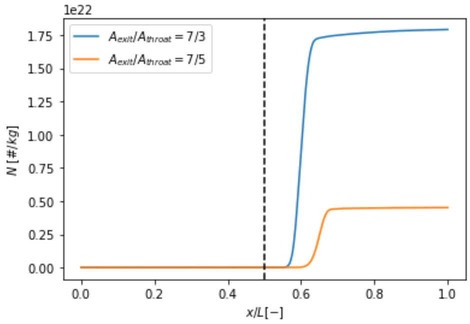

Figure 6.23: Droplet density vs. x_c: channel with a higher area ratio vs. baseline.

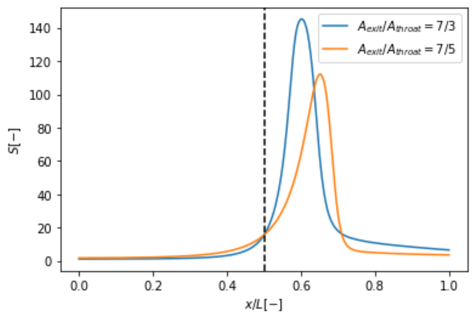

Figure 6.24: Supersaturation ratio vs. x_c: channel with a higher area ratio vs. baseline.

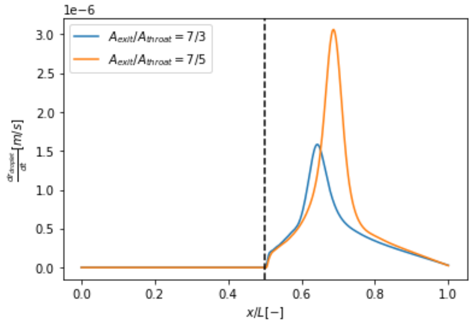

Figure 6.25: Droplet growth rate vs. x_c: channel with a higher area ratio vs. baseline.

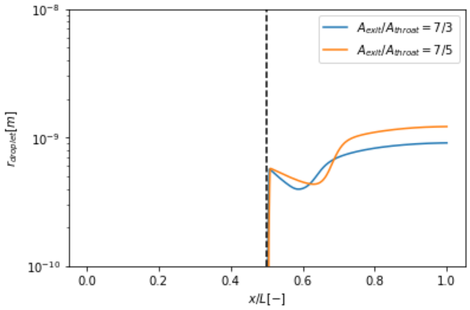

Figure 6.26: Average droplet radius vs. x_c: channel with a higher area ratio vs. baseline.

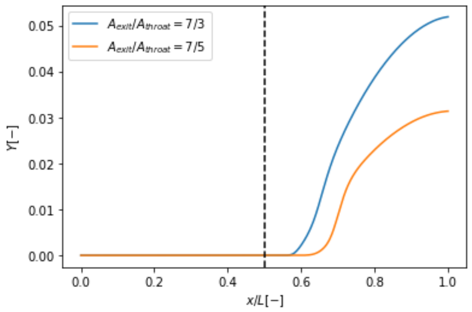

Figure 6.27: Solid fraction vs. x_c: channel with a higher area ratio vs. baseline.

Figure 6.22 to Figure 6.27 show the evolution of the solid phase properties for the channel with a higher area ratio and the baseline one. Figure 6.22 and Figure 6.23 show that nucleation starts earlier ($x/L = 0.55$ vs. $x/L = 0.6$) for the channel with higher area ratio, with the nucleation rate and the number of particles formed significantly higher for that case, albeit with a slight offset. This can be attributed to the higher maximum supersaturation value attained for the channel geometry with a higher area ratio (Figure 6.24). In Figure 6.25 and Figure 6.26 it can be seen that the droplet growth rate and the droplet size is higher for the baseline channel. This is because the flow has a higher residence time inside the expanding region for the baseline channel (lower velocity) and hence droplets get to grow bigger. Finally, Figure 6.27 shows that the channel with a higher area ratio achieves a higher solid fraction value than the baseline case. Taking into consideration the competing influences of the droplet growth rate on one hand and the nucleation rate on another, this can be interpreted as the later dominating over the former.

6.1.4. Different throat location case

The effects of changing the channel throat location on the flow properties are here assessed. For that purpose, two different cases for the throat location ($x_{throat}/L = 0.25, 0.75$) are simulated and compared against the baseline case ($x_{throat}/L = 0.5$). The geometry of such channels are shown in Figure 6.28 and Figure 6.30.

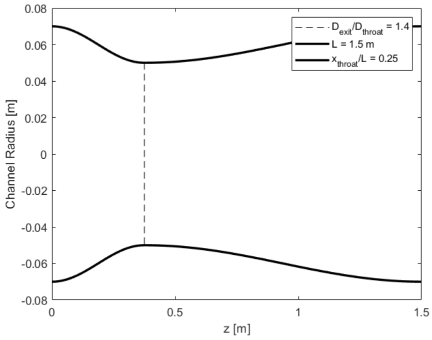

Figure 6.28: Channel geometry with a throat located at $x_{throat}/L = 0.25$.

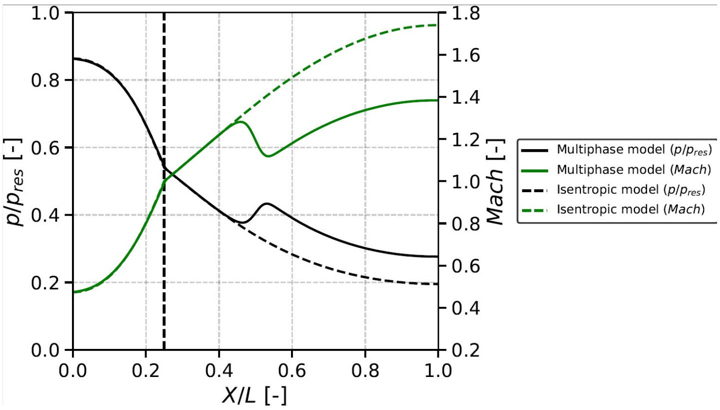

Figure 6.29: Pressure and Mach number plots: channel with a throat located at $x_{throat}/L = 0.25$ vs. baseline.

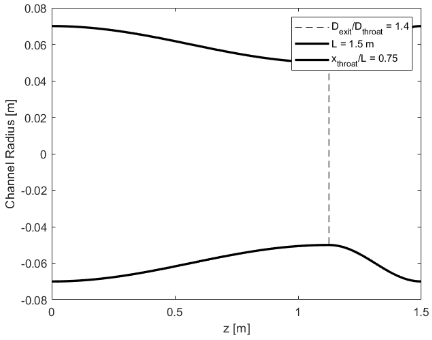

Figure 6.30: Channel geometry with a throat located at $x_{throat}/L = 0.75$.

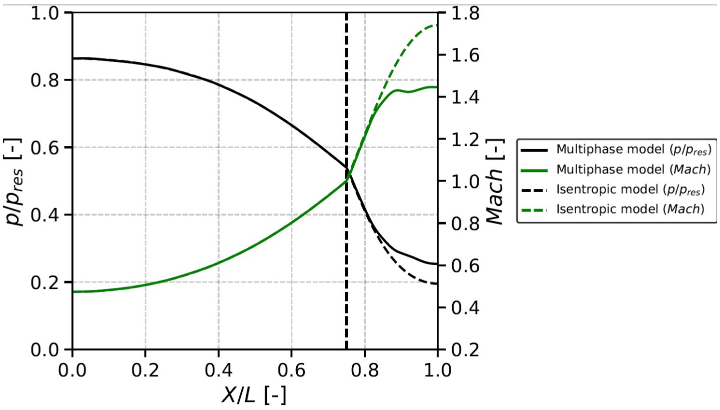

Figure 6.31: Pressure and Mach number plots: channel with a throat located at $x_{throat}/L = 0.75$ vs. baseline.

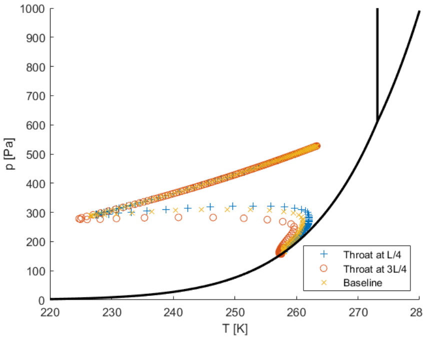

Figure 6.32: PT diagram: channels with different throat locations.

Figure 6.29 and Figure 6.31 show the evolution of pressure and Mach number along x_c for the channels with throat located at $x_{throat}/L = 0.25, 0.75$ with and without (isentropic) considering the condensation phenomena. The closer the throat is located to the reservoir, the farther upstream the Wilson point is located in the channel. Figure 6.32 shows that the further downstream the throat location is, the deeper pressure and temperature go into the supersaturated region, as expected due to the fact that gradients are more pronounced for those cases.

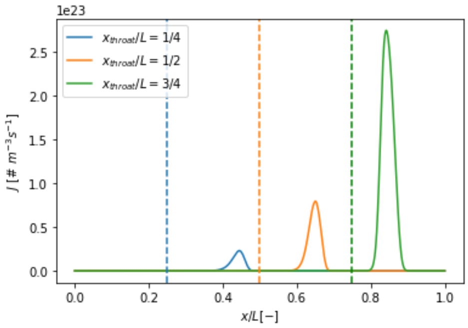

Figure 6.33: Nucleation rate vs. x_c: channels with different throat locations.

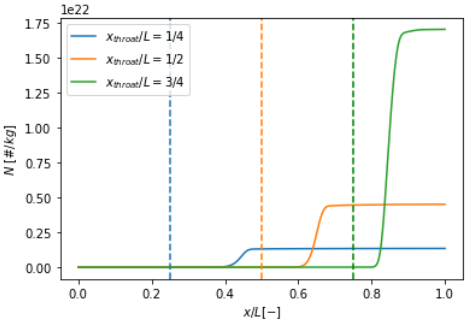

Figure 6.34: Droplet density vs. x_c: channels with different throat locations.

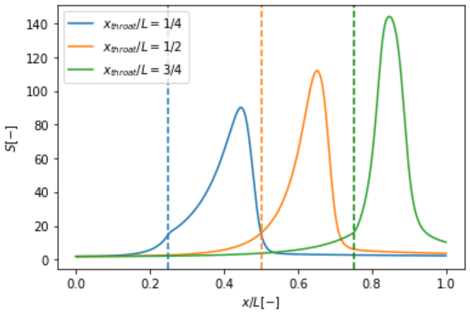

Figure 6.35: Supersaturation ratio vs. x_c: channels with different throat locations.

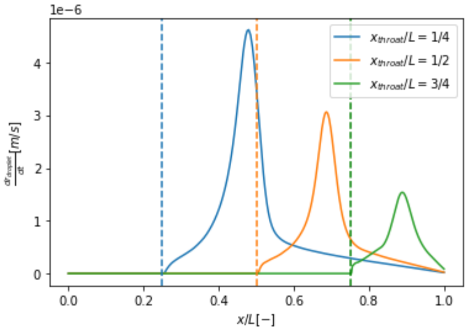

Figure 6.36: Droplet growth rate vs. x_c: channels with different throat locations.

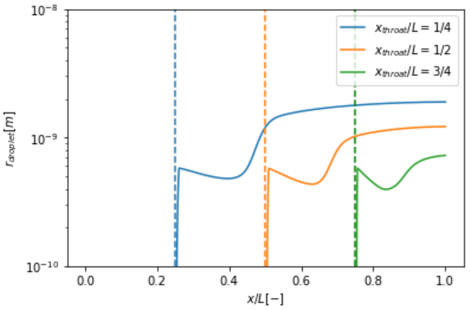

Figure 6.37: Average droplet radius vs. x_c: channels with different throat locations.

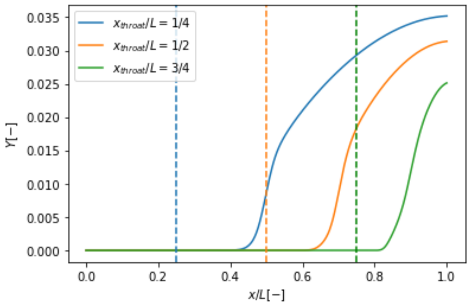

Figure 6.38: Solid fraction vs. x_c: channels with different throat locations.

Figure 6.33 to Figure 6.38 show the evolution of the solid phase properties for the channels with throat located at $x_{throat}/L = 0.25, 0.5, 0.75$. Figure 6.33 and Figure 6.34 show that the onset of nucleation is related to the throat location, happening first for the case $x_{throat}/L = 0.25$ and last for $x_{throat}/L = 0.75$, as that is where the pressure gradient is steeper and hence supersaturation achieves its maximum value (Figure 6.35). However, both the nucleation rate and the droplet number reach higher maximum values for the case $x_{throat}/L = 0.75$, due to the presence of higher gradients of properties for this geometry. This can be attributed to the higher maximum supersaturation value attained for the case $x_{throat}/L = 0.75$. In Figure 6.36 and Figure 6.37 it can be seen that the droplet growth rate and the droplet size achieve higher values for the case $x_{throat}/L = 0.25$. This is because the residence time is higher for this case, as the length of the divergent section is higher for this channel. Finally, Figure 6.38 shows that the solid fraction attains higher values for the case $x_{throat}/L = 0.25$. This is because the droplet growth rate influence dominates over that of the nucleation rate.

6.2. Effects of the boundary conditions

6.2.1. Wall friction and heat convection effects

In this subsection, the effects of considering the viscous effects of wall friction and heat convection on the flow are investigated. For that, the turbulence model mentioned in chapter 4 is used in the simulation of the baseline channel geometry. The results are shown and analysed below.

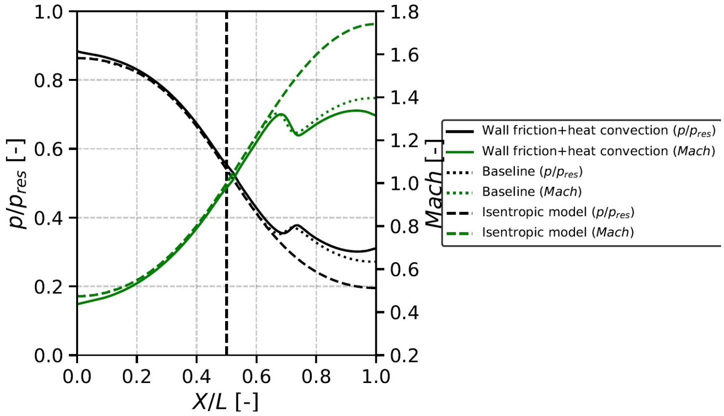

Figure 6.39: Pressure and Mach number plots: case with wall friction and heat convection.

It can be observed that the effects of wall friction and heat convection have a relatively small effect in the flow properties overall. However, there are some key differences between this and the baseline case that can be underlined. Figure 6.39 clearly shows that wall friction and heat convection lead to a decrease in the exit Mach number and increase in the exit pressure. This can be interpreted as a decrease in the effective cross section area, due to the presence of a boundary layer.

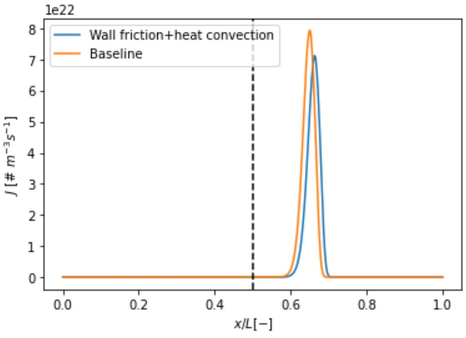

Figure 6.40: Nucleation rate vs. x_c: case with wall friction and heat convection vs. baseline.

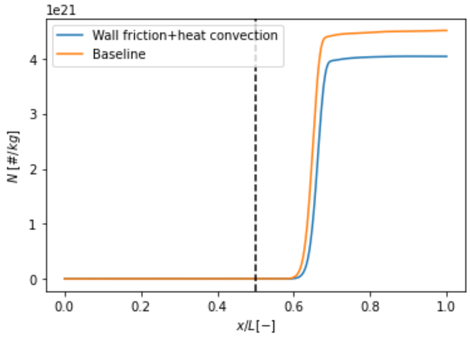

Figure 6.41: Droplet density vs. x_c: case with wall friction and heat convection vs. baseline.

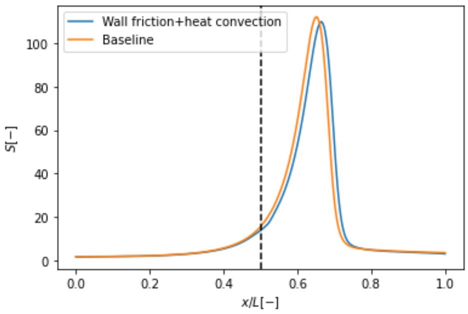

Figure 6.42: Supersaturation ratio vs. x_c: case with wall friction and heat convection vs. baseline.

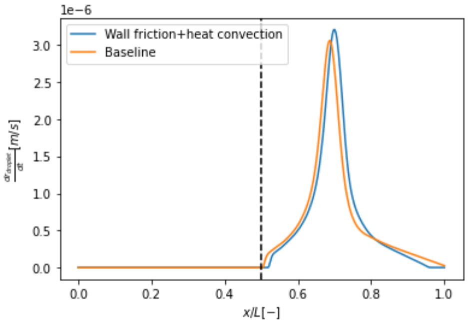

Figure 6.43: Droplet growth rate vs. x_c: case with wall friction and heat convection vs. baseline.

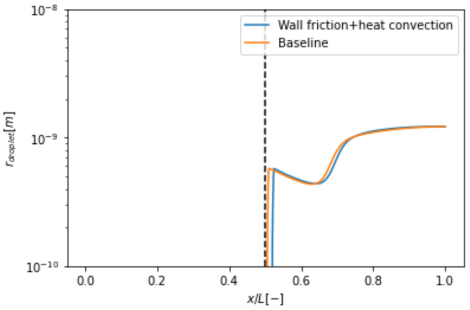

Figure 6.44: Average droplet radius vs. x_c: case with wall friction and heat convection vs. baseline.

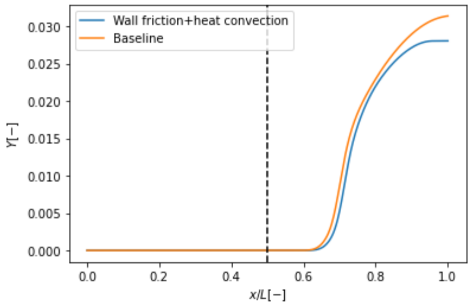

Figure 6.45: Solid fraction vs. x_c: case with wall friction and heat convection vs. baseline.

Figure 6.40 and Figure 6.41 in turn show that the onset of nucleation happens slightly downstream for the model including wall friction and heat convection, with the nucleation rate and droplet number achieving slightly lower maxima for the later case. This is also a consequence of the presence of a boundary layer, which makes the property gradients in the throat region smoother. Figure 6.42, Figure 6.43 and Figure 6.44 on the other hand show little differences between the models with and without wall friction and heat convection. This is because supersaturation and particle growth are mainly inviscid phenomena. Finally, Figure 6.45 shows that the solid fraction attains lower values for the model accounting for wall friction and heat convection, as a consequence of the nucleation rate effect being largely dominant over that of the droplet growth rate, which is very similar for both cases.

6.2.2. Different reservoir temperature case

Here the effects of varying the reservoir temperature are analysed. In order to do that, the baseline channel geometry (Figure 3.11) is simulated with three different reservoir temperature values ($T_{res} = 273.16K, 278.16K, 283.16K$).

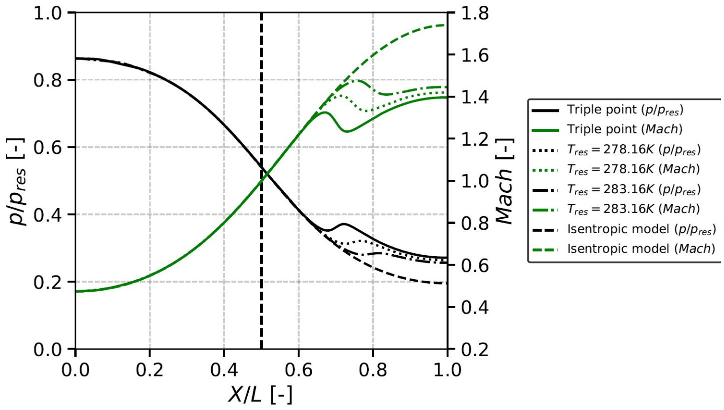

Figure 6.46: Pressure and Mach number plots: cases with different reservoir temperatures.

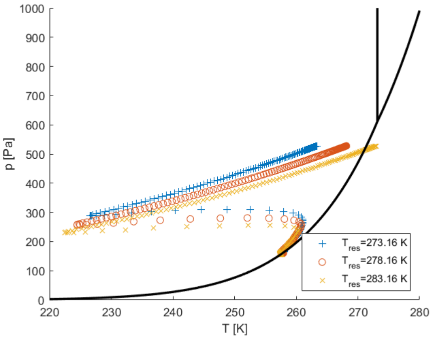

Figure 6.47: PT diagram: cases with different reservoir temperatures.

Based on the type of analysis that was done for the effects of changing geometric features on the flow behaviour, similar trends can be drawn upon when looking into the effects of varying the reservoir temperature. Figure 6.46 shows the evolution of pressure and Mach number along x_c for channels with $T_{res} = 273.16K, 278.16K, 283.16K$ with and without (isentropic) considering the condensation phenomena. The lowest the reservoir temperature, the farthest upstream the Wilson point is located in the channel. Figure 6.47 shows that the higher the reservoir temperature, the deeper pressure and temperature go into the supersaturated region. This is to be expected, as for those cases there is initially a lower likelihood for droplets to nucleate.

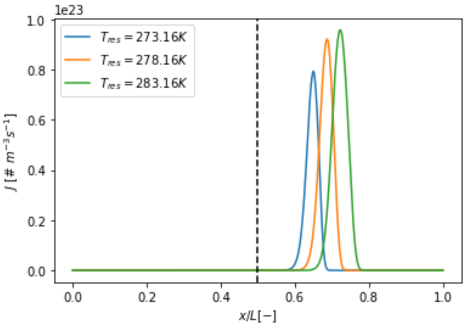

Figure 6.48: Nucleation rate vs. x_c: cases with different reservoir temperatures.

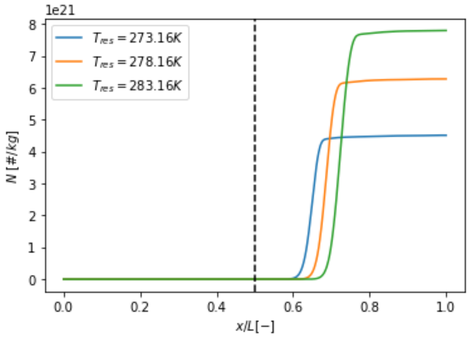

Figure 6.49: Droplet density vs. x_c: cases with different reservoir temperatures.

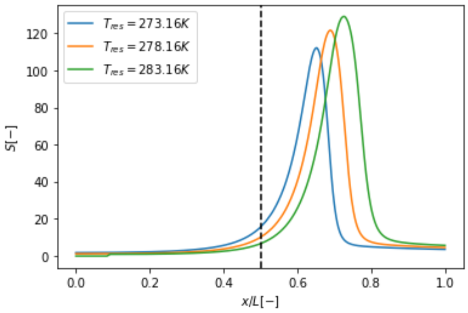

Figure 6.50: Supersaturation ratio vs. x_c: cases with different reservoir temperatures.

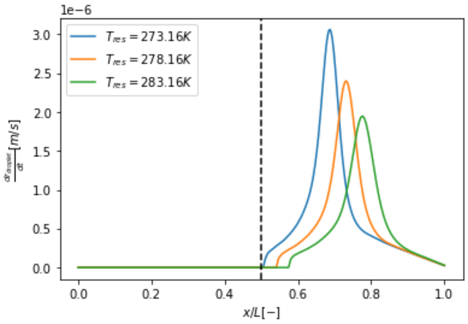

Figure 6.51: Droplet growth rate vs. x_c: cases with different reservoir temperatures.

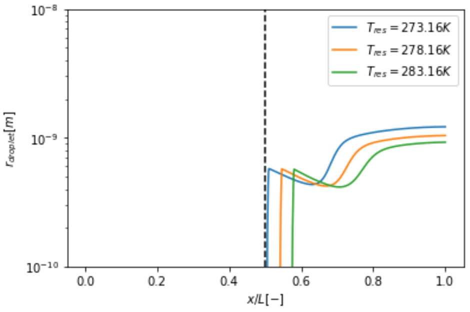

Figure 6.52: Average droplet radius vs. x_c: cases with different reservoir temperatures.

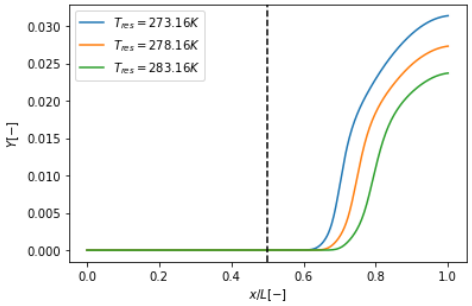

Figure 6.53: Solid fraction vs. x_c: cases with different reservoir temperatures.

Figure 6.48 and Figure 6.49 show that nucleation starts earlier for the channel with the lowest reservoir temperature. This can be explained by the fact that for this case steam is already well into supersaturation state inside the reservoir. However, as the case with higher reservoir temperature achieves lower minimum temperature and pressure, nucleation rate and particle number attain higher overall values for this case. This can be attributed to the higher maximum supersaturation value attained for that case (Figure 6.50). On the other hand, the maximum supersaturation value is achieved first for the case with the lowest reservoir temperature. In Figure 6.51 and Figure 6.52 it can be seen that the droplet growth rate and the droplet size achieve higher values for the case with the lowest reservoir temperature. This is because the residence time is higher for this case, due to the lower achieved velocity. Finally, Figure 6.53 shows that the solid fraction attains higher values for the case with the lowest reservoir temperature, as the droplet growth rate term is dominant over that of the nucleation rate.

6.2.3. Different reservoir pressure case

An assessment of the effects of varying the reservoir pressure is done now. In order to do that, the baseline channel geometry (Figure 3.11) is simulated with three different reservoir pressure values ($p_{res} = 411.2Pa, 611.2Pa, 811.2Pa$).

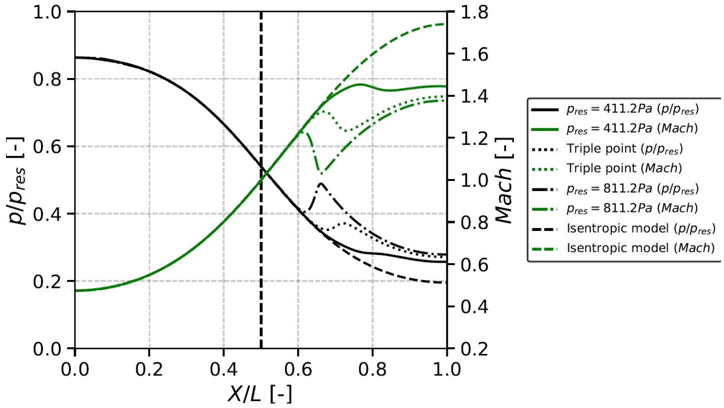

Figure 6.54: Pressure and Mach number plots: cases with different reservoir pressures.

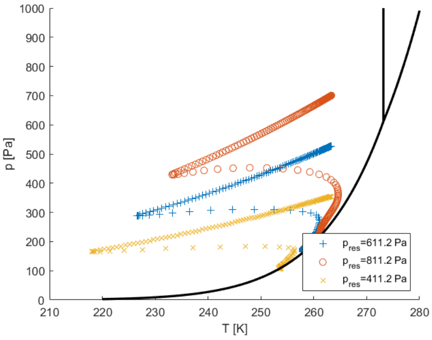

Figure 6.55: PT diagram: cases with different reservoir pressures.

Figure 6.54 shows the evolution of pressure and Mach number along x_c for channels with $p_{res} = 411.2Pa, 611.2Pa, 811.2Pa$ with and without (isentropic) considering the condensation phenomena. The highest the reservoir temperature, the farthest upstream the Wilson point is located in the channel. Figure 6.55 shows that the lower the reservoir pressure, the deeper pressure and temperature go into the supersaturated region. This is to be expected, as for those cases there is initially a lower likelihood for droplets to nucleate.

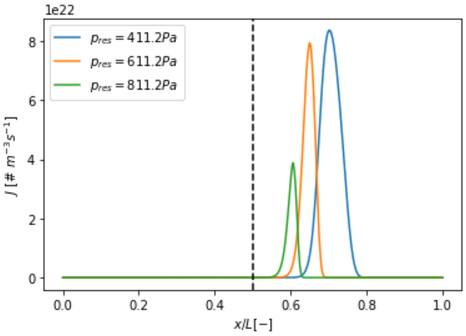

Figure 6.56: Nucleation rate vs. x_c: cases with different reservoir pressures.

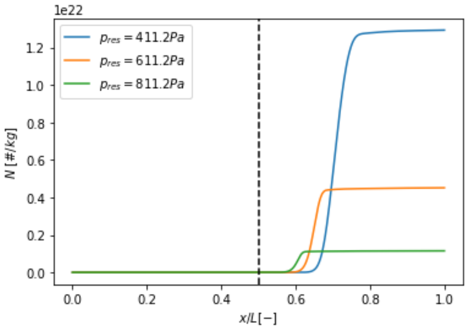

Figure 6.57: Droplet density vs. x_c: cases with different reservoir pressures.

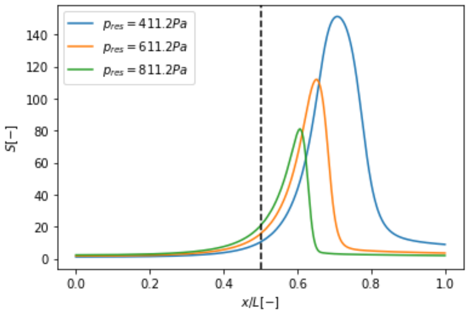

Figure 6.58: Supersaturation ratio vs. x_c: cases with different reservoir pressures.

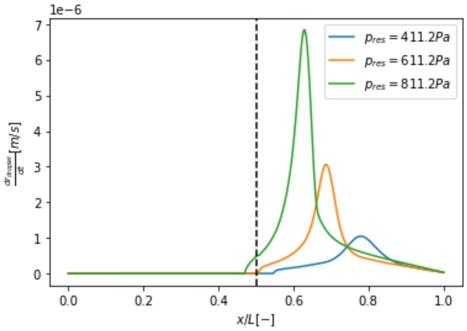

Figure 6.59: Droplet growth rate vs. x_c: cases with different reservoir pressures.

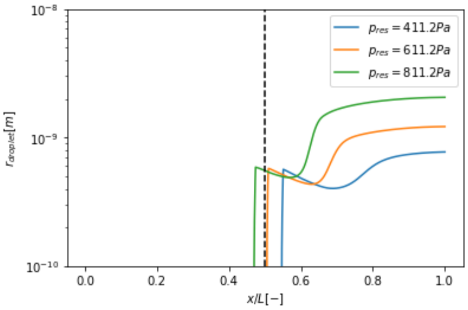

Figure 6.60: Average droplet radius vs. x_c: cases with different reservoir pressures.

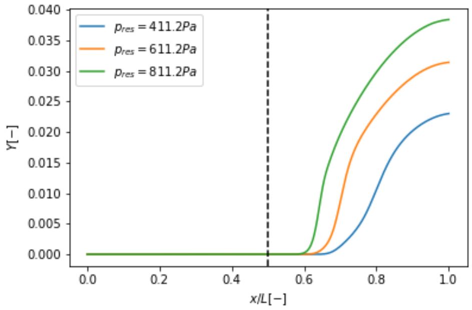

Figure 6.61: Solid fraction vs. x_c: cases with different reservoir pressures.

Figure 6.56 and Figure 6.57 show that nucleation starts earlier for the channel with the highest reservoir pressure. This can be explained by the fact that for this case steam is already well into supersaturation state inside the reservoir. However, as the case with lower reservoir pressure achieves lower minimum temperature and pressure, nucleation rate and particle number attain higher overall values for this case. This can be attributed to the higher maximum supersaturation value attained for that case (Figure 6.58). On the other hand, the maximum supersaturation value is achieved first for the case with the highest reservoir pressure. In Figure 6.59 and Figure 6.60 it can be seen that the droplet growth rate and the droplet size achieve higher values for the case with the highest reservoir pressure. This is because the residence time is higher for this case, due to the lower achieved velocity. Finally, Figure 6.61 shows that the solid fraction attains higher values for the case with the highest reservoir pressure, as the droplet growth rate term is dominant over that of the nucleation rate.

6.3. Application: Enceladus plumes

In this subsection, a similarity study is performed with the goal to achieve a unifying outlook for the onset of the condensation phenomenon at the laboratory and Enceladus scales. For that purpose, a comparison of the property evolution for channels with $L = 1.5m, 150m$ is first performed. Figure 6.62 shows the evolution of pressure and Mach number for channels with $L = 1.5m, 150m$. Clearly, for the case with $L = 150m$ the onset of condensation happens at a farther upstream relative distance x_c/L and at a higher temperature. This can better be understood by looking at Figure 6.63, which further corroborates that the steam goes less into the supersaturated region for longer channels, that can be analysed through the lens of the Wilson number. Namely, the longest the channel, the longest the activation time and hence the lowest the cooling rate and Wilson number. In the limit of a very high channel length, the nucleation phenomenon occurs almost entirely in equilibrium. Figure 6.64 to Figure 6.68 show the evolution of the flow properties for channels with $L = 1.5m, 150m$. These results follow the same trends as those obtained when comparing the channel cases $L = 1.5m, 3m$, with the difference that the length scales being dealt with in this section differ by 2 orders of magnitude.

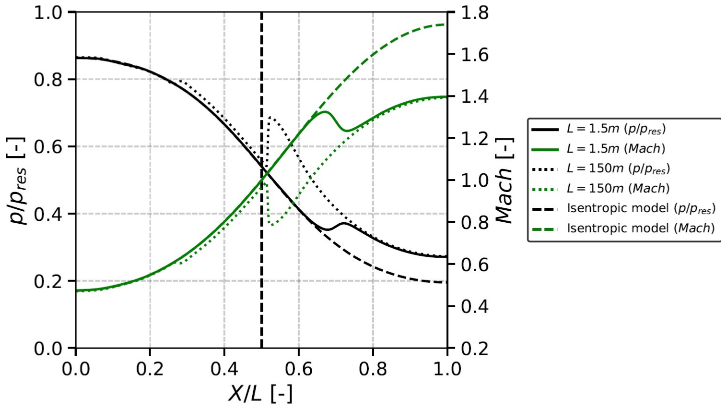

Figure 6.62: Pressure and Mach number plots: $L = 1.5m, 150m$.

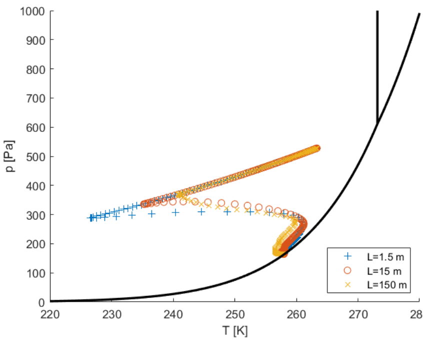

Figure 6.63: PT diagram: $L = 1.5m, 15m, 150m$.

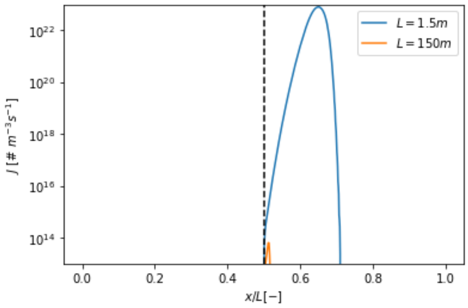

Figure 6.64: Nucleation rate vs. x_c: $L = 1.5m, 150m$.

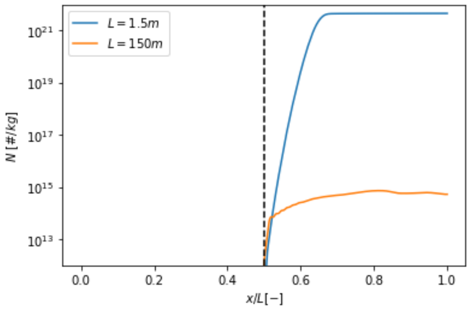

Figure 6.65: Droplet density vs. x_c: $L = 1.5m, 150m$.

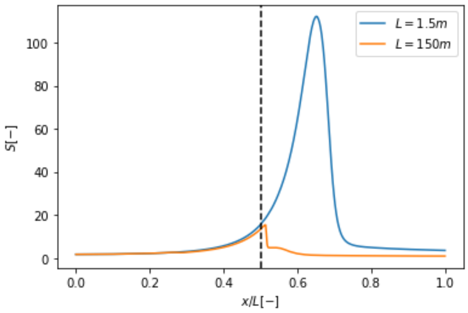

Figure 6.66: Supersaturation ratio vs. x_c: $L = 1.5m, 150m$.

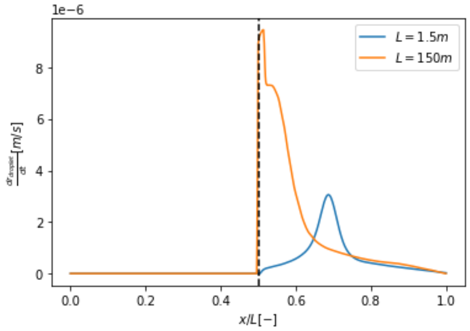

Figure 6.67: Droplet growth rate vs. x_c: $L = 1.5m, 150m$.

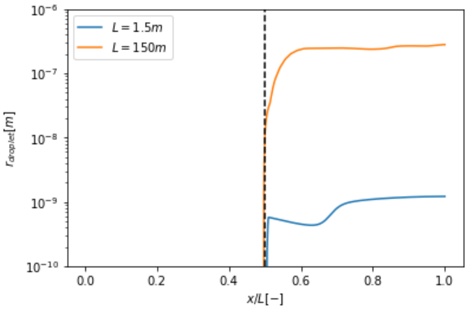

Figure 6.68: Average droplet radius vs. x_c: $L = 1.5m, 150m$.

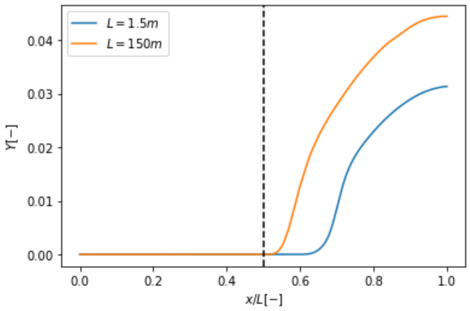

Figure 6.69: Solid fraction vs. x_c: $L = 1.5m, 150m$.

Finally, it is also particularly interesting to plot the velocity profile throughout the centreline (Figure 6.76) and the droplet size distribution at the outlet (Figure 6.71) for the channel with length $L = 150m$, comparing it with data from Schmidt et al. 2008 for channels with similar length scales. The flow velocity follows a similar pattern to the Mach number, increasing throughout the channel as the vapour expands and decreasing in the nucleation regions due to the latent heat. Velocity achieves a value of 553 m/s at the vent, which is well within the range of 350-950 m/s estimated by fitting the UVIS and INMS data (Dong et al. 2011, Schmidt et al. 2008). As for the droplet size distribution, it can clearly be seen that most ice droplets have sizes at the vent ranging between 0.1 μm (10^{-7} m) and 1 μm ($10^{-6} m$), which is compatible with what was predicted by Hedman et al. 2009 and Schmidt et al. 2008 for channels with lengths in the order of hundreds of meters.

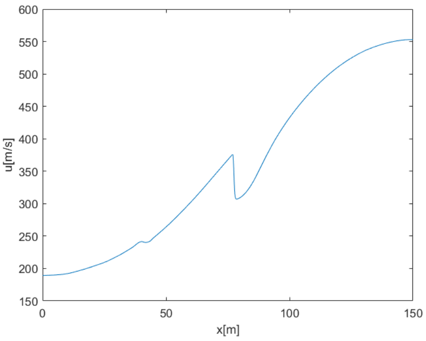

Figure 6.70: Velocity profile vs. x_c: channel with length $L = 150m$.

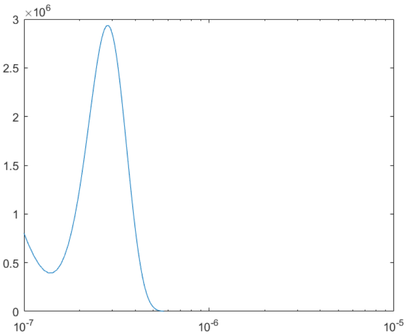

Figure 6.71: Droplet size distribution at the vent: channel with length $L = 150m$.

Then, the droplet size values at the vent are plotted against the expansion parameter ϵ in Figure 6.72. A power-law regression of the type $y = ax^b$ is used to perform a parametric analysis. This process is replicated for three different reservoir conditions settings: triple point, $T_{res} = 278.16K$, $p_{res} = 611.2Pa$ and $p_{res} = 811.2Pa$, $T_{res} = 273.16K$.

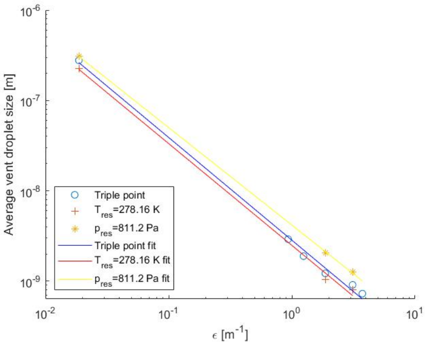

Figure 6.72: $r_{droplet}$ vs. ϵ for the geometric settings (left to right): $L = 150m$, $L = 3m$, $x_{throat}/L = 0.25$, baseline, $D_{exit}/D_{throat} = 7/3$, $x_{throat}/L = 0.75$.

From the previous figure, it can be seen that the average vent droplet size is strongly correlated to the channel expansion ratio ϵ. Particularly, for the triple point case the following fitting parameters were obtained: $a = 3 \cdot 10^{-9}$, $b = -1.137$, $R^2 = 0.9999$. The larger the expansion ratio, the lower the particle radius. Regarding the influence of the reservoir conditions, increasing the reservoir temperature is equivalent to a downwards offset of the $r_{droplet}$ vs. ϵ curve, whereas increasing the reservoir pressure has a the opposite effect, i.e., an upwards offset of the $r_{droplet}$ vs. ϵ curve. Specifically for the channel with $L = 150m$, a solid fraction of 0.04448 and an average droplet size of 0.2782 μm were obtained at the vent.

6.4. Comparison between 2D and quasi-1D models

The model chosen and used throughout this work is based on a 2D description of the flow. In the previous sections of this chapter, the analysis was based on channel centreline values such that the different cases could be more readily compared. In order to assess whether these values are representative of the flow, Figure 6.73 to Figure 6.76 show pressure, temperature, density and velocity contour plots for the channel with length $L = 150m$. Further, Figure 6.77 compares pressure and Mach number values at two different y-locations of the same channel and also with the same property values obtained using the quasi-1D model described by Hijden 2021.

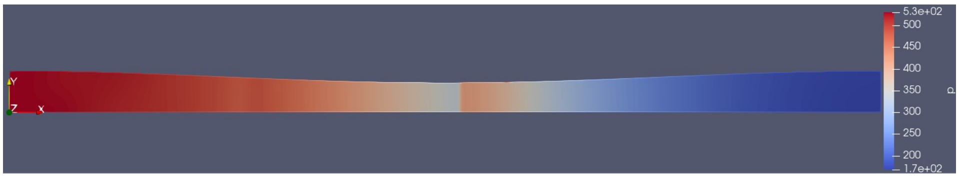

Figure 6.73: Contour of the static pressure field (SI values) for the channel with $L = 150m$.

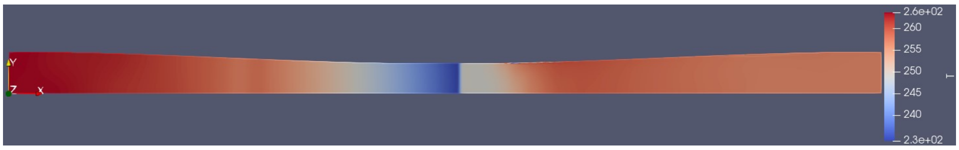

Figure 6.74: Contour of the static temperature field (SI values) for the channel with $L = 150m$.

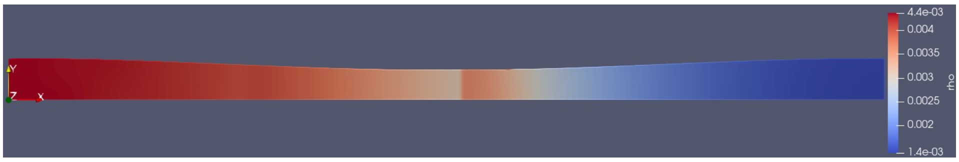

Figure 6.75: Contour of the density field (SI values) for the channel with $L = 150m$.

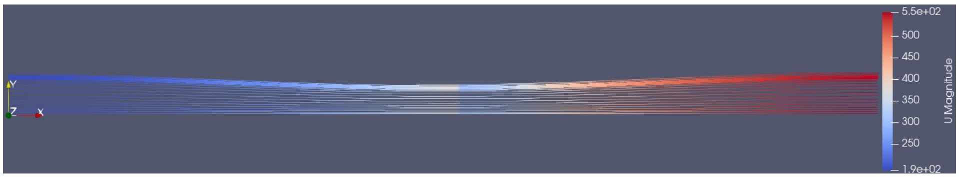

Figure 6.76: Shape of the velocity streamlines (SI values) for the channel with $L = 150m$.

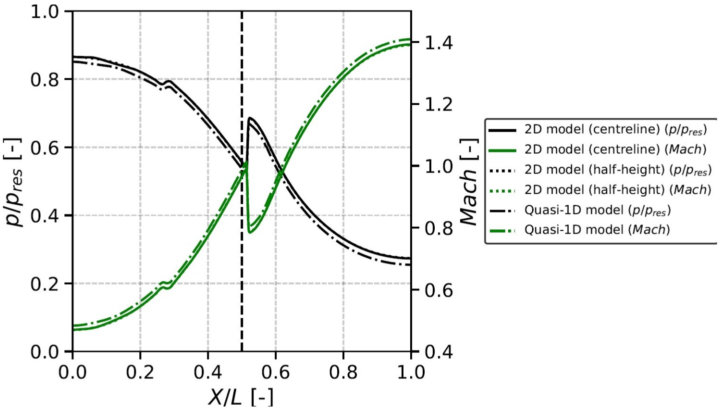

Figure 6.77: Comparison between 2D and quasi-1D model by Hijden 2021.

The previous figures show that the 2D effects are small and thus the quasi-1D approximation can be used to study these plume phenomena. Namely the flow properties are indistinguishable at the channel centreline and half height. On the other hand, there are small differences between the results given by the 2D model and those given by the quasi-1D model by Hijden 2021. The later shows a slightly lower pressure ratio and a slightly higher Mach number. This difference is more noticeable at the channel exit, where streamlines diverge the most.

6.5. Comparison with laboratory experimental data

In this section, a comparison is performed between results from numerical simulations and experimental results obtained by Verhoeff 2023 in the Aerodynamics laboratory at TU Delft. Figure 6.78 and Figure 6.79 show such comparisons. Two different simulation settings for the wall temperature were used to make such comparison: adiabatic and isothermal. Mach number and pressure ratio were also compared to an isentropic simulation case.

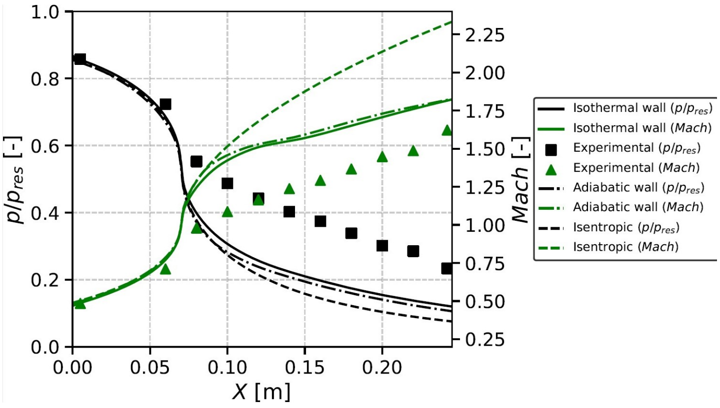

Figure 6.78: Mach number and pressure ratio: simulations vs laboratory experimental results from model 1 by Verhoeff 2023 (full power setting).

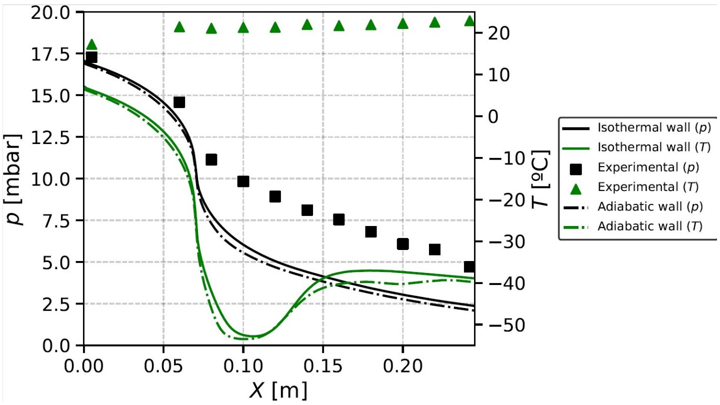

Figure 6.79: Temperature and pressure: simulations vs laboratory experimental results from model 1 by Verhoeff 2023 (full power setting).

As expected, for the simulation case with the isothermal wall the increase (decrease) in pressure and temperature (Mach number) resulting from the condensation process is slightly more pronounced than for the adiabatic case, as there is heat transfer from the walls to the flow in the former case. As for the comparison between the simulations and experimental results, clear differences can be seen. For instance, according to the simulations the flow cools down to temperatures lower than -50 $°C$, then increasing only slightly to a bit higher than -40 $°C$. This is in total contrast to what happens in the experiment, where temperature starts rising from the reservoir to a plateau of around 22 $°C$. Experimental Mach number and pressure also significantly diverge from simulation expectations from around $x = 0.05m$ on. Namely, in the experiment the sonic point is achieved at around $x = 0.08m$ vs. $x = 0.07m$ in the simulations. One consideration is that the 'experimental' Mach number was in fact calculated from actually measured pressure using isentropic relations. Of course, this is highly dubious once condensation starts. Another important remark is that the experimental measurements were taken close to the wall (so subject to boundary layer effects), whereas the simulation results are plotted along the channel centreline. Nevertheless, such extreme property radial gradients are still questionable. The pressure difference between the reservoir and the vent, much higher for the simulations than for the experiment (vent pressure of about 2.5 $mbar$ for the simulations vs. 4.7 $mbar$ for the experiment) could possibly be explained by the presence of nucleated grains already at the reservoir in the experiments, as argued by Ingersoll and Nakajima 2016b, as vapour is already supersaturated there.

6.6. Discussion

In order to acquire an overview on the effects that the different channel geometric and boundary conditions settings have on the plumes, the values of key flow properties at the vent such as Mach number, pressure ratio, channel Knudsen number, number of particles, solid fraction and droplet size are summarized in Table 6.1.

n	Test case	$M[-]$	$p/p_0[-]$	$Kn[-]$	$N[10^{21}/kg]$	$f[-]$	$r_{droplet}[nm]$
1	Isentropic model	1.740	0.1951	-	-	-	-
2	Multi-phase model ($\epsilon = 1.867$)	1.396	0.2714	0.00013	4.516	0.03138	1.217
3	Longer channel ($\epsilon = 0.933$)	1.377	0.2790	0.00013	0.3962	0.03771	2.912
4	Higher area ratio ($\epsilon = 3.111$)	1.798	0.1190	0.00026	17.93	0.05192	0.9090
5	$x_{throat}/L = 0.25$ ($\epsilon = 1.244$)	1.383	0.2765	0.00013	1.350	0.03519	1.891
5	$x_{throat}/L = 0.75$ ($\epsilon = 3.733$)	1.444	0.2544	0.00012	17.07	0.02514	0.7257
6	Wall friction and heat convection	1.314	0.3106	0.00012	4.045	0.02805	1.216
7	$T_{res} = 278.15K$	1.419	0.2640	0.00013	6.284	0.02731	1.041
7	$T_{res} = 283.15K$	1.445	0.2565	0.00013	7.805	0.02370	0.9236
8	$p_{res} = 811.2Pa$	1.376	0.2788	0.00010	1.150	0.03838	2.054
8	$p_{res} = 411.2Pa$	1.444	0.2570	0.00018	12.94	0.02301	0.7729
-	$L = 150m$ ($\epsilon = 0.01867$)	1.392	0.2733	0.013	$5.359{\cdot}10^{-7}$	0.04448	278.2

Table 6.1: Key plume property values at the vent

Now, a critical reflection on the results previously obtained is made, if possible based on comparisons between the values of simulated key plume properties with data from the Cassini mission and Schmidt et al. 2008. The results shown in the previous section clearly lead to the conclusion that the geometric expansion ratio has a fundamental influence on the Mach number and pressure ratio at the vent. Namely, the higher the cross section ratio between vent and throat, the higher the exit Mach number and the lower the pressure ratio. Particularly, the Mach number values for the channel with $L = 150m$ and expansion ratio of 1.4 (1.392) are in agreement with the values reported by Schmidt et al. 2008 for velocity and temperature. Higher reservoir temperature or lower reservoir pressure also lead to an increase the Mach number and decrease in the pressure ratio. The channel Knudsen number is only an important parameter for the channel with $L = 150m$, for which it achieves a value of 0.013 at the vent. According to Tsien 1946, this is clearly in the slip-flow regime. As such, future works should consider a slipping wall model for this case. The number of particles fundamentally depends on the geometric expansion ratio. This is of course because the nucleation rate is higher in these situations. As for the solid fraction, a higher expansion ratio, higher divergent length or higher reservoir pressure all lead to higher values of this property at the vent. In order to achieve a solid fraction in the range 0.07-0.2, in line with what is measured for Enceladus (Gao et al. 2016, Kieffer et al. 2009), while maintaining particle sizes in the range 0.1-3 μm (Hedman et al. 2009), channel lengths in the range 100-1000 m with an expansion ratio of around 1.4 and a reservoir temperature of about 273.16 K (to achieve vent velocities of about 550 m/s) are suitable. It is also important to keep in mind that, even though in reality the velocity of the solid grains is smaller than that of the gas (2/3 of that of the vapour phase for the majority of the grains according to Schmidt et al. 2008, due to wall collisions followed by re-acceleration by the gas), for the solid fraction values of interest (0.07-0.2) this difference does not play a significant role in the plume dynamics. Nevertheless, future works can study this difference, possibly also coupled with a suitable model for the wall interactions.

7

Conclusion & recommendations

In this project, an investigation of the fundamental physical processes behind the ice and vapour plumes of Enceladus was elaborated. These plumes are believed to extend from subsurface reservoirs of liquid water (fed by oceans) through very long and narrow cracks all the way to the surface of the moon. First, a study of the physical phenomena behind the formation and maintenance of such plumes was elaborated. Then, the influences of the crevasse shape and reservoir conditions were studied. Finally, general trends were established between the plume properties and the characteristics of the channel and reservoir, with a similarity analysis between the laboratory and Enceladus scales elaborated upon this. Some questions arose with the proposal of the project topics, while others did so throughout the process of making it. All of them are given an answer here. Then, for cases in which a definite answer is not possible, recommendations for future investigations are suggested, including some of the author's own remarks from the elaboration of this project.

Q1: Which physical processes should be included to model the plumes of Enceladus? And what is the effect of each of these processes?

1. **Condensation: nucleation and grain growth.** This model takes into consideration the condensation process of vapour into solid ice particles: grain nucleation and growth. This is modelled through sink terms in the mass, momentum and energy conservation equations, along with two extra conservation equations for the solid fraction and number of particles. This model is useful in making predictions about the plume properties for given channel geometry and reservoir conditions and comparing them to Schmidt et al. 2008 and the laboratory data.
2. **Wall friction and heat convection.** Taking into account wall friction and heat convection might become important to fully describe the condensation phenomena, due to the interaction between the boundary layer and the nucleation phenomenon. Specifically, the presence of a boundary layer has the consequence of effectively decreasing the expansion ratio and thus the nucleation rate and number of particles formed. It has however little effect on the droplet size, as the particle growth phenomenon is basically an inviscid process.
3. **Quasi-1D (Hijden 2021) vs. 2D model.** The quasi-1D approximation is accurate for cases with moderate exit to throat area ratio such as the ones that produce the droplet size and solid fraction ranges of interest. However, 2D effects could become important when wall interactions (grain accretion and sublimation) are considered, as they imply property gradients normal to the flow direction. Wall interactions play a non negligible role in the plumes physics, namely in changing the crack geometry over time. However, such effects were not considered in this work, as the author's main goal was to understand how length scales as disparate as those found in Enceladus or in the Aerodynamics laboratory at TU Delft (where wall interactions are absent) influence the plumes phenomena.

Q2: How can observations from the plumes of Enceladus relate to characteristics of the crevasse and reservoir?

1. **How do the geometric parameters of the channel (length, expansion ratio, smooth/sharp throat, throat location) influence the plume characteristics (velocity, number of particles,**

solid fraction, average droplet size)? The plume characteristics fundamentally depend on the channel geometry. An analysis on the relation between the main plume features and each of the channel geometric parameters is elaborated here.

Length: the channel length influences the location of the onset of nucleation and the droplet size at the vent, while having little effect on the remaining flow properties. Namely, a larger length implies a smaller maximum supersaturation value and thus a rather gradual nucleation process. It also leads to higher average droplet sizes at the vent.

Expansion ratio: the channel geometric expansion is arguably the most influential of all the channel geometric parameters, as it affects all the plume characteristics. A larger expansion ratio implies a larger exit Mach number and velocity, lower pressure ratio, higher number of particles, higher solid fraction and lower average droplet sizes at the vent.

Smooth/sharp throat: the only visible effect of having a sharp channel throat rather than a smooth one is in the number of particles formed: introducing a sharp throat leads to a decrease in the nucleation rate and thus in the total number of solid grains formed at the vent.

Throat location: the throat location plays an important rule in that changing its relative location (i.e. the length fraction at which it is located) varies the residence time of the flow in the divergent section of the channel, where the condensation process largely takes place. Effectively, the closer to the reservoir the throat is located, the lower the number of particles formed, the higher the solid fraction and the higher the average droplet size at the vent.

2. **How do the reservoir conditions (temperature, pressure) affect the plume characteristics?** An increase in the reservoir temperature has the effect of increasing the exit Mach number and velocity, decreasing the pressure ratio, increasing the number of particles formed, decreasing the solid fraction and the average droplet size at the vent. An increase in the reservoir pressure has the opposite effect.
3. **Which channel shape and reservoir conditions are the best fit for the plume characteristics observed by Cassini? Can the results be scaled up from the laboratory to Enceladus?** Very little is actually known about the plume phenomena and reservoir characteristics under the surface of Enceladus. However, from measurements taken by Cassini spacecraft for velocity, solid fraction and grain size at the vent, it is possible to make predictions about the typical crevasse shape and reservoir conditions. Namely, an exit velocity of about 500 m/s, solid fraction around 0.04-0.05 and average droplet size in the tenths of μm roughly corresponds to a crevasse with a length of 150 m, expansion ratio of 1.4 and reservoir temperature around 273 K. This is also in agreement with the expectations of ice-liquid equilibrium in the reservoir. As it is believed that boiling occurs inside the reservoir, a reservoir pressure of around 611 Pa is plausible, so that the reservoir is at close to the triple point equilibrium. In order to achieve higher exit velocities (up to 950 m/s), solid fractions in the range 0.07-0.2 and grain sizes attaining values as high as 75 μm, much larger channel lengths (higher than 1 km) and expansion ratios (close to 4 according to Hijden 2021) are required. As for the similarity between the plumes simulated in the laboratory and the actual ones in Enceladus, due to the fact that the typical length scales in the laboratory are in the 0.1-1 m range, whereas for Enceladus those are in the 100-1000 m range, much smaller droplet sizes will be obtained in the laboratory experiments: average grain size in the nm scale vs. in the 0.1-1 μm scale, respectively. Also, the nucleation process for the plumes in Enceladus will happen much closer to equilibrium than what is measured for the experimental plumes. One way to increase the average droplet size and solid fraction obtained at the vent in the experiments is to design a channel with a throat located close to the reservoir, while keeping a low geometric expansion ratio. Increasing the reservoir pressure also helps achieving higher average vent droplet sizes.

Recommendations

It is worth to keep in mind that this project used a rather simple flow model, considering that the vapour phase behaves as a perfect gas and as a continuous medium. Both of this assumptions are arguable for the extremely low density values the gas attains in these plumes. Future works could consider different thermodynamic and/or kinetic gas models. Another dubious assumption made throughout this work was considering the droplets would be on average so far apart from the channel walls that they would not interact with them. This is empirically known to be false, as the average exit velocity of the grains is on average 2/3 that of the gas. This is only possible considering the grains can collide and stick to the walls, be accelerated back by the flow or sublimate and return back to the gas phase. Finally, the parameter used in this project to describe the effective expansion ratio (ϵ) was defined in terms of the length of the divergent portion of the channel, as it is where the condensation phenomena (nucleation and particle growth) happens at large. However, a more accurate length to be used would be that between the channel location where the first grains are formed and the vent.

Bibliography

Albada, G. D. van, B. van Leer, and W. W. Roberts (1997). “A comparative study of computational methods in cosmic gas dynamics”. In: *Upwind and High-Resolution Schemes*, pp. 95–103.

Anderson Jr., John D. (2017). *Fundamentals of Aerodynamics*. 6th. McGraw-Hill Education.

Atkins, Peter and Julio de Paula (2006). *Physical Chemistry*. 8th. W. H. Freeman and Company.

Azzini, Lucia (2019). “Numerical investigation of dense condensing flows for next-generation power units”. In: Delft University of Technology.

Bakhtar, F. et al. (2005). “Classical Nucleation Theory and Its Application to Condensing Steam Flow Calculations”. In: *Proceedings of the Institution of Mechanical Engineers, Part C: Journal of Mechanical Engineering Science* 219.12, pp. 1315–1333. DOI: `10.1243/095440605x8379`.

Barschdorff, D. et al. (1972). “Homogeneous nucleation in steam nozzle condensation”. In: *Nature Physical Science* 240.103, pp. 166–167. DOI: `10.1038/physci240166a0`.

Becx, T.J. (2019). “Icy moon plume simulator chamber”. In: Delft University of Technology.

Bird, G. A. (1994). *Molecular Gas Dynamics and the Direct Simulation of Gas Flows*. Oxford University Press.

Blondel, F. (2014). “Couplages instationnaires de la vapeur humide dans les écoulements de turbines à vapeur (in French)”. In: École Centrale de Lyon.

Crank, J. and P. Nicolson (1996). “A practical method for numerical evaluation of solutions of partial differential equations of the heat-conduction type”. In: *Advances in Computational Mathematics* 6.1, pp. 207–226. DOI: `10.1007/bf02127704`.

Dong, Y et al. (2011). “The water vapor plumes of Enceladus”. In: *Journal of Geophysical Research Atmospheres* 116. DOI: `10.1029/2011JA016693`.

Gao, P. et al. (2016). “Aggregate particles in the plumes of Enceladus”. In: *Icarus* 264, pp. 227–238. DOI: `10.1016/j.icarus.2015.09.030`.

Greitzer, E. M., C. S. Tan, and M.B. Graf (2004). *Internal Flow: Concepts and Applications*. 1st. Cambridge University Press.

Hedman, M. M. et al. (2009). “Spectral observations of the Enceladus plume with Cassini-VIMS”. In: *The Astrophysical Journal* 693, pp. 1749–1762. DOI: `10.1088/0004-637X/693/2/1749`.

Hijden, N.J. van der (2021). “Linking Enceladus’ plume characteristics to the crevasse properties”. In: Delft University of Technology.

Huang, Yongli et al. (2013). “Size, separation, structural order, and mass density of molecules packing in water and ice”. In: *Scientific Reports* 3. DOI: `10.1038/srep03005`.

Ingersoll, Andrew P. and Miki Nakajima (2016a). “Controlled boiling on Enceladus. 1. Model of the vapor-driven jets”. In: *Icarus* 272, pp. 309–318. DOI: `10.1016/j.icarus.2016.02.027`.

— (2016b). “Controlled boiling on Enceladus. 2.Model of the liquid-filled cracks”. In: *Icarus* 272, pp. 319–326. DOI: `10.1016/j.icarus.2015.12.040`.

Ingersoll, Andrew P. and Alexey A. Pankine (2010). “Subsurface heat transfer on Enceladus: Conditions under which melting occurs”. In: *Icarus* 206, pp. 594–607. DOI: `10.1016/j.icarus.2009.09.015`.

Karagiannis, Angelos (2020). “Numerical Examination of Non-Equilibrium Condensation in Supersonic Micronozzles”. In: Delft University of Technology.

Kempf, Sascha, Uwe Beckmann, and Jürgen Schmidt (2010). “How the Enceladus dust plume feeds Saturn’s E ring”. In: *Elsevier* 206, pp. 446–457. DOI: `10.1016/j.icarus.2009.09.016`.

Kieffer, S. W. et al. (2009). “A redetermination of the ice/vapor ratio of Enceladus’ plumes: Implications for sublimation and the lack of a liquid water reservoir”. In: *Icarus* 203, pp. 238–241. DOI: `10.1016/j.icarus.2009.05.011`.

Kikoin, A. K. and I. K. Kikoin (1978). *Molecular Physics*. Mir Publishers.

Kite, Edwin S. and Allan M. Rubin (2016). “Sustained eruptions on Enceladus explained by turbulent dissipation in tiger stripes”. In: University of California at San Diego.

Kurganov, A. and G. Petrova (2007). “A second-order well-balanced positivity preserving central-upwind scheme for the Saint-Venant system”. In: *Communications in Mathematical Sciences* 5.1, pp. 133–160. DOI: `10.4310/cms.2007.v5.n1.a6`.

Lai, Der-Shaiun and J. R. Kadambi (1993). “Generation of mono-disperse droplets by spontaneous condensation of flow in nozzles”. In: Department of Mechanical and Aerospace Engineering, Case Western Reserve University, Cleveland, Ohio.

Lamanna, G. (2000). “On nucleation and droplet growth in condensing nozzle flows”. In: Technische Universiteit Eindhoven.

Marcantoni, Luis F. Gutiérrez, José P. Tamagno, and Sergio A. Elaskar (2012). “High speed flow simulation using OpenFOAM”. In: *Mecánica Computacional* 31, pp. 2939–2959.

Matson, D. L., J. C. Castillo-Rogez, et al. (2012). “Enceladus: A hypothesis for bringing both heat and chemicals to the surface”. In: *Icarus* 221, pp. 53–62. DOI: `10.1016/j.icarus.2012.05.031`.

— (2018). “Enceladus’ near-surface CO_2 gas pockets and surface frost deposits”. In: *Icarus* 302, pp. 18–26. DOI: `10.1016/j.icarus.2017.10.025`.

Matson, D. L., L. J. Spilker, and J. P. Lebreton (2002). “The Cassini/Huygens Mission to the Saturnian System”. In: *Springer*. DOI: `https://doi.org/10.1007/978-94-017-3251-2_1`.

Matsuo, Kazuyasu et al. (1986). “Studies of condensation shock waves : 2nd report, relation between condensation shock wave and condensation zone”. In: *Bulletin of JSME* 29, pp. 439–443.

Moore, M. J. et al. (1973). “Predicting the fog-drop size in wet steam turbines”. In: Proceedings of the Conference on Wet Steam 4, Coventry, UK. Institution of Mechanical Engineers. Paper C37/73.

Nimmo, F. et al. (2007). “Shear heating as the origin of the plumes and heat flux on Enceladus”. In: *nature* 447, pp. 289–291. DOI: `10.1038/nature05783`.

Peeters, P., J. Gielis, and M. Van Dongen (2002). “The nucleation behavior of supercooled water vapor in helium”. In: *The Journal of chemical physics* 117, pp. 5647–5653. DOI: `10.1063/1.1501885`.

Porco, C. C. et al. (2006). “Cassini Observes the Active South Pole of Enceladus”. In: *Science* 311, pp. 1393–1401. DOI: `10.1126/science.1123013`.

Porco, Carolyn, Daiana DiNino, and Francis Nimmo (2014). “How the geysers, tidal stresses, and thermal emission across the south polar terrain of Enceladus are related”. In: *The Astronomical Journal* 148.3. DOI: `10.1088/0004-6256/148/3/45`.

Postberg, F. et al. (2009). “Sodium salts in E-ring ice grains from an ocean below the surface of Enceladus”. In: *nature* 459, pp. 1098–1101. DOI: `10.1038/nature08046`.

— (2011). “A salt-water reservoir as the source of a compositionally stratified plume on Enceladus”. In: *nature* 474, pp. 620–622. DOI: `10.1038/nature10175`.

Pouring, Andrew (1965). “Thermal choking and condensation in nozzles”. In: *The Physics of Fluids* 8.10, pp. 1802–1810. DOI: `10.1063/1.1761112`.

Roberts, J. H. and F. Nimmo (2008). “Near-surface heating on Enceladus and the south polar thermal anomaly”. In: *Journal of the Aeronautical Sciences* 35. DOI: `10.1029/2008GL033725`.

Schmidt, Jürgen et al. (2008). “Slow dust in Enceladus’ plume from condensation and wall collisions in tiger stripe fractures”. In: *nature* 451, pp. 685–688. DOI: `10.1038/nature06491`.

Sklavenitis, Stavros (2022). “Experimental simulation and assessment of the geysers of icy moons in the laboratory”. In: Delft University of Technology.

Tsien, Hsue-Shen (1946). “Superaerodynamics, Mechanics of Rarefied Gases”. In: *Journal of the Aeronautical Sciences* 13.12, pp. 653–664. DOI: `10.2514/8.11476`.

Verhoeff, T. H. P. (2023). “Laboratory experiments recreating icy moons’ geysers”. In: Delft University of Technology.

Waite Jr, J. H. et al. (2009). “Liquid water on Enceladus from observations of ammonia and ^{40}Ar in the plume”. In: *nature* 460, pp. 487–490. DOI: `10.1038/nature08153`.

Warming, R. F. and R. M. Beam (1976). “Upwind second-order difference schemes and applications in aerodynamic flows”. In: *AIAA Journal* 14.9, pp. 1241–1249. DOI: `10.2514/3.61457`.

Wegener, Peter P. (1964). “Condensation phenomena in nozzles”. In: *Elsevier* 15, pp. 701–724. DOI: `10.1016/B978-1-4832-2730-6.50033-6`.

Wen, Chuang et al. (2019). “Non-equilibrium condensation of water vapour in supersonic flows with shock waves”. In: *International journal of heat and mass transfer* 149.119109. DOI: `10.1016/j.ijheatmasstransfer.2019.119109b`.

Wölk, Judith and Reinhard Strey (2001). “Homogeneous Nucleation of H2O and D2O in Comparison: The Isotope Effect”. In: Institut für Physikalische Chemie, Universität zu Köln.

Yeoh, S. K., T. A. Chapman, et al. (2015). “On understanding the physics of the Enceladus south polar plume via numerical simulation”. In: *Icarus* 253, pp. 205–222. DOI: `10.1016/j.icarus.2015.02.020`.

Yeoh, S. K., Z. Li, et al. (2016). “Constraining the Enceladus plume using numerical simulation and Cassini data”. In: *Icarus* 281, pp. 357–378. DOI: `10.1016/j.icarus.2016.08.028`.

Young, J. B. (1980). “Spontaneous Condensation of Steam in Supersonic Nozzles”. In: Cambridge Univ. (England).; National Aeronautics and Space Administration, Washington, DC.

Zhang, Guojie et al. (2019). “The relationship between the nucleation process and boundary conditions on non-equilibrium condensing flow based on the modified model”. In: *International Journal of Multiphase Flow* 114, pp. 180–191. DOI: `10.1016/j.ijmultiphaseflow.2019.03.005`.

A

Source Code Example

A pseudo-code version of the algorithm used for the condensation model is presented here. In case the reader is interested, the actual OpenFOAM source code can be accessed through the link *https://github.com/baetatomska98/Enceladus/tree/main/rhoCentralFoam_2ph.*

```
for each domain cell
    Compute local saturation properties;
    if rho * N * V_cell < 1.0 or f < 1e-12
        f, N = 0;
    end
    if T < T_crit and T < T_sat(p) and T >= 173.16
        Compute local solid grain properties;
        if rho * N * V_cell >= 1.0 and f >= 1e-12
            Compute r_droplet from f and N;
        else
            r_droplet = 0;
        end
        if S >= 1
            Compute r_crit;
        else
            r_crit = 0;
        end
        if r >= r_crit and r >= 2.75e-10
            Compute droplet growth rate;
            Compute active component of mass generation source term;
        else
            Set both terms to zero;
        end
        if r_crit >= 2.75e-10
            Compute nucleation rate;
            if gamma_nuc * V_cell * delta t < 1.0
                gamma_nuc = 0;
            end
        else
            r_crit, gamma_nuc = 0;
        end
        Compute the remaining source terms;
    else
        Set all condensation terms to zero;
    end
end
```

B

Extra figures

In this section of the appendix, the contour plots obtained by simulating the plumes with the OpenFOAM solver are shown.

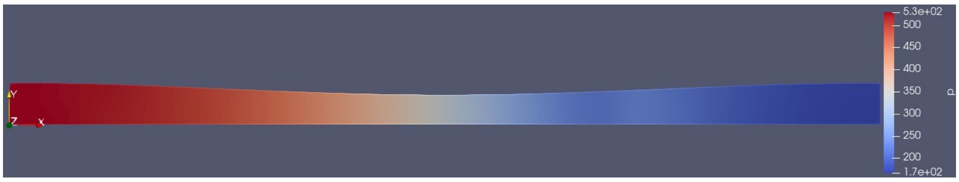

Figure B.1: Contour of the static pressure field for the baseline case.

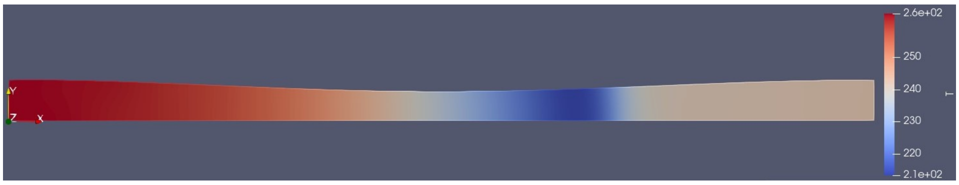

Figure B.2: Contour of the static temperature field for the baseline case.

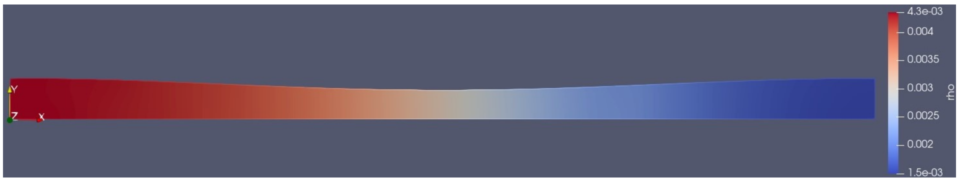

Figure B.3: Contour of the density field for the baseline case.

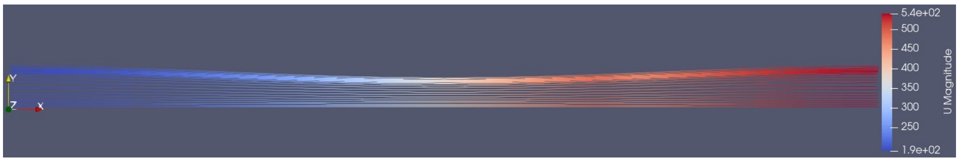

Figure B.4: Shape of the streamlines for the baseline case.

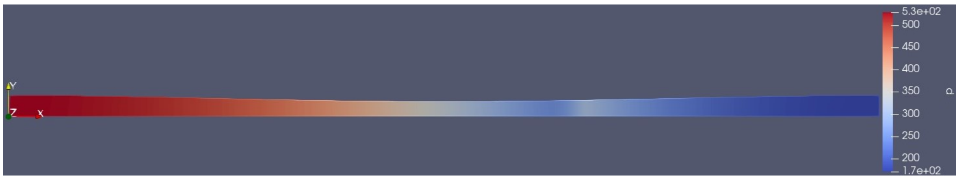

Figure B.5: Contour of the static pressure field for the longer channel case.

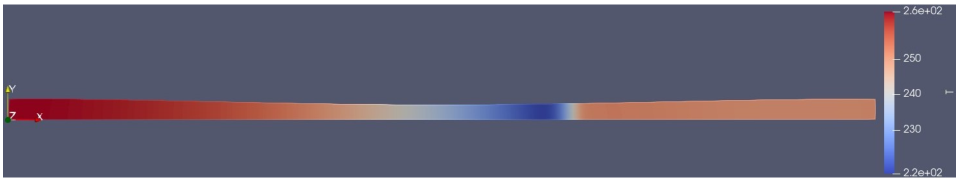

Figure B.6: Contour of the static temperature field for the longer channel case.

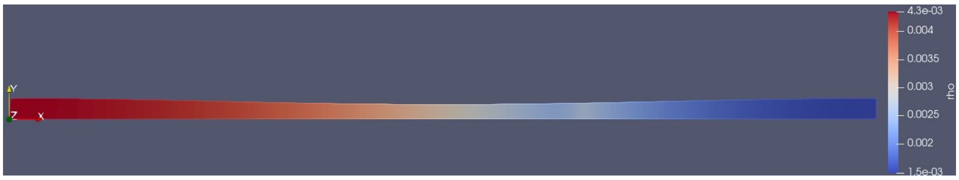

Figure B.7: Contour of the density field for the longer channel case.

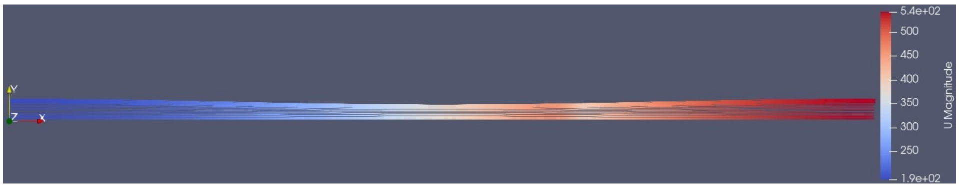

Figure B.8: Shape of the streamlines for the longer channel case.

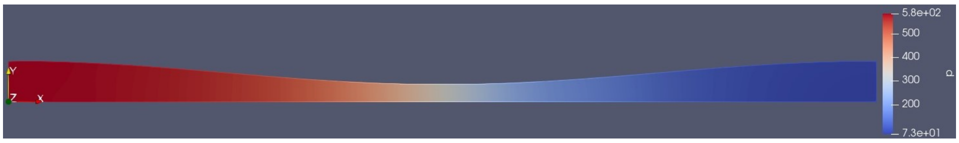

Figure B.9: Contour of the static pressure field for the channel case with a higher expansion ratio.

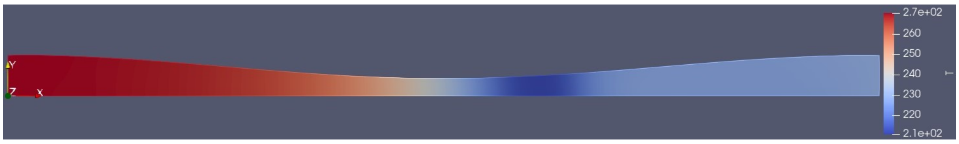

Figure B.10: Contour of the static temperature field for the channel case with a higher expansion ratio.

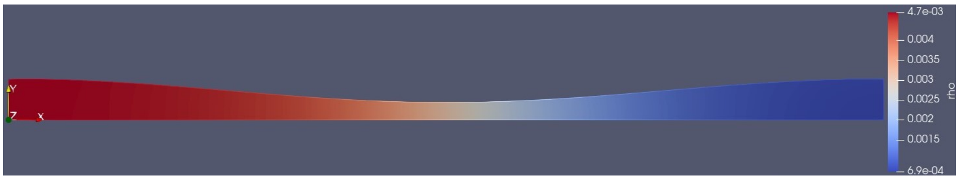

Figure B.11: Contour of the density field for the channel case with a higher expansion ratio.

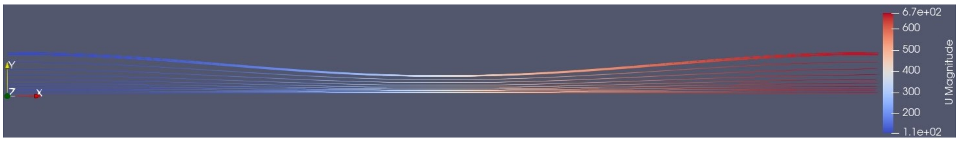

Figure B.12: Shape of the streamlines for the channel case with a higher expansion ratio.

Figure B.13: Contour of the static pressure field for the channel case with a throat located at $x_{throat}/L = 0.25$.

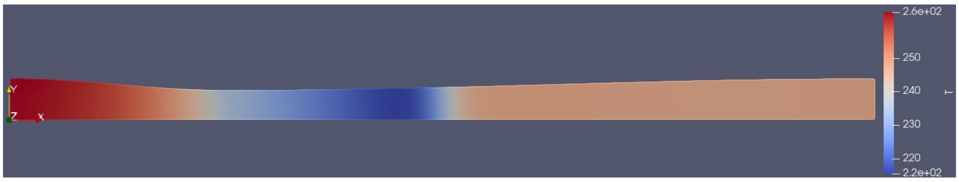

Figure B.14: Contour of the static temperature field for the channel case with a throat located at $x_{throat}/L = 0.25$.

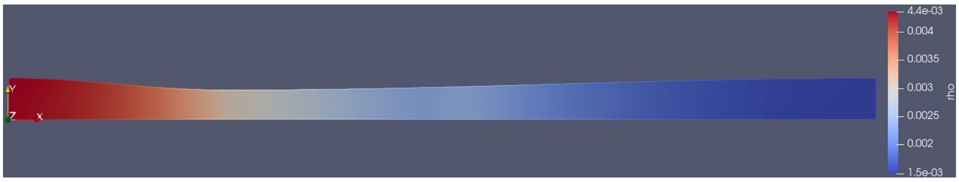

Figure B.15: Contour of the density field for the channel case with a throat located at $x_{throat}/L = 0.25$.

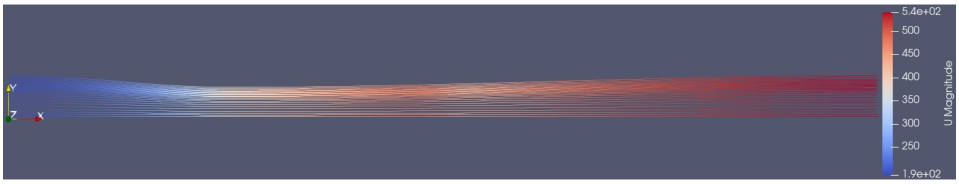

Figure B.16: Shape of the streamlines for the channel case with a throat located at $x_{throat}/L = 0.25$.

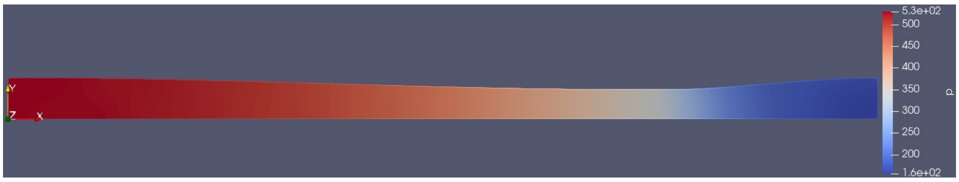

Figure B.17: Contour of the static pressure field for the channel case with a throat located at $x_{throat}/L = 0.75$.

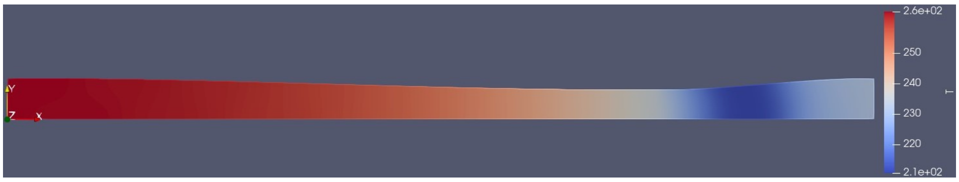

Figure B.18: Contour of the static temperature field for the channel case with a throat located at $x_{throat}/L = 0.75$.

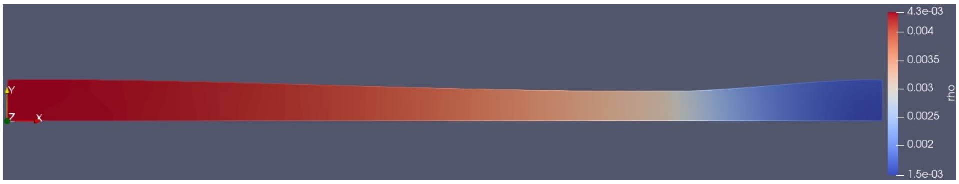

Figure B.19: Contour of the density field for the channel case with a throat located at $x_{throat}/L = 0.75$.

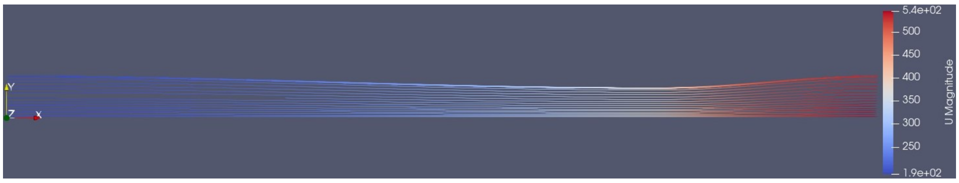

Figure B.20: Shape of the streamlines for the channel case with a throat located at $x_{throat}/L = 0.75$.

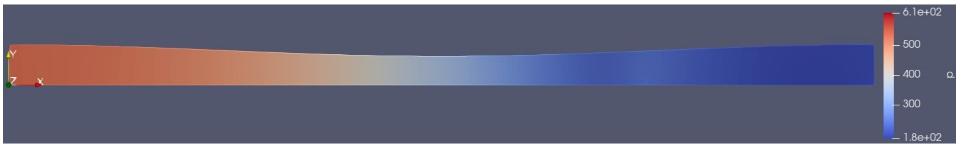

Figure B.21: Contour of the static pressure field for the case with wall friction and heat convection.

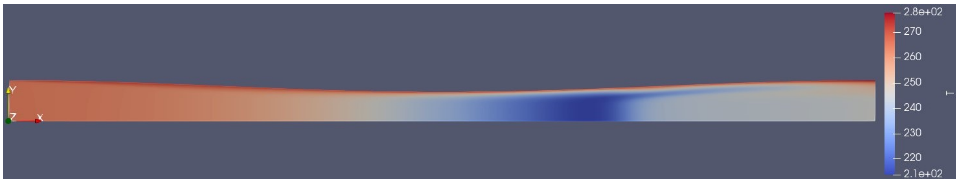

Figure B.22: Contour of the static temperature field for the case with wall friction and heat convection.

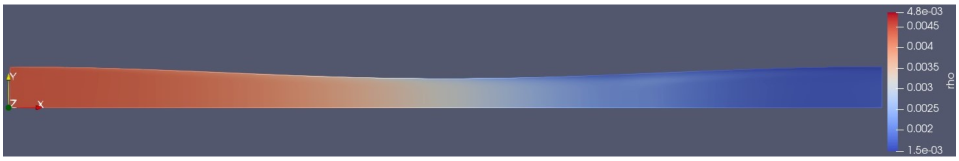

Figure B.23: Contour of the density field for the case with wall friction and heat convection.

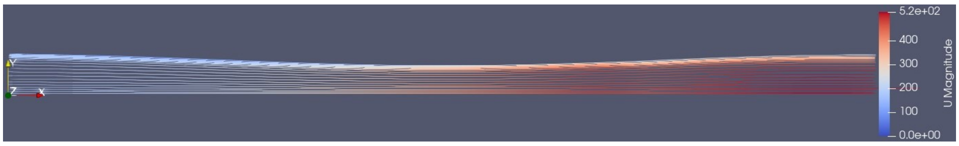

Figure B.24: Shape of the streamlines for the case with wall friction and heat convection.

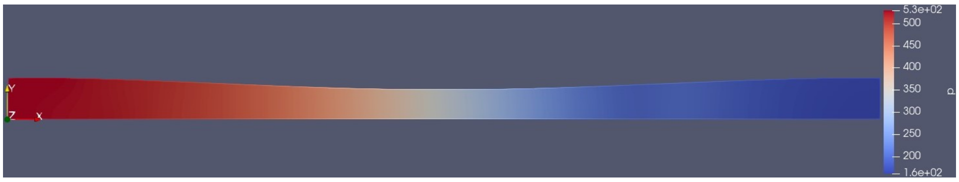

Figure B.25: Contour of the static pressure field for the case with a reservoir temperature of $T_{res} = 278.16K$.

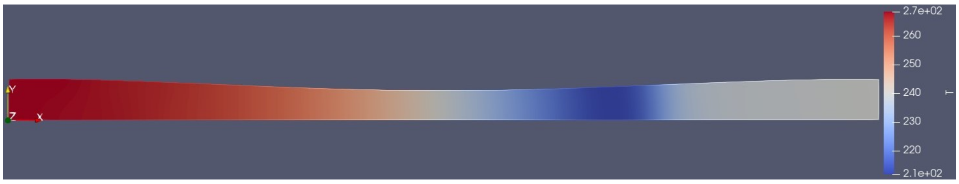

Figure B.26: Contour of the static temperature field for the case with a reservoir temperature of $T_{res} = 278.16K$.

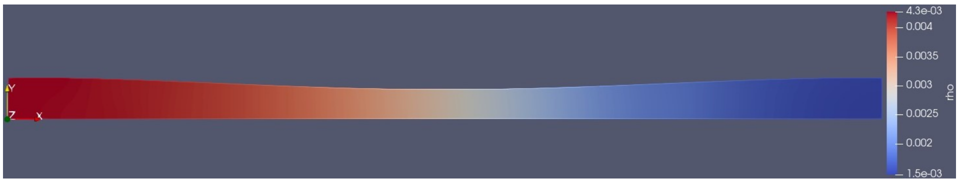

Figure B.27: Contour of the density field for the case with a reservoir temperature of $T_{res} = 278.16K$.

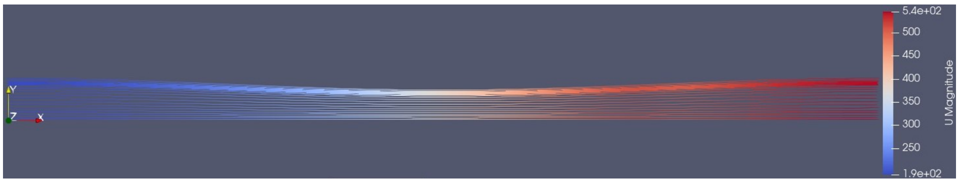

Figure B.28: Shape of the streamlines for the case with a reservoir temperature of $T_{res} = 278.16K$.

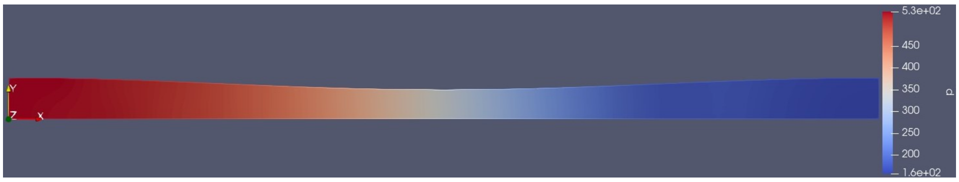

Figure B.29: Contour of the static pressure field for the case with a reservoir temperature of $T_{res} = 283.16K$.

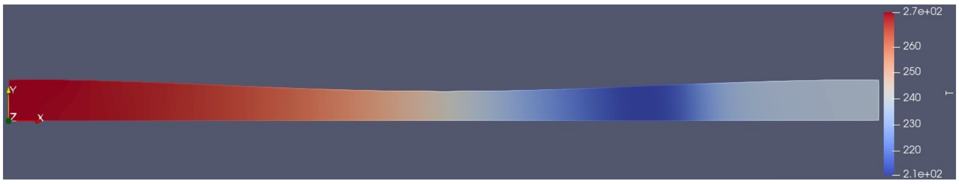

Figure B.30: Contour of the static temperature field for the case with a reservoir temperature of $T_{res} = 283.16K$.

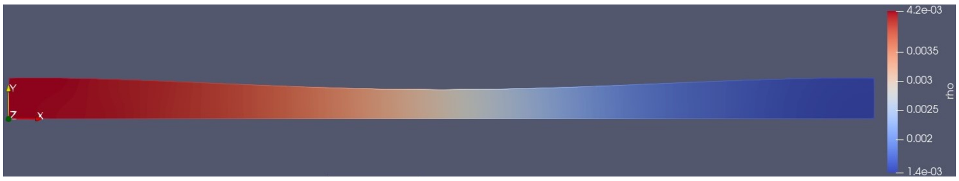

Figure B.31: Contour of the density field for the case with a reservoir temperature of $T_{res} = 283.16K$.

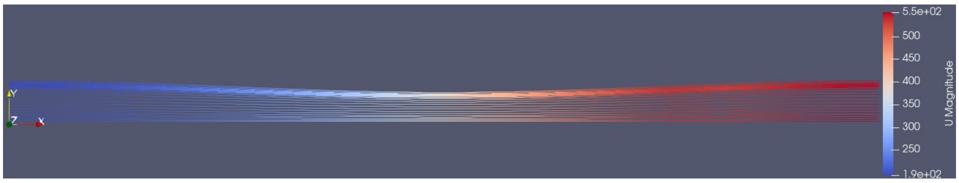

Figure B.32: Shape of the streamlines for the case with a reservoir temperature of $T_{res} = 283.16K$.

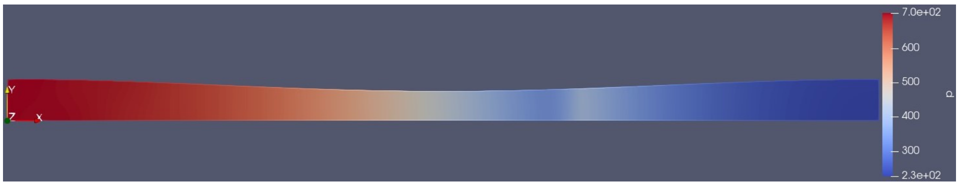

Figure B.33: Contour of the static pressure field for the case with a reservoir pressure of $p_{res} = 811.2Pa$.

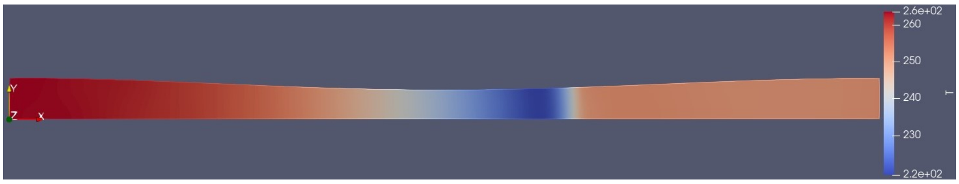

Figure B.34: Contour of the static temperature field for the case with a reservoir pressure of $p_{res} = 811.2Pa$.

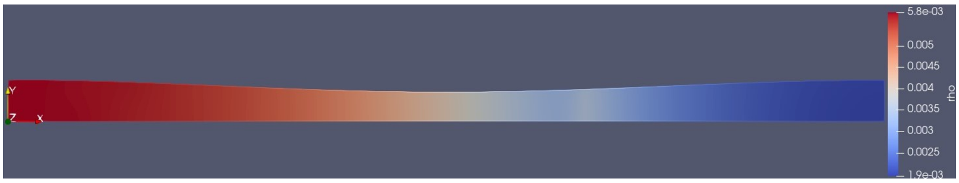

Figure B.35: Contour of the density field for the case with a reservoir pressure of $p_{res} = 811.2Pa$.

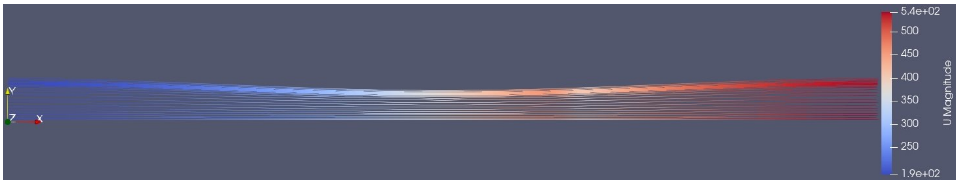

Figure B.36: Shape of the streamlines for the case with a reservoir pressure of $p_{res} = 811.2Pa$.

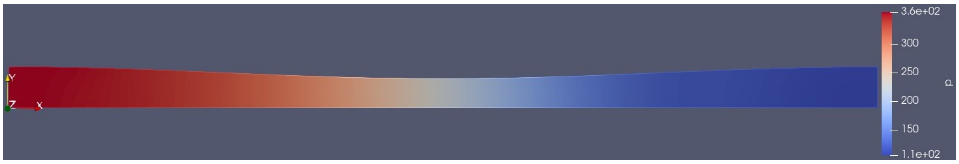

Figure B.37: Contour of the static pressure field for the case with a reservoir pressure of $p_{res} = 411.2Pa$.

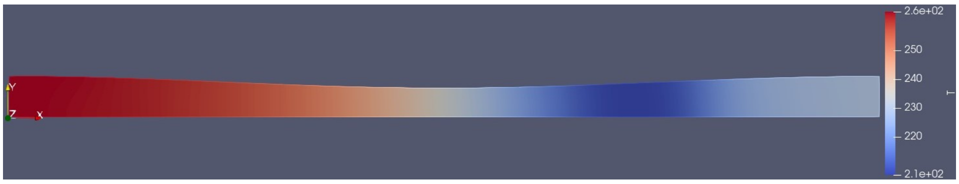

Figure B.38: Contour of the static temperature field for the case with a reservoir pressure of $p_{res} = 411.2Pa$.

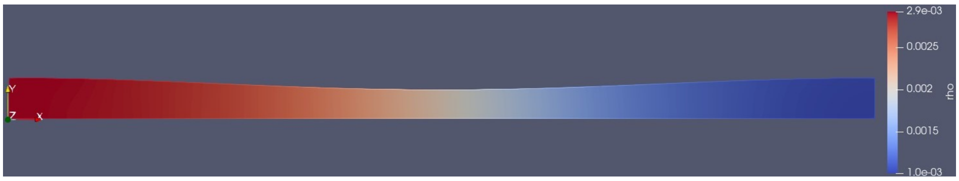

Figure B.39: Contour of the density field for the case with a reservoir pressure of $p_{res} = 411.2Pa$.

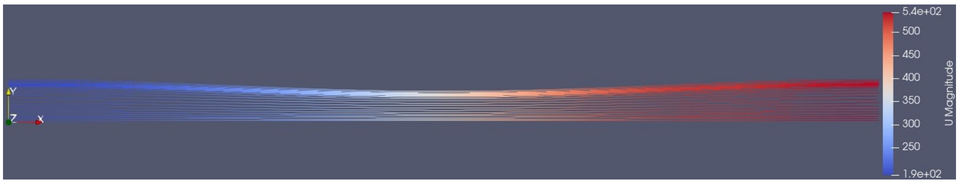

Figure B.40: Shape of the streamlines for the case with a reservoir pressure of $p_{res} = 411.2Pa$.